A measurement of the electron neutrino component in the T2K beam using the tracker detectors and the electromagnetic calorimeter at the near detector ND280

Thesis submitted in accordance with the requirements of the University of Liverpool for the degree of Doctor in Philosophy

by

Georgios Christodoulou

Oliver Lodge Laboratory,

University of Liverpool,

September 2011

Abstract

Starting with a muon neutrino (ν_μ) beam T2K is searching for electron neutrino (ν_e) appearance in the Far Detector (Super-Kamiokande) and aims to produce the first measurement of the neutrino mixing angle θ_{13}. Beam contamination of ν_e is one of the main background components. The Near Detector, ND280, is optimized for measuring the ν_e contamination through the reconstruction of ν_e interactions. The ν_e beam contamination is studied in this thesis. The total number of ν_e beam events reconstructed in ND280 is $51.2^{+21.3\ \text{stat.}\ +10.1\ \text{sys.}}_{-21.3\ \text{stat.}\ -14.4\ \text{sys.}}$ for 1.068×10^{20} protons on target, a result which is consistent with the Monte Carlo expectations. This result a supplementary statement to the $\nu_\mu \rightarrow \nu_e$ oscillation signal observed at Super-Kamiokande during the first year of T2K run, as no significant excess in the expected ν_e beam contamination has been observed.

Acknowledgments

Since the beginning of my PhD in 2007 until the very end in 2011 it was a very exciting experience. With the ups and downs, the hard and the good times, the days literally living in the physics department, the T2K collaboration and UK meetings with the talks and karaoke, the international and local conferences, the 11th of March earthquake, the essential coffee breaks, the long physics discussions, the wonderful personal development record, the university skills workshops and the bubble chamber football tournament are only a small fraction of what happened during this exciting period.

Firstly, I would like to say a huge thank you to my supervisor Prof. Christos Touramanis, who despite his extremely busy routine he has always time to answer my physics and analysis questions, providing guidelines and giving advice. But, beyond physics he is also a good advisor in many other areas and maybe one of the most important things I have learned from him, is that physics is not only sitting in front of a computer writing complicated algorithms or solving mathematical equations, but is also politics, economics and social networking.

This thesis could not survive without the support of my colleagues from the university of Liverpool. Especially I would like to thank my secondary supervisor Dr. Neil McCauley for all the advice and his efforts to make me understand much deeper the physics meaning in my work. I would also like to thank Dr. David Payne, Dr. Carlos Chavez and Dr. Jon Coleman for all the help they very happily provided to me and the long discussions until the last minute before I complete this work. The presence of my fellow T2K graduate students, Richard Calland, Alex Thorley, Matt Murdoch and Lorna Kellett, who sometimes made the time flow much quicker and for all the good memories and the unforgettable moments. Also, a special thank to all the other Liverpool students for baking Mondays and

pub Fridays, and especially my fellow travelers James Mylroie-Smith, Bozydar Wrona and Sylwia Migas. I would also like to thank all the academic and administrative staff in the university of Liverpool for all their help.

The experience working in a big collaboration is really unique and I would like to thank all my T2K collaborators.

My time at Liverpool could not be better without the moments shared with the Greek-Cypriot community. I would like to thank you all and really looking forward for a reunion.

This thesis could not never finish without the trust and support of my family, my parents Marios and Eleni, and, my brothers Charalambos and Nicholas, who although they never realized what exactly I am doing they always tried very hard to understand. I now promise to explain every single word written in this thesis.

Contents

List of Figures

List of Tables

Chapter 1

Introduction

Neutrino physics is one of the newest and most rapidly evolving fields in high energy physics. Being the first particle introduced before its actual discovery, the story of the neutrino could either be very short or long and promising. It finally turned out to be the latter for almost 100 years now. The fascinating life of the neutrino starts along with the first primary experiments which determined its existence and will be discussed at the beginning of the introductory chapter. This follows a basic review of the main types of neutrino experiments; solar, atmospheric, reactor and accelerator, and also with some basic comments on the neutrino masses and generations.

1.1 The mysterious neutrino

The "life" of the neutrino starts in the early 1930s when the continuous spectra of the beta decay is established [1]. In contrast to the discrete spectrum of α and γ rays, the observation of a continuous spectra in beta decay could suggest a violation of the energy conversation principle. Soon Wolfgang Pauli came up with the hypothesis of the existence of a neutral particle in order to resolve the energy conservation crisis for beta decay. He called this hypothetical particle "neutron", but it was renamed to neutrino after the discovery of the neutron in 1932 by James Chadwick [2]. In 1933, Enrico Fermi established the first successful effective theory for beta decay, incorporating the neutrino [3]. A few years later Shoichi Sakata and Takesi Inoue proposed the muon-pion scheme with the muon accompanied by a neutrino [4].

Although the neutrino was postulated to exist in the early 1930s, it was not until the

1950s that the effort for detecting neutrinos began. Frederick Reines and Clyde Cowan headed "Project Poltergeist" aiming to detect (anti)neutrinos from nuclear reactors. The method used to tag (anti)neutrinos was groundbreaking and the same method is still used by reactor neutrino experiments today. They considered the inverse beta decay $\bar{\nu}_e + p \rightarrow e^+ + n$. The positron quickly annihilates with a nearby electron, while the neutron will scatter randomly in the detector until is captured, emitting photons with a well defined energy. By measuring the characteristic time between the positron annihilation and the photon emission from the neutron capture they were able to study the antineutrinos produced at nuclear reactors. Definite evidence was obtained in 1956 [5] and the first results published in 1960 [6]. Reines was awarded the Nobel prize in 1995 for "pioneering experimental contributions to lepton physics".

In 1957, Bruno Pontecorvo introduced neutrino-antineutrino oscillations [7, 8]. Later on, this led to the theory of neutrino oscillations (see next chapter), but at that time the model introduced was analogous to the $K^0 - \bar{K}^0$ oscillations. In 1962, Ziro Maki, Masami Nakagawa and Sakata introduce the neutrino flavor mixing theory [9].

Soon after the discovery of the muon, the question was raised if the accompanying muon-neutrino was the same as the electron neutrino. The answer came in 1962 when Leon Lederman, Mel Schwartz and Jack Steinberger created the first artificial neutrino beam at the Brookhaven National Laboratory and verified that the muon neutrino was indeed different from the electron neutrino [10]. They developed a unique technique, still used today in long baseline neutrino experiments. In simple words, they smashed protons on a fixed target, creating a large flux of pions. The pions then decay into muons and neutrinos. One can steer the surviving pions, and hence the muons and the neutrinos, into a beam-dump and put a detector at the other end. The question was now if the muon neutrino would produce a muon or an electron when it interacts with matter. The experiment revealed that only muons can be produced and confirmed the existence of the second family of neutrinos. Lederman, Schwartz and Steinberger were awarded the Nobel prize in 1988 "for the neutrino beam method and the demonstration of the doublet structure of the leptons through the discovery of the muon neutrino".

The discovery of the tau lepton in 1975 [11] by Martin Perl and colleagues at SLAC,

Stanford California suggested the existence of the accompanied neutrino, ν_τ. The first indirect evidence for the existence of a weak neutral current carrier was observed when the neutral current neutrino interactions were discovered in 1973 at the Gargamelle bubble chamber experiment at CERN [12, 13]. Hard evidence for the existence of a third neutrino generation was obtained in 1989 from the LEP experiment at CERN. The width of the Z^0 boson is consistent with the Standard Model (SM) predictions as long as there are 3 weakly interacting neutrino species [14]. Nevertheless, the direct observation of the ν_τ was achieved in 2001 by the DONUT collaboration [15].

Neutrino oscillations is one of the most topical areas in neutrino physics, developed since the early 1990s. Neutrino oscillations describe the probability that a neutrino with some energy after travelling a specific distance can change flavor. The most usual interpretation of this result is that the neutrino flavor eigenstates are a superposition of the mass eigenstates, suggesting, against the SM prediction, that the neutrino is actually massive. Neutrino oscillations are usually defined by five mixing parameters, two mass square differences, Δm^2_{21} and Δm^2_{31}, and the three mixing angles, θ_{12}, θ_{23} and θ_{13}. This chapter will focus mostly on the efforts established mainly in the last 20 years to measure the five neutrino oscillation parameters. The next chapter will focus on the theoretical and phenomenological aspects of neutrino oscillations.

1.2 Solar Neutrinos

Soon after it was realized that the Sun gets its energy from nuclear fusion, it was also understood that the Earth is actually bombarded with enormous fluxes of neutrinos since most of the Sun's energy is produced through the proton-proton fusion.

The first evidence for the existence of solar electron neutrinos was obtained in 1964 when the Homestake Solar Neutrino Observatory in South Dakota, led by Ray Davis, detected the first electron neutrinos via the inverse beta decay, $\nu_e + {}^{37}Cl \rightarrow e^- + {}^{37}Ar$ [16]. The experiment, located 1478 m below the surface, consists of a very large tank of 615 tonnes of tetrachloroethylene and the purpose was to search for argon atoms produced by the decay of radioactive ${}^{37}Ar$. Homestake ran until 1984 and Davis was awarded the Physics Nobel prize in 2002 "for pioneering contributions to astrophysics, in particular

for the detection of cosmic neutrinos." After the first results published by the Homestake experiment in 1960s, a rather strange puzzle appeared: the neutrino flux measured was statistically smaller than that predicted from the Standard Solar Model [16, 17]. This was the first sign of the solar neutrino anomaly, confirmed decades later by other experiments.

Homestake was followed by the Kamiokande [18] (Kamioka Nucleon Decay Experiment) experiment, built in a zinc mine in Japan and initially designed to search for proton decay. However, this water Cherenkov experiment also looked for Solar neutrinos via the neutrino-electron elastic scattering, $\nu_e + e^- \rightarrow \nu_e + e^-$. The Kamiokande experiment was only sensitive to the most energetic neutrinos from the Sun coming from ^8B, but, since the recoil electron can produce Cherenkov light it was able to reconstruct the electron energy and direction, thus it was the first experiment to reconstruct the direction of the incoming neutrino with respect to the position of the Sun.

The search for Solar neutrinos was continued in the early 1990s with two more radiochemical experiments, similar to Homestake, the GALLEX [19] experiment in Italy and the SAGE [20] experiment in the USSR. Both searched for neutrinos via the inverse nuclear β decay of gallium, $\nu_e + ^{71}Ga \rightarrow e^- + ^{71}Ge$. Although these experiments could not measure the energy of the incoming neutrinos, they had a lower energy threshold than the Kamiokande experiment.

Kamiokande, GALLEX and SAGE confirmed the solar neutrino anomaly observed by Homestake thirty years earlier. The explanation for the neutrino deficit in these experiments came a decade later from Super-Kamiokande, SNO and finally by the KamLAND experiment.

Super-Kamiokande [21, 22, 23] is the extended and improved version of Kamiokande. It was designed to study both atmospheric (see next section) and solar neutrinos and also to improve the sensitivity to proton decay searches. For solar neutrinos the purpose was to precisely measure the solar neutrino spectrum from ^8B. The contribution of Super-Kamiokande was significant: to confirm the solar neutrino deficit and also to show that the deficit is constant with time and independent of the neutrino energy at the range of 5-10 MeV.

SNO [24, 25] (Sudbury Neutrino Observatory) is a heavy water detector measuring

neutrino interactions via 3 main processes, Charge Current: $\nu_e + ^2 H \rightarrow 2p + e^-$, Elastic Scattering: $\nu + e^- \rightarrow \nu + e^-$ and Neutral Current: $\nu + ^2 H \rightarrow \nu + p + n$. Like Super-Kamiokande SNO also searched for the ^8B neutrinos. The kinematics of the electrons produced from neutrino-electron scattering and neutrino-deuteron scattering are different, allowing to separate these two reactions. Neutron detection for the neutral current neutrino-deuteron interaction is done either using the photons emitted by the neutron capture in deuteron or placing ^3He neutron detectors inside the heavy water tank. From the three above neutrino interactions used by SNO to detect neutrinos, the charge current neutrino-deuteron scattering is only possible for the electron neutrinos. The neutral current neutrino-deuteron is flavor blind, while the neutrino-electron scattering is possible for all neutrino flavors, but with a much higher probability for electron neutrinos. Thus SNO could measure simultaneously the solar ν_e and the total, all flavor, solar neutrino flux. The observation that ν_μ and/or ν_τ are coming from the Sun, provided one of the strongest evidences of the neutrino oscillation hypothesis, leading to a very elegant solution [26] to the solar neutrino deficit observed decades earlier. The survival probability of solar neutrinos in vacuum can take the simple form

$$P_{\nu_e \rightarrow \nu_e}(E, L) = 1 - \sin^2 2\theta \sin^2 \left(\frac{\Delta m^2 L}{4E} \right), \tag{1.1}$$

where L is the Earth-Sun distance, E is the incident neutrino energy, θ is the neutrino mixing angle and Δm^2 is the mass difference of the neutrino mass eigenstates. Although in reality neutrino oscillations in the vacuum can't explain very well the Solar neutrino flux deficit, the introduction of matter effects can provide an elegant solution to the Solar neutrino problem. More about neutrino oscillations can be found in the next chapter.

1.3 Atmospheric Neutrinos

Atmospheric neutrinos are produced when cosmic protons interact in the upper atmosphere producing pions. The pions then decay into muons and muon neutrinos. The muons decay to electrons and 2 neutrinos. Atmospheric neutrino experiments measure the ν_μ/ν_e ratio at the sea level, and thus the R-ratio, which is the ν_μ/ν_e ratio divided by its theoretical

prediction, is close to two.

The first experiments that searched for atmospheric neutrinos in 1980s and early 1990s measured an unexpected low R-ratio. This could imply either a smaller ν_μ flux or a higher ν_e flux than expected. Details for the measured R-ratio from different experiments can be found in [27].

The most important contribution to the atmospheric neutrino sector was made by the Kamiokande (and Super-Kamiokande later) experiment. Kamiokande not only measured the R-ratio but also measured the ν_μ and ν_e fluxes with respect to the neutrino direction [18]. The solution to the atmospheric neutrino anomaly arrived a bit later from Super-Kamiokande, showing that indeed the ν_μ are disappearing [21, 22, 23]. For the atmospheric neutrinos, the disappearance probability can take the simplified form

$$P_{\nu_\mu \to \nu_\tau}(E, L) = \sin^2 2\theta \sin^2 \left(\frac{\Delta m^2 L}{4E} \right). \tag{1.2}$$

The distance L from the production point to the detector is estimated as a function of the zenith angle of the neutrino arrival direction.

1.4 Reactor Neutrinos

Reactor neutrino experiments use the copious $\bar{\nu}_e$ flux produced by nuclear fission reactions. These neutrinos have relatively low energy, the average being 4 MeV. The technique used is very similar to the one described previously from the first neutrino experiment by F. Reines and C. Cowan using the inverse beta decay $\bar{\nu}_e + p \to e^+ + n$.

The disappearance of the reactor $\bar{\nu}_e$ was first measured by the KamLAND experiment [28]. KamLAND was surrounded by 55 Japanese nuclear reactor cores and the results confirmed the oscillation effect observed in solar neutrinos. Past reactor experiments such as CHOOZ [29], a liquid scintillation enriched with Gd, an element with high neutron capture cross section, and Palo Verde [30] measured the flux of $\bar{\nu}_e$ at 1 km from the reactor cores. These two experiments could not confirm the disappearance of the neutrinos but CHOOZ put the best current upper limit on the third so far unknown mixing angle (θ_{13}). The importance of this result is that the neutrino disappearance oscillations studied from

Super-Kamiokande do not involve the ν_e appearance case. Current experiments, like the Double-CHOOZ [31], which is an upgrade of the CHOOZ experiment, and the Daya Bay in China [32] which use 2 or more near and far detectors in order to reduce the systematic uncertainties on the neutrino flux and energy spectrum, will try to detect a signature of the θ_{13} mixing angle. A recent fit to solar neutrino oscillation parameters from solar+reactor data is shown in Figure 1.1 (from [33]).

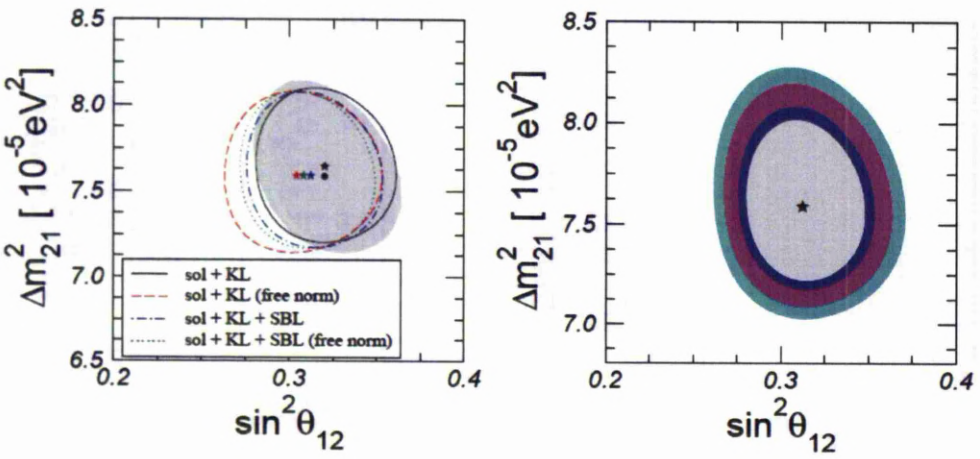

Figure 1.1: Global fit of solar neutrino parameters from solar+KamLAND data. Plot on the left shows the 2 σ allowance using different assumptions for the reactor neutrino fluxes. The plot on the right shows the combined fit for 90 %, 95 %, 99 %, 99.73 % CL. From [33].

1.5 Accelerator Neutrinos

As described earlier neutrino beams can be artificially created in the laboratory by smashing protons on a fixed target and producing pions which will eventually decay to muon neutrinos. Accelerator based neutrino oscillation experiments are sensitive to the atmospheric

neutrino oscillation parameters through the ν_μ disappearance and also to the ν_e appearance by measuring the θ_{13} mixing angle. The detector is usually built at a specific distance in order to reach the maximum or minimum for the neutrino oscillation hypothesis. Usually this distance is of the order of a few hundred kilometers. Another detector is also located near the neutrino beam production point in order to reduce the systematic uncertainties and also to measure various neutrino cross sections.

K2K [34] was the first accelerator neutrino oscillation experiment to observe neutrino oscillations. It used the 12 GeV proton beam at KEK in Japan to produce neutrinos and direct them to the 50 kilo-tonnes Super-Kamiokande detector at a distance of 250 km. The protons hit an aluminium target and the produced pions and kaons were bent forward by 2 magnetic horns into a decay volume. The decayed pions and kaons result in a neutrino beam whose energy peaks near 1.3 GeV. A near detector is located 300 m downstream of the target. The first near detector is a one kiloton water Cerenkov detector and the second is a fine grained detector. K2K measured the ν_μ disappearance in good agreement with the neutrino atmospheric experiments.

MINOS [35] is another accelerator neutrino oscillation experiment. It uses the NuMI beam at Fermilab to send neutrinos at a distance of 735 km away in order to measure ν_μ oscillations. The current measurements on the atmospheric neutrino oscillation parameters from MINOS are $|\Delta m^2_{23}| = (2.32^{+0.12}_{-0.08}) \times 10^{-3} eV^2$ and $\sin^2 2\theta_{23} > 0.9$ at 90% CL [36]. A combined fit of atmospheric and MINOS data is shown on Fig. 1.2 (from [33]).

1.6 Constraints on neutrino masses

Neutrino oscillation experiments can only measure the mass squared difference of the neutrino mass eigenstates. However, weak decays are a direct way of measuring the neutrino masses.

Tritium experiments, ${}^3He \rightarrow {}^3 He + e^- + \nu_e$, have been able to put an upper limit on electron neutrino mass. The Mainz experiment set an upper limit for the electron neutrino mass at 2.3 eV at 95% CL [37] and the Troitzk experiment at $m_{\nu_e} < 2.5$ eV at 95% CL [38]. Both Mainz and Troitzk collaborations have been merged to a new collaboration called KATRIN, with an expected sensitivity down at 0.2 eV [39].

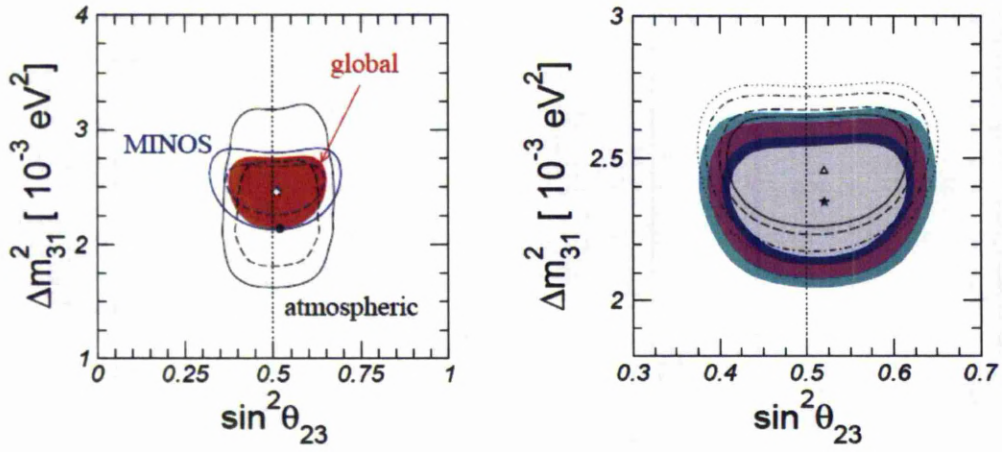

Figure 1.2: On the left: 90 % CL (dashed) and 3 σ (solid) for atmospheric (black), MINOS (blue) and combined (red/shaded). On the right: Combined fit for atmospheric+MINOS data at 90 %, 95 %, 99 %, 99.73 % CL for normal hierarchy (black) and inverted hierarchy (colored). From [33].

The study of the pion or tau decay can also give direct information about the neutrino mass. The mass of the ν_μ can be measured if the pion and muon momenta are accurately measured via the decay $\pi^+ \rightarrow \mu + \nu_\mu$. Such results from PSI suggest for the neutrino masses that $m_k < 0.17\ MeV/c^2$ (90% CL) for k=1,2,3 [40]. ALEPH measured the neutrino masses from the tau decays $\tau^- \rightarrow 2\pi^- + \pi^+ + \nu_\tau$ and $\tau^- \rightarrow 3\pi^- + 2\pi^+ + \pi^0 + \nu_\tau$ with the result $m_k < 18.2\ MeV/c^2$ (90% CL) for k=1,2,3 [41].

Neutrino-less double β decay ($0\nu\beta\beta$-decay) is another very promising way to determine the mass of neutrinos and also to reveal the Majorana nature of neutrinos. The $0\nu\beta\beta$-decay, $N(A,Z) \rightarrow N(A,Z+2) + 2e^-$ or $N(A,Z) \rightarrow N(A,Z-2) + 2e^+$, was first suggested by W. Furry in 1939 [42]. Since this process proceeds via the emission and absorption of

virtual Majorana neutrinos, it is only possible if the lepton number is violated and thus it is forbidden in the SM. The half life for the $0\nu\beta\beta$-decay is given by the expression [43]

$$\left(T_{1/2}^{0\nu}\right)^{-1} = G^{0\nu}(E_0, Z)|M(A, Z)|^2|m_{\beta\beta}|^2, \tag{1.3}$$

where $G^{0\nu}(E_0, Z)$ is a phase-space parameter, $M(A, Z)$ corresponds to the nuclear matrix element and $m_{\beta\beta} = \sum U_{ei}^2 m_i$ is the effective Majorana mass, with m_i the neutrino mass eigenstates and U_{ei} represent the mixing matrix elements between these mass eigenstates and the electron neutrino flavor eigenstates.

The lower bound for $0\nu\beta\beta$-decay was obtained in the germanium Heidelberg-Moscow experiment [44]

$$T_{1/2}^{0\nu}\left(^{76}Ge\right) \geq 1.55 \times 10^{25} \text{ years } (90\%CL), \tag{1.4}$$

giving an upper limit for the effective Majorana mass

$$|m_{\beta\beta}| \leq (0.3 - 1.2) \text{ eV}/c^2. \tag{1.5}$$

The CUORICINO experiment also reached similar sensitivity for the half life of ^{130}Te [45]

$$T_{1/2}^{0\nu}\left(^{130}Te\right) \geq 1.8 \times 10^{24} \text{ years } (90\%CL), \tag{1.6}$$

giving an upper limit for the effective Majorana mass

$$|m_{\beta\beta}| \leq (0.2 - 1.1) \text{ eV}/c^2. \tag{1.7}$$

Several future or ongoing experiments (CUORE, MAJORANA, EXO, SNO+, SUPER-NEMO and others) [46, 47] will focus their search on $0\nu\beta\beta$-decay aiming for a sensitivity for the effective Majorana mass down to $10^{-2}\ eV/c^2$.

1.7 A fourth neutrino generation?

Although the SM is consistent with the the 3 light neutrino family, a fourth neutrino family, usually called the sterile neutrino, has been discussed from time to time. The "LSND

anomaly" was observed by the LSND (Liquid Scintillator Neutrino Detector) collaboration [48, 49], operated from 1993-1998, as an excess on the predicted number of oscillated $\nu_\mu \rightarrow \nu_e$ neutrinos at lower energies.

The MiniBooNE [50, 51] experiment uses a 0.8 kiloton mineral oil Cerenkov detector and operates at FermiLab, is testing the significance of the "LSND anomaly". The 0.8 GeV neutrino beam for MiniBooNE is produced from the Booster Neutrino Beam smashing 8 GeV protons on a beryllium target and the secondary pion or kaons are focused by a magnetic horn. A 0.6 GeV antineutrino beam is also produced by reversing the polarity of the magnetic horn. Searching for $\nu_\mu \rightarrow \nu_e$ oscillations, MiniBooNE observed an anomalous excess of low energy electron-like events in charge current quasi elastic events over the standard neutrino interactions [51, 52]. An excess of events was also observed from the $\bar{\nu}_\mu \rightarrow \bar{\nu}_e$ search [53].

The results from MiniBooNE resulted more in confusion than clarification. The signal produced by electrons and converted photons is indistinguishable, and this hint could explain that the excess observed from LSND and MiniBooNE originates from converted photons, and not from electrons.

Chapter 2

Neutrino Oscillations

Neutrino oscillation is one of the most active research areas in neutrino physics today. Oscillations were first introduced by Pontecorvo in 1957 [7, 8]. This phenomenon is very crucial, since it will definitely prove to us, that, at least one neutrino type acquires some mass. However, the Standard Model considers the neutrinos to be massless, thus neutrino oscillations present an open window for new phenomena and perhaps even new physics beyond the Standard Model.

In simple words, neutrino oscillation is the transformation of a neutrino of a certain flavor into a neutrino of a different flavor. So, if for example we have initially a pure ν_μ, with energy E, then after traveling a distance L there is a non-zero probability that the neutrino will be detected as a ν_e.

2.1 Neutrino Oscillations In Vacuum

The weak eigenstates of neutrinos ν_α can be expressed as linear combinations of mass eigenstates ν_κ

$$|\nu_\alpha\rangle = \sum_{k=1}^{3} U^*_{\alpha k}|\nu_k\rangle, \tag{2.1}$$

where U is a unitary mixing matrix.

In the case of antineutrinos we merely replace U with U^*

$$|\bar{\nu}_\alpha\rangle = \sum_{k=1}^{3} U_{\alpha k}|\bar{\nu}_k\rangle. \tag{2.2}$$

This implies that if the mixing matrix is complex then CP is violated, and the oscillations of neutrinos and antineutrinos may be different.

We are looking for the probability to find a neutrino, produced initially in a flavor eigenstate $|\nu_\alpha\rangle$ and at a time t=0, in a state $|\nu_b\rangle$ at a later time t. At the production point and at t=0 we have the initial neutrino state given by the equation:

$$|\nu(t=0)\rangle = |\nu_\alpha\rangle = \sum_{k=1}^{3} U^*_{\alpha k}|\nu_k\rangle. \tag{2.3}$$

Using the Schrödinger equation,

$$i\frac{d}{dt}|\nu_\kappa(t)\rangle = H|\nu_\kappa(t)\rangle, \tag{2.4}$$

where H is the Hamiltonian. The massive neutrino states evolve as plane waves (plane wave approximation) [54, 55, 56]:

$$|\nu_\kappa(t)\rangle = e^{-iE_\kappa t}|\nu_\kappa\rangle. \tag{2.5}$$

The time evolution of this state is then

$$|\nu(t)\rangle = \sum_{k=1}^{3} U^*_{\alpha k} e^{-iE_k t}|\nu_k\rangle. \tag{2.6}$$

The probability of a flavor eigenstate neutrino ν_α to transform to another flavor eigenstate ν_b is

$$P(\nu_\alpha \to \nu_b, t) = |A(\nu_\alpha \to \nu_b, t)|^2, \tag{2.7}$$

where A is the probability amplitude given by

$$A(\nu_\alpha \to \nu_b, t) = \langle\nu_b|\nu(t)\rangle = U^*_{\alpha k} e^{-iE_k t}\langle\nu_b|\nu_k\rangle = U_{bi}U^*_{\alpha k}e^{-iE_k t}\langle\nu_i|\nu_k\rangle = U_{bk}e^{-iE_k t}U^*_{\alpha k}. \tag{2.8}$$

In the above relation $e^{-iE_k t}$ is the phase function describing the time evolution of the mass eigenstate neutrino ν_k in the energy representation, U_{bk} gives the amplitude to find the flavor neutrino state ν_b in the mass eigenstate ν_k and $U^*_{\alpha k} = U^\dagger_{k\alpha}$ is the amplitude to find the mass

eigenstate ν_k, with energy E_k, in the state of the flavor neutrino ν_α. From the expression of probability amplitude it is clear that transitions between flavor neutrinos can take place only if the mixing matrix U is non-diagonal and the phase factor e^{-iE_kt} is different for different neutrinos. Then the neutrino oscillation probability will take the form

$$P(\nu_\alpha \to \nu_b, t) = \left| U_{bk} e^{-iE_k t} U^*_{\alpha k} \right|^2 . \tag{2.9}$$

If neutrinos are massless or if there is no mixing ($U = 1$) then the transition probability is simply $P(\nu_\alpha \to \nu_b, t) = \delta_{\alpha b}$. Using the fact that neutrinos are relativistic particles with $m << p$ and also that massive neutrinos have the same momentum p we can write their energy as

$$E_k = \sqrt{p^2 + m^2} = p\sqrt{1 + \frac{m^2}{p^2}} = E + \frac{m^2}{2E} = E + \frac{m^2}{2E}. \tag{2.10}$$

Then the neutrino oscillation probability will take the form

$$P(\nu_\alpha \to \nu_b, t) = \left| U^*_{\alpha k} U_{bi} U_{\alpha i} U^*_{bk} \right| e^{-i\Delta m^2 \frac{t}{2E}}, \tag{2.11}$$

where $\Delta m^2 = m_k^2 - m_i^2$. Furthermore using the unitarity of matrix U

$$\begin{aligned} P(\nu_\alpha \to \nu_b, t) \;=\; & \sum_i |U_{\alpha i}|^2 |U_{bi}|^2 + \sum_{i \neq k} Re\left(U^*_{\alpha k} U_{bi} U_{\alpha i} U^*_{bk}\right) \cos\left(\frac{\Delta m^2 t}{2E}\right) + \\ & + \sum_{i \neq k} Im\left(U^*_{\alpha k} U_{bi} U_{\alpha i} U^*_{bk}\right) \sin\left(\frac{\Delta m^2 t}{2E}\right). \end{aligned} \tag{2.12}$$

The above probability can also be written as

$$\begin{aligned} P(\nu_\alpha \to \nu_b, t) \;=\; & \delta_{\alpha b} - 4 \sum_{i>k} Re\left(U^*_{\alpha k} U_{bi} U_{\alpha i} U^*_{bk}\right) \sin^2\left(\frac{\Delta m^2 t}{4E}\right) + \\ & + 2 \sum_{i>k} Im\left(U^*_{\alpha k} U_{bi} U_{\alpha i} U^*_{bk}\right) \sin\left(\frac{\Delta m^2 t}{2E}\right). \end{aligned} \tag{2.13}$$

In the case of antineutrinos one can merely replace the sign of the imaginary term.

If CPT holds then

$$P(\nu_\alpha \to \nu_b, t) = P(\bar{\nu}_b \to \bar{\nu}_\alpha, t), \tag{2.14}$$

and if CP is conserved

$$P(\nu_\alpha \to \nu_b, t) = P(\bar{\nu}_\alpha \to \bar{\nu}_b, t). \tag{2.15}$$

If CP is not conserved then the oscillation probabilities for neutrinos are different from those for antineutrinos. Together CPT and CP invariance are equivalent to time reversal T invariance

$$P(\nu_\alpha \to \nu_b, t) = P(\nu_b \to \nu_\alpha, t). \tag{2.16}$$

2.1.1 2 Flavor Oscillations

We consider first the case we have only two neutrino species ν_e and ν_μ. We can write the lepton mixing matrix as

$$U = \begin{pmatrix} \cos\theta_0 & \sin\theta_0 \\ -\sin\theta_0 & \cos\theta_0 \end{pmatrix} \tag{2.17}$$

with θ_0 the mixing angle. We can then express the flavor neutrino eigenstates as linear combinations of the mass eigenstates

$$|\nu_e\rangle = \cos\theta_0|\nu_1\rangle + \sin\theta_0|\nu_2\rangle, \tag{2.18}$$

$$|\nu_\mu\rangle = -\sin\theta_0|\nu_1\rangle + \cos\theta_0|\nu_2\rangle. \tag{2.19}$$

Then the probability of an electron neutrino to transform to a muon neutrino and vice versa is given by

$$P(\nu_e \to \nu_\mu, t) = P(\nu_\mu \to \nu_e, t) = \sin^2 2\theta_0 \sin^2\left(\frac{\Delta m^2 t}{4E}\right). \tag{2.20}$$

The survival probabilities for electron and muon neutrino are

$$P(\nu_e \to \nu_e, t) = P(\nu_\mu \to \nu_\mu, t) = 1 - P(\nu_e \to \nu_\mu, t). \tag{2.21}$$

In this case $\Delta m^2 = m_2^2 - m_1^2$. For relativistic neutrinos we can assume that $L \approx t$, where L is the distance traveled by neutrinos.

Defining the oscillation length as $l_{osc} = \frac{4\pi E}{\Delta m^2} \approx 2.47 \frac{E[GeV]}{\Delta m^2[eV^2]} m[km]$, we can write the

transition probability as

$$P(\nu_e \to \nu_\mu, L) = \sin^2 2\theta_0 \sin^2\left(\frac{L\pi}{l_{osc}}\right) = \sin^2 2\theta_0 \sin^2\left(\frac{1.27L[km]\Delta m^2[eV^2]}{E[GeV]}\right). \quad (2.22)$$

The first term in the above equation describes the amplitude of the neutrino oscillations and it does not depend on the distance traveled by neutrinos. When $\theta_0 = \frac{\pi}{4}$ we have maximal mixing, since the amplitude is maximal. If θ_0 is close to 0 or $\pi/2$, the flavor eigenstates are almost identical with the mass eigenstates and this corresponds to minimal mixing and the oscillation amplitude is small.

The second term in Equation 2.22 oscillates with the distance L traveled by neutrinos. The oscillation phase is proportional to the distance L and to the energy difference of the mass eigenstates $\Delta m^2/2E$. Thus, if we want to have a high transition probability, in addition to a large mixing, we should also have a large oscillation phase. For example, if the quantity L/E is extremely small, for any mass difference, then oscillation can not occur. And, if the oscillation phase is quite large, we will get very fast oscillations.

2.1.2 3 Flavor Oscillations

In this case, the lepton mixing matrix U will be a 3×3 matrix and the parametrization of this matrix will take a similar form as in the quark case. The mixing matrix U contains the three mixing angles (θ_{12}, θ_{13}, θ_{23}) and one CP-violation phase δ [57] [1]

$$U = \begin{pmatrix} c_{12}c_{13} & s_{12}c_{13} & s_{13}e^{-i\delta} \\ -s_{12}c_{23} - c_{12}s_{23}s_{13}e^{i\delta} & c_{12}c_{23} - s_{12}s_{23}s_{13}e^{i\delta} & s_{23}c_{13} \\ s_{12}s_{23} - c_{12}c_{23}s_{13}e^{i\delta} & -c_{12}s_{23} - s_{12}c_{23}s_{13}e^{i\delta} & c_{23}c_{13} \end{pmatrix}, \quad (2.23)$$

where $c_{ij} = \cos\theta_{ij}$ and $s_{ij} = \sin\theta_{ij}$. The oscillation probabilities will be the same, as previously given in Equation 2.13. However, in this case, they won't be as simple as they were in the two flavor case but we can make some approximations and get some simple formulas.

[1] In the case of Majorana neutrinos U must be multiplied by diag$(1, e^{i\alpha_1/2}, e^{i\alpha_2/2})$.

Considering that the neutrino mass differences $\Delta m^2_{ij} = m^2_i - m^2_j$ have an hierarchy

$$\left|\Delta m^2_{12}\right| << \left|\Delta m^2_{31}\right| \approx \left|\Delta m^2_{32}\right|, \tag{2.24}$$

this means that we can have $m_1 << m_2 << m_3$, called normal mass hierarchy, or $m_3 << m_1 << m_2$, called inverted mass hierarchy.

The limit $\Delta m^2_{21} \to 0$ applies quite well to the atmospheric, accelerator and reactor neutrino oscillation experiments. The transition probability takes then a simple form, very similar to the one in the two neutrino case.

Another limiting case is when we assume $U_{e3} = 0$ or $|U_{e3}| << 1$ (i.e. $\theta_{13} \approx 0$) and we can get again very simple relations, similar to the one in the two neutrino case.

2.2 Neutrinos Oscillations In Matter

In the previous section we have considered oscillations of neutrinos in vacuum, but the oscillation of neutrinos in matter can be quite different; matter can affect the phenomenon of neutrino oscillations. This is because matter consists of quarks and electrons. The scattering process between quarks and neutrinos involves only the exchange of Z^0 (neutral current interactions). This contribution is not very important, since the contribution of quarks to the scattering amplitude is the same for all neutrino flavors. However, electron-neutrino scattering is quite different. Neutral weak current gives again identical scattering amplitudes for all neutrino flavors but there are some differences for the charged weak current. This is because the corresponding scattering of electron neutrinos with electrons can also take place via $W^{\pm}$ exchange (charge current interactions).

For the charge current case the interaction is described by the Hamiltonian

$$H_{cc} = \frac{G_F}{\sqrt{2}}[\bar{e}\gamma_\mu(1-\gamma_5)\nu_e][\bar{\nu}_e\gamma^\mu(1-\gamma_5)e]. \tag{2.25}$$

Here G_F is the Fermi coupling constant of the weak interaction. Using a Fierz transformation we can write the above Hamiltonian as

$$H_{cc} = \frac{G_F}{\sqrt{2}}[\bar{\nu}_e\gamma_\mu(1-\gamma_5)\nu_e][\bar{e}\gamma^\mu(1-\gamma_5)e]. \tag{2.26}$$

The effective energy of neutrinos will then have an extra term of the form $\langle e\nu|H_{cc}|e\nu\rangle$. Since for left-handed neutrinos $\langle\nu|\bar{\nu}\gamma^0(1-\gamma_5)\nu|\nu\rangle = 2$, and for electrons at rest or moving very slowly $\langle e|\bar{e}\gamma^\mu(1-\gamma_5)e|e\rangle = N_e\delta_{\mu 0}$, this term will finally contribute an additional potential for the electron neutrinos $V = \sqrt{2}G_F N_e$, with N_e the electron density. In the case of antineutrinos the sign of V is opposite.

In vacuum, for the two neutrino case the evolution equation in the mass eigenstate basis is $i(d/dt)|\nu_m\rangle = H_m|\nu_m\rangle$, where $H_m = diag(E_1, E_2)$. Moving in the flavor basis ($\nu_{fl} = U\nu_m$) the Hamiltonian is no longer diagonal and the evolution equation becomes $i(d/dt)|\nu_{fl}\rangle = H_{fl}|\nu_{fl}\rangle = UH_mU^\dagger|\nu_{fl}\rangle$.

For example, consider the two neutrino case in vacuum with $\nu_e = \cos\theta_0\nu_1 + \sin\theta_0\nu_2$ and $\nu_\mu = -\sin\theta_0\nu_1 + \cos\theta_0\nu_2$. Then $\nu_1 = \cos\theta_0\nu_e - \sin\theta_0\nu_\mu$ and $\nu_2 = \sin\theta_0\nu_e + \cos\theta_0\nu_\mu$. These states in vacuum, as mentioned above, are eigenstates of the Hamiltonian giving

$$i\frac{d}{dt}\begin{pmatrix}\nu_1\\ \nu_2\end{pmatrix} = \frac{1}{2E}\begin{pmatrix}m_1^2 & 0\\ 0 & m_2^2\end{pmatrix}\begin{pmatrix}\nu_1\\ \nu_2\end{pmatrix}. \tag{2.27}$$

But, in the flavor basis the Hamiltonian is no longer diagonal:

$$i\frac{d}{dt}\nu_e = \frac{1}{2E}[(m_1^2\cos^2\theta_0 + m_2^2\sin^2\theta_0)\nu_e + (m_2^2 - m_1^2)\sin\theta_0\cos\theta_0\nu_\mu], \tag{2.28}$$

$$i\frac{d}{dt}\nu_\mu = \frac{1}{2E}[(m_2^2 - m_1^2)\sin\theta_0\cos\theta_0\nu_e + (m_1^2\sin^2\theta_0 + m_2^2\cos^2\theta_0)\nu_\mu]. \tag{2.29}$$

Writing

$$(m_1^2\cos^2\theta_0 + m_2^2\sin^2\theta_0) = -\frac{1}{2}(m_2^2 - m_1^2)(\cos^2\theta_0 - \sin^2\theta_0) + \frac{1}{2}(m_2^2 + m_1^2), \tag{2.30}$$

we find

$$i\frac{d}{dt}\begin{pmatrix}\nu_e\\ \nu_\mu\end{pmatrix} = \begin{pmatrix}-\frac{\Delta m^2}{4E}\cos 2\theta_0 & \frac{\Delta m^2}{4E}\sin 2\theta_0\\ \frac{\Delta m^2}{4E}\sin 2\theta_0 & \frac{\Delta m^2}{4E}\cos 2\theta_0\end{pmatrix}\begin{pmatrix}\nu_e\\ \nu_\mu\end{pmatrix}, \tag{2.31}$$

where we have neglected a term $\left(p + \frac{m_1^2+m_2^2}{4E}\right)$ in the diagonal terms, which does not contribute to the phase differences of neutrino oscillations. Then, the evolution equation which

describes the transition of an electron neutrino to muon neutrino and vise versa, in matter, becomes

$$i\frac{d}{dt}\begin{pmatrix}\nu_e\\ \nu_\mu\end{pmatrix}=\begin{pmatrix}-\frac{\Delta m^2}{4E}\cos 2\theta_0+\sqrt{2}G_F N_e & \frac{\Delta m^2}{4E}\sin 2\theta_0\\ \frac{\Delta m^2}{4E}\sin 2\theta_0 & \frac{\Delta m^2}{4E}\cos 2\theta_0\end{pmatrix}\begin{pmatrix}\nu_e\\ \nu_\mu\end{pmatrix}. \tag{2.32}$$

For constant density, N_e, it is easy to solve the above equation. Diagonalizing the above matrix will give us the neutrino eigenstates in matter

$$|\nu_{1m}\rangle=\cos\theta|\nu_e\rangle+\sin\theta|\nu_\mu\rangle, \tag{2.33}$$

$$|\nu_{2m}\rangle=-\sin\theta|\nu_e\rangle+\cos\theta|\nu_\mu\rangle. \tag{2.34}$$

The new mixing angle θ is related to the vacuum mixing angle with the following equation (for antineutrinos simply change the denominator minus sign with a plus sign)

$$\tan 2\theta=\frac{\frac{\Delta m^2}{2E}\sin 2\theta_0}{\frac{\Delta m^2}{2E}\cos 2\theta_0-\sqrt{2}G_F N_e}. \tag{2.35}$$

Obviously, if the electron density N_e vanishes then matter oscillations coincide with vacuum oscillations ($\theta=\theta_0$). However, for an infinite density N_e, we have $\theta=0$ or $\theta=\pi/2$ and in this case the matter eigenstates are given by the flavor eigenstates.

From the form of the eigenstates of neutrinos in matter, we conclude that matter oscillations can be very similar to oscillations in vacuum. They can only occur if neutrinos acquire a mass and mix. So the transition probability in matter, has the same form as in vacuum

$$P(\nu_e\to\nu_\mu,L)=\sin^2 2\theta\sin^2\left(\frac{L\pi}{l_m}\right), \tag{2.36}$$

where in this case the oscillation length has the form

$$l_m=\frac{4\pi E}{\Delta m^2_M}=\frac{4\pi E}{\sqrt{\left(\frac{\Delta m^2}{2E}\cos 2\theta_0-\sqrt{2}G_F N_e\right)^2+\left(\frac{\Delta m^2}{2E}\right)^2\sin^2 2\theta_0}}, \tag{2.37}$$

with Δm^2_M the squared-mass difference in matter.

The probability that an electron neutrino is found to be unchanged after crossing a distance l in matter is

$$P(\nu_e \to \nu_e, L) = 1 - \sin^2 2\theta \sin^2\left(\frac{L\pi}{l_m}\right). \tag{2.38}$$

An important parameter is the oscillation amplitude given by

$$\sin^2 2\theta = \frac{\left(\frac{\Delta m^2}{2E}\right)^2 \sin^2 2\theta_0}{\left(\frac{\Delta m^2}{2E}\cos 2\theta_0 - \sqrt{2}G_F N_e\right)^2 + \left(\frac{\Delta m^2}{2E}\right)^2 \sin^2 2\theta_0}. \tag{2.39}$$

The left-hand side has a maximum when $\theta = \pi/4$, achieved by the condition known as the MSW resonance condition

$$\frac{\Delta m^2}{2E}\cos 2\theta_0 = \sqrt{2}G_F N_e. \tag{2.40}$$

Thus, we have a separation between matter and vacuum oscillations, as even for very small vacuum mixing angles θ_0, we can have maximal mixing in matter.

We can apply this MSW effect and find a very elegant solution to the solar neutrino problem. This problem arises from the fact that less solar electron neutrinos than expected were observed [58]. Solar electron neutrinos are produced in the Sun by nuclear reactions. No muon or tau neutrinos are produced.

From the MSW resonance condition we can find the MSW resonance density

$$N_e^{res} = \frac{\Delta m^2 \cos 2\theta_0}{2\sqrt{2}EG_F}. \tag{2.41}$$

The electron density has a large value in the core of the Sun and becomes zero at the edge of the Sun. The resonance condition can then be satisfied by a wide range of values of $E/\Delta m^2$. Electron neutrinos begin their "journey" from the core of the Sun to the outer edge of the Sun. In some areas the electron density satisfies the resonance condition giving a non-zero probability for the electron neutrino to transform to a muon neutrino. But, the electron neutrino can reach the resonance region if its energy is greater than the energy needed to satisfy the resonance condition at the density at the center of the Sun. The

minimum energy for this purpose is

$$E_{min} = \frac{\Delta m^2 \cos 2\theta_0}{2\sqrt{2} G_F N_e(0)}. \tag{2.42}$$

Since neutrinos leave the Sun as a combination of the states ν_e and ν_μ, we can have a simple description in the case of the adiabatic approximation. From the adiabatic theorem of quantum mechanics, it follows, that for a slow variation of the Hamiltonian the basis states change, but no transitions between the individual states are induced. The system remains in the original (time-dependent) eigenstate.

Thus, in the case of adiabatic approximation the density changes very slowly. In the core of the Sun the electron density is infinite and the heavier mass eigenstate is an electron neutrino eigenstate. As the neutrino travels to the outer part of the Sun the amount of electron density decreases, the mass neutrino eigenstates become a combination of the two neutrino flavor eigenstates depending on the mixing angle θ. The resonance case occurs for an average density ($\theta = \pi/4$). According to the adiabatic theorem, the electron neutrino generated in a mass eigenstate remains in this state and eventually leaves the Sun as a muon neutrino.

2.3 Neutrino Oscillations and T2K

T2K is a long baseline neutrino oscillation experiment. A powerful proton beam at the J-PARC accelerator centre in Japan is producing a neutrino beam targeting the Super-Kamiokande detector 295 km away. With an expected sensitivity of about an order of magnitude better than any other current neutrino oscillation experiment, T2K aims to measure the $\nu_\mu \rightarrow \nu_e$ oscillation and eventually to measure θ_{13}, the only unknown mixing angle in the PMNS neutrino mixing matrix in Equation 2.23. Also if θ_{13} is non-zero, T2K will be able to measure or put some limits on the CP violation in the leptonic sector. Finally, T2K will also measure with much better precision the atmospheric oscillation parameters θ_{23} and Δm^2_{23}. More about T2K can be found in the next chapter; this section covers basic neutrino oscillation phenomenology for T2K.

In T2K we are particularly interested in the ν_μ disappearance probability $P(\nu_\mu \rightarrow \nu_\mu)$,

and the ν_e appearance probability $P(\nu_\mu \rightarrow \nu_e)$. Using the 3×3 neutrino mixing matrix 2.23 and with the help of Equation 2.13, the exact formulas, neglecting matter effects, for the neutrino disappearance and appearance probabilities can be written as

$$\begin{aligned} P(\nu_\mu \rightarrow \nu_\mu) &= 1 - 4S_{23}^2C_{13}^2\left(C_{12}^2C_{23}^2 + S_{12}^2S_{13}^2S_{23}^2 - 2C_{12}C_{23}S_{12}S_{13}S_{23}\cos\delta\right)\sin^2\Delta_{23} \\ &\quad - 4S_{23}^2C_{13}^2\left(S_{12}^2C_{23}^2 + C_{12}^2S_{13}^2S_{23}^2 + 2C_{12}C_{23}S_{12}S_{13}S_{23}\cos\delta\right)\sin^2\Delta_{13} \\ &\quad - 4\left(C_{12}^2C_{23}^2 + S_{12}^2S_{13}^2S_{23}^2 - 2C_{12}C_{23}S_{12}S_{13}S_{23}\cos\delta\right) \\ &\quad \times \left(S_{12}^2C_{23}^2 + C_{12}^2S_{13}^2S_{23}^2 + 2C_{12}C_{23}S_{12}S_{13}S_{23}\cos\delta\right)\sin^2\Delta_{12}, \end{aligned} \tag{2.43}$$

$$\begin{aligned} P(\nu_\mu \rightarrow \nu_e) &= 4C_{13}^2S_{13}^2S_{23}^2\sin^2\Delta_{31} \\ &\quad + 8C_{13}^2S_{12}S_{13}S_{23}\left(C_{12}C_{23}\cos\delta - S_{12}S_{13}S_{23}\right)\cos\Delta_{32}\sin\Delta_{31}\sin\Delta_{21} \\ &\quad - 8C_{13}^2C_{12}C_{23}S_{12}S_{13}S_{23}\sin\delta\sin\Delta_{32}\sin\Delta_{31}\sin\Delta_{21} \\ &\quad + 4S_{12}^2C_{13}^2\left(C_{12}^2C_{23}^2 + S_{12}^2S_{23}^2S_{13}^2 - 2C_{12}C_{23}S_{12}S_{23}S_{13}\cos\delta\right)\sin^2\Delta_{21}. \end{aligned} \tag{2.44}$$

Here, $\Delta_{ij} = \frac{1.27\Delta m_{ij}^2}{eV^2}\frac{L}{km}\frac{GeV}{E_\nu}$ and $c_{ij} = \cos\theta_{ij}$, $s_{ij} = \sin\theta_{ij}$.

Equations 2.43 and 2.44 depend on three unknown parameters. The first is the mixing angle θ_{13} which T2K is optimized to measure. The second is the CP-violation phase δ. From the PMNS mixing matrix, the CP-violation phase is always associated with the $\sin\theta_{13}$ term. Thus, in the case that θ_{13} is relatively large, T2K can put some limits on the value of the CP-violation δ parameter. The other unknown parameter is related to the neutrino mass hierarchy, Figure 2.1. The leading terms on both Equations 2.43 and 2.44 are not sensitive to the sign of the neutrino mass ordering. For long baselines matter effects provide a solution to this in the case that $\theta_{13} \neq 0$. However, T2K is not sensitive to matter effects.

The neutrino oscillation probabilities are strongly dependent on L/E. At the T2K peak neutrino energy $\sim$ 0.7 GeV and for the T2K distance at 295 km the first oscillation mini-

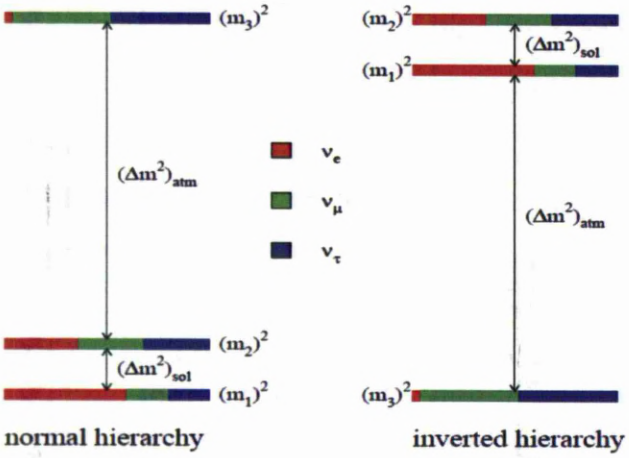

Figure 2.1: The neutrino mass hierarchy scheme. Normal mass hierarchy is on the left inverted mass hierarchy on the right.

parameter	$bf \pm 1\sigma$	2σ range	3σ range
$\Delta m^2_s(10^{-5}eV^2)$	$7.59^{+0.23}_{-0.18}$	$7.22 - 8.03$	$7.03 - 8.27$
$\lvert\Delta m^2_A\rvert(10^{-3}eV^2)$	$2.40^{+0.12}_{-0.11}$	$2.18 - 2.64$	$2.07 - 2.75$
$\sin^2\theta_{12}$	$0.318^{+0.019}_{-0.016}$	$0.29 - 0.36$	$0.27 - 0.38$
$\sin^2\theta_{23}$	$0.50^{+0.07}_{-0.06}$	$0.39 - 0.63$	$0.36 - 0.67$
$\sin^2\theta_{13}$	$0.013^{+0.013}_{-0.009}$	≤ 0.039	≤ 0.053

Table 2.1: Recent values for neutrino oscillation parameters, giving best fit value and 2σ, 3σ range. From [59].

mum for the disappearance case and the first oscillation maximum for the appearance case are accessible, Figures 2.2 and 2.3. The corresponding neutrino oscillation probabilities as a function of the neutrino energy, for the T2K distance of 295 km, are shown in Figures 2.4 and 2.5. The expected sensitivity of θ_{13}, as a function of Δm^2_{23}, for the full T2K operation at 5×10^{21} protons on target (POT) is shown in Figure 2.6 [60]. The values for the neutrino oscillation parameters are taken from Table 2.1 [59].

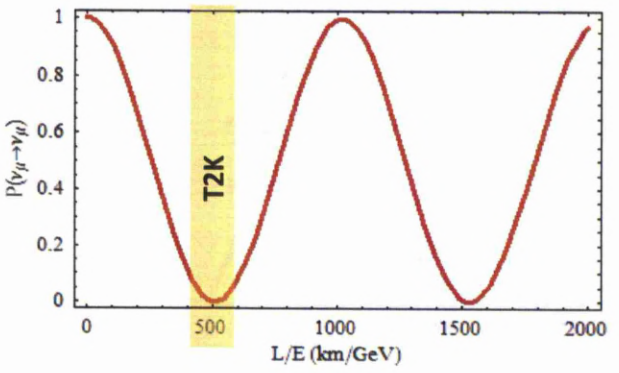

Figure 2.2: The muon neutrino disappearance oscillation probability as a function of the L/E. Plot using Equation 2.43 with the best fit oscillation parameters from Table 2.1 and $\delta_{CP} = 0$.

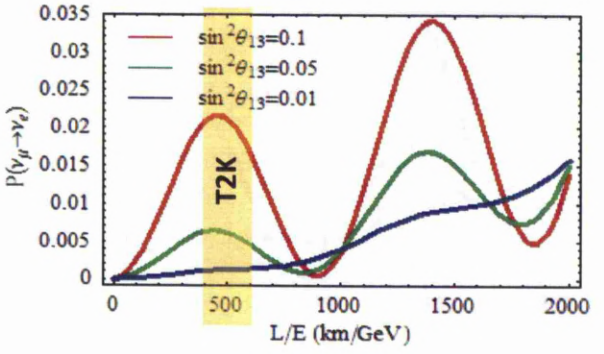

Figure 2.3: The electron neutrino appearance oscillation probability as a function of the L/E. Plot using Equation 2.44 with the best fit oscillation parameters from Table 2.1, $\delta_{CP} = 0$ and three different values for the unknown θ_{13}.

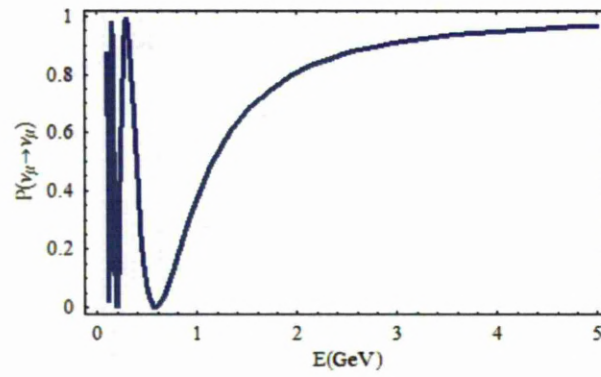

Figure 2.4: The muon neutrino disappearance oscillation probability as a function of the neutrino energy for L=295 km. Plot using Equation 2.43 with the best fit oscillation parameters from Table 2.1 and $\delta_{CP} = 0$.

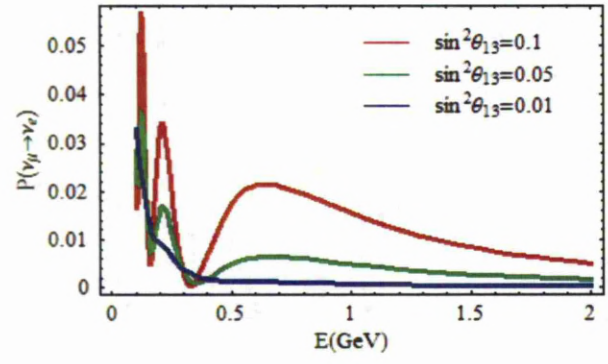

Figure 2.5: The electron neutrino appearance oscillation probability for 3 different values of θ_{13} as a function of the neutrino energy for L=295 km. Plot using Equation 2.44 with the best fit oscillation parameters from Table 2.1 and $\delta_{CP} = 0$.

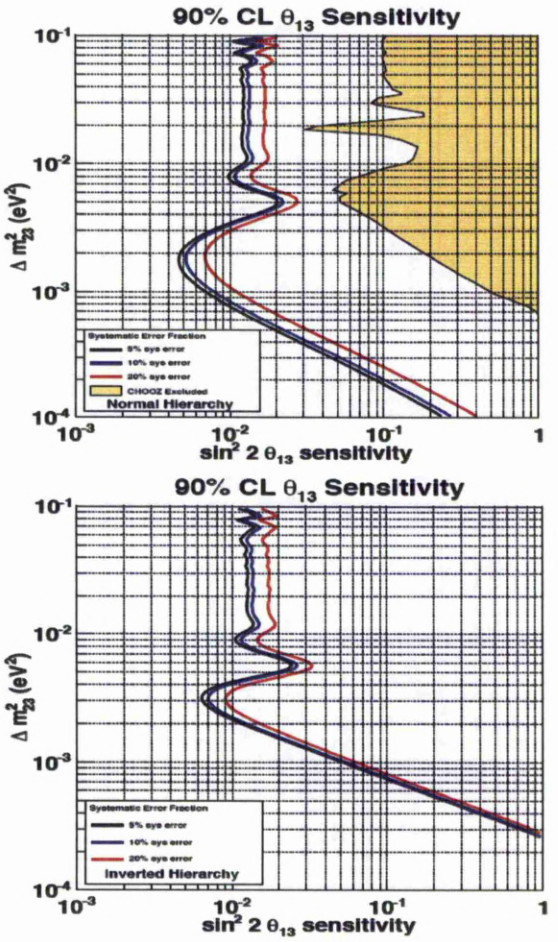

Figure 2.6: Expected θ_{13} sensitivity at 90 % CL for T2K for 5×10^{21} POT. Normal(Inverted) hierarchy on top(bottom). From[60]

Chapter 3

The T2K long baseline neutrino oscillation experiment

The newly constructed accelerator facility at J-PARC, on the east coast of Japan, is used to produce an intense narrow-band off-axis neutrino beam towards the Super-Kamiokande detector located 295 km away on the west side of Japan. Choosing an off-axis angle of 2.5^o, the neutrino beam will have a narrow energy spread at 0.7 GeV around the oscillation maximum for the 295 km distance.

T2K aims for an intensive search for the unknown θ_{13} mixing angle by searching for the rare $\nu_\mu \rightarrow \nu_e$ oscillations and, if this angle is large enough to also search for possible CP violation in the lepton sector. It also aims to make a precise measurement of the muon neutrino disappearance. Two more detectors are located near the neutrino beam at 280 m. INGRID is located on-axis and its purpose is to monitor and profile the neutrino beam. ND280 is located at 2.5^o off-axis and is designed to measure the neutrino beam, determine the ν_e beam contamination and to measure various cross sections.

Construction and commission of the beam and near and far detectors have been completed near the end of 2009 and first data was collected at the beginning of 2010 and ran approximately for 6 months. The detector operation stopped for a few weeks, to upgrade the beam line and install the barrel ECal modules in ND280. T2K entered in phase-II in early November of 2010 and continued until the March 2011 earthquake, accumulating in total 1.43×10^{20} protons on target (POT).

3.1 The Neutrino Beam

The J-PARC Linear Accelerator (Linac) produces a 190 MeV energy proton beam. The proton beam enters the Rapid Cycling Synchrotron (RCS) to accelerate to 3 GeV. The proton beam then enters the proton synchrotron (PS) to accelerate to 30 GeV. With the combined help of dipole and quadrapole superconducting magnets the proton beam is bent and enters the ARC site. The proton design intensity of the PS is 3.3×10^{14} protons/pulse at a rate of 0.31 Hz. The proton beam is extracted in spills of 5.6 μs. Each spill has six bunches for Run-I or eight bunches for Run-II, each of length 58 ns.

The protons are smashed onto a high pressure helium cooled cylindrical graphite target producing a large number of hadrons. The target has diameter 0.3 cm and 90 cm length. The target is located inside the first of three magnetic horns which focus the positive hadrons. The hadrons are pions with a small contamination of kaons. The focused pions are directed to the 110 m decay volume filled with 1 atm helium gas in order to reduce the pion absorption and tritium production. Some of the pions will stop in the decay volume walls, but a very large fraction will decay to a muon and a ν_μ, producing the neutrino flux. Some of the resulting muons will also decay, $\mu^+ \rightarrow e^+ + \nu_e + \bar{\nu}_\mu$ contaminating the beam with a small fraction of $\bar{\nu}_\mu$ and ν_e. A fraction of the kaons decay, $K^+ \rightarrow \pi^0 + e^+ + \nu_e$ and $K_L^0 \rightarrow \pi^\pm + e^\pm + \nu_e(\bar{\nu}_e)$, resulting in a small ν_e beam contamination. Electron neutrinos from kaon decay contaminate the ν_e spectrum at high energies, while ν_e at lower energies are mostly produced from muon decay. The length of the decay volume is carefully chosen so as to maximize the pion decay and minimize the muon decay.

At the end of the decay volume a beam dump is used to stop the remaining hadrons that did not decay. The beam dump is constructed out of graphite blocks cooled with water in aluminum pipes.

In addition to neutrinos high energy muons will also exit the decay volume. Thus, downstream of the decay volume a muon monitor (MUMON) is placed. Detecting these high energy muons, MUMON can be used as a neutrino beam monitor and also as a proton beam and horn monitor. The MUMON consists of silicon detectors and ionization chambers.

With the current construction and using pion decay kinematics, T2K is using an off-axis beam configuration to produce a narrow band neutrino beam. The off-axis angle is chosen to be 2.5^o with respect to far detector, leading to a narrow neutrino beam peaking around 0.7 GeV. The T2K beam complex is illustrated in Figure 3.1 [61].

3.2 The Far Detector: Super-Kamiokande

Super-Kamiokande (SK) is located under the Ike mountain 295 km southeast from the J-PARC facilities. It is the largest water Cerenkov detector in the world, with 41.4 m height and 39.3 m diameter. It is built vertically to the ground and can hold 50 kilo-tonnes of water. SK is divided into an external and internal part. The internal part is separated by plastic sheets and has dimensions 36.2 m high and 33.8 m diameter. The external part of the SK detector acts as a veto for interactions that may happen around the detector area. If signal is recorded in the outer part of the detector and not in the internal part, then this is considered to be an event coming from outside the detector rather as a neutrino interaction event. Additionally, a fiducial volume cut is applied at 22.5 kilo-tonnes of water to remove cosmic muon events and radioactivity around the detector.

The construction of the SK is completed with 11446 20 inch diameter photomultipliers (PMT), installed in the internal part of the SK facing to the center of the detector. 1885 8-inch diameter PMTs are installed in the external part of SK facing to the outer part of the detector. The detector electronics are located on the top of the detector. A view of the SK detector is shown in Figure 3.2.

When a relativistic charged particle travels in a medium, it polarizes the molecules along its path. If the particle's velocity is largest than the speed of light in the medium, then as the molecules become depolarized they emit radiation. A cone will be created around the particle's direction of motion from the produced photons. The opening angle of the cone is depending on the particle's velocity u and on the refractive index of the medium n and it can be written as

$$\cos\theta = \frac{1}{\beta n}, \tag{3.1}$$

with $\beta = u/c$ and $\beta > \frac{1}{n}$. For water $n = 1.34$.

The light is detected by the photomultipliers of the internal part of the detector, form-

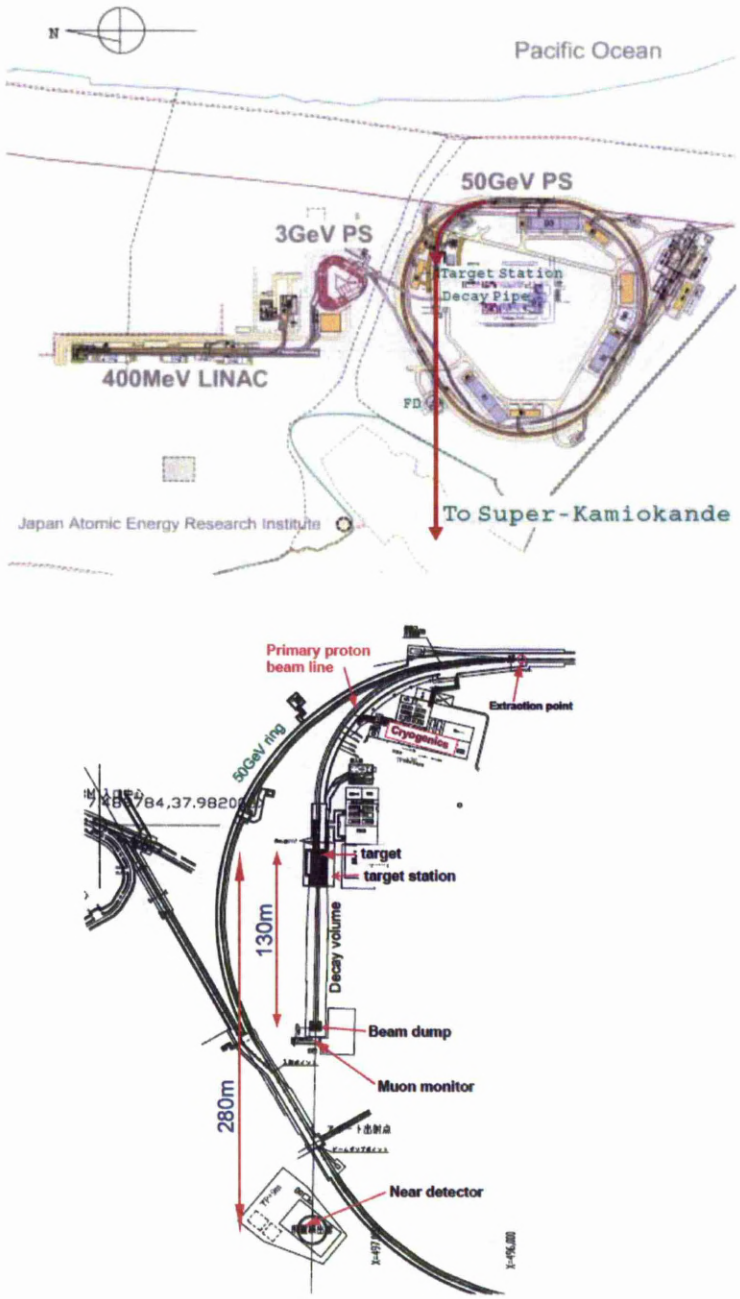

Figure 3.1: The T2K beam complex. From [61].

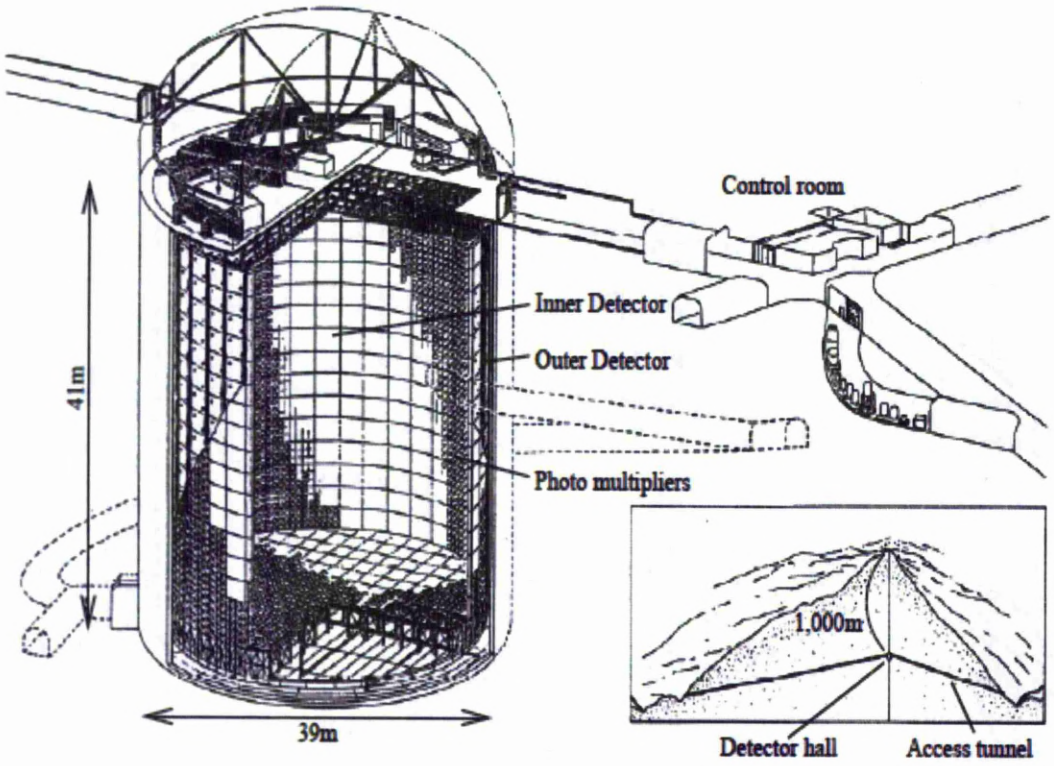

Figure 3.2: A schematic view of the Super-Kamiokande detector.

ing a circular object (ring). Different type of charged particles will produce different ring shapes. Muons and pions produce sharp rings called μ-like ring. On the other hand, electrons scatter more with matter and produce more fuzzy rings, called e-like ring. Timing information makes it possible to distinguish muon decay events, since an electron-like ring follows a muon-like ring. Neutral pions, can be distinguished since they decay to two photons. The photons produce an electron-positron pair and they are visible as electron-like events. If these two showers are very close to each other, they can easily mimic a single electron event. Protons produced by neutrino interactions are usually below the Cerenkov threshold and they are invisible.

3.2.1 Event selection at the Super-Kamiokande detector

The selection of the ν_μ or ν_e candidates first requires a fully contained (FC) reconstructed interaction vertex inside the fiducial volume (FV). The FV is defined as a cylinder with

	Data	ν_μ CC	ν_e CC	NC	$\nu_\mu \rightarrow \nu_e$ CC
interaction in FV	n/a	67.2	3.1	71.0	6.2
fully-contained FV	88	52.4	2.9	18.3	6.0
single ring	41	30.8	1.8	5.7	5.2
e-like	8	1.0	1.8	3.7	5.2
$E_{vis} > 100$ MeV	7	0.7	1.8	3.2	5.1
no delayed electrons	6	0.1	1.5	2.8	4.6
non-π^0-like	6	0.04	1.1	0.8	4.2
$E_\nu^{rec} < 1250$ MeV	6	0.03	0.7	0.6	4.1

Table 3.1: Analysis summary and selection of CC $\nu_\mu \rightarrow \nu_e$ candidates selected at T2K after 1.43×10^{20} protons on target and comparison with the MC [62]. For the CC MC three neutrino oscillations are considered with $\sin^2 2\theta_{13} = 0.1$ and $\delta_{CP} = 0$.

a distance of 200 cm from the boundaries of the inner detector. An event is classified as FC if it deposits at least 30 MeV of visible energy from all the reconstructed Cerenkov rings only in the inner detector and has no energy deposit at the outer detector. The FC sample can then be divided into single or multi ring μ-like or e-like events. A selection of single and multi-ring muon-like event displays from Run-I are shown in Figure 3.3. The particle identification is applied on the most energetic ring and then the event is classified as μ-like or e-like. A special cub-category of the multi-ring e-like events is the case of only two e-like rings and with no decay candidates. This event is selected as a neutral current π^0 candidate. The candidate is then confirmed as a true neutral current π^0 event if the invariant mass of the π^0 is in the range 85 MeV/c^2-185 MeV/c^2.

During the first year of data taking, T2K has selected 6 $\nu_\mu \rightarrow \nu_e$ candidates, indicating a non-zero θ_{13} mixing angle. The results and an analysis summary are shown on Table 3.1 [62].

3.3 The on axis INGRID near detector

The Interactive Neutrino Grid (INGRID) is located 280 m from the target and it consists of 16 independent detectors, from which 14 are aligned 7 and 7 in cross shape construction. The two center modules are aligned according to the beam center. The remaining two modules are placed on the two corners of the cross shape construction in order to check the symmetry in the profile of the neutrino beam (see Figure 3.4). Each module consists of

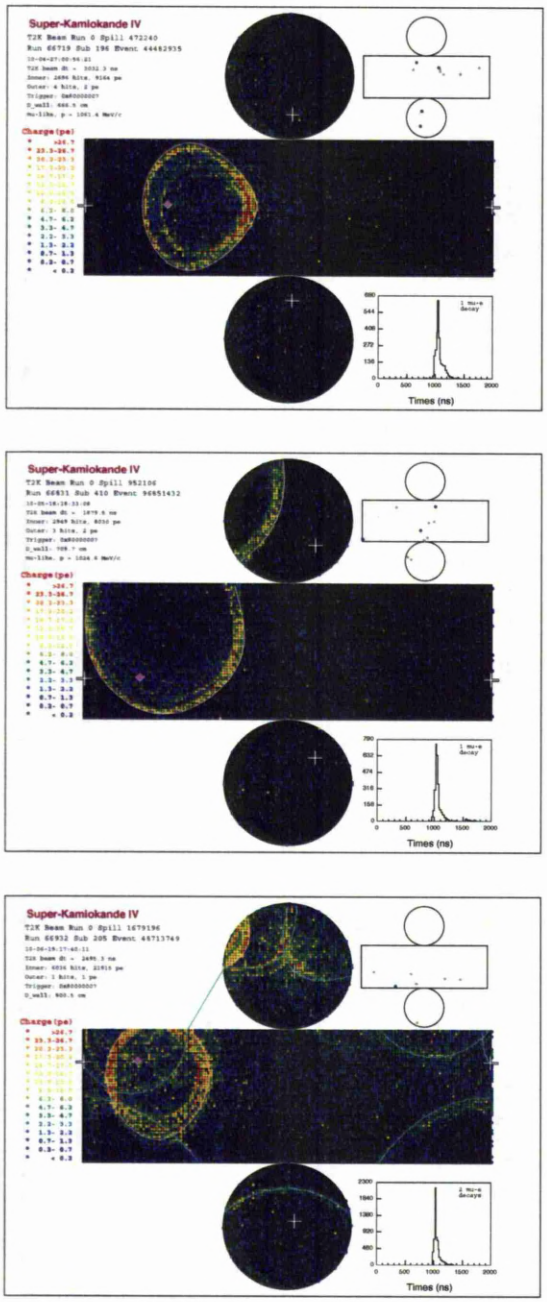

Figure 3.3: The event displays are showing single (top and middle) and multi ring (bottom) muon like events from Run-I (January-June 2010) dataset. The crosses on the event display show the reconstructed vertex position. The histogram at the bottom of each event display shows the hit time useful for the Michel electron tagging.

11 scintillating plastic bar layers alternating with 9 thick iron planes, and has dimensions $1 \times 1 \times 1$ m. Four additional veto planes are placed on the side of each module. INGRID's main purpose is to profile, on a daily basis, the neutrino flux within 1 mrad corresponding to a 2 % shift of the off-axis neutrino beam spectrum.

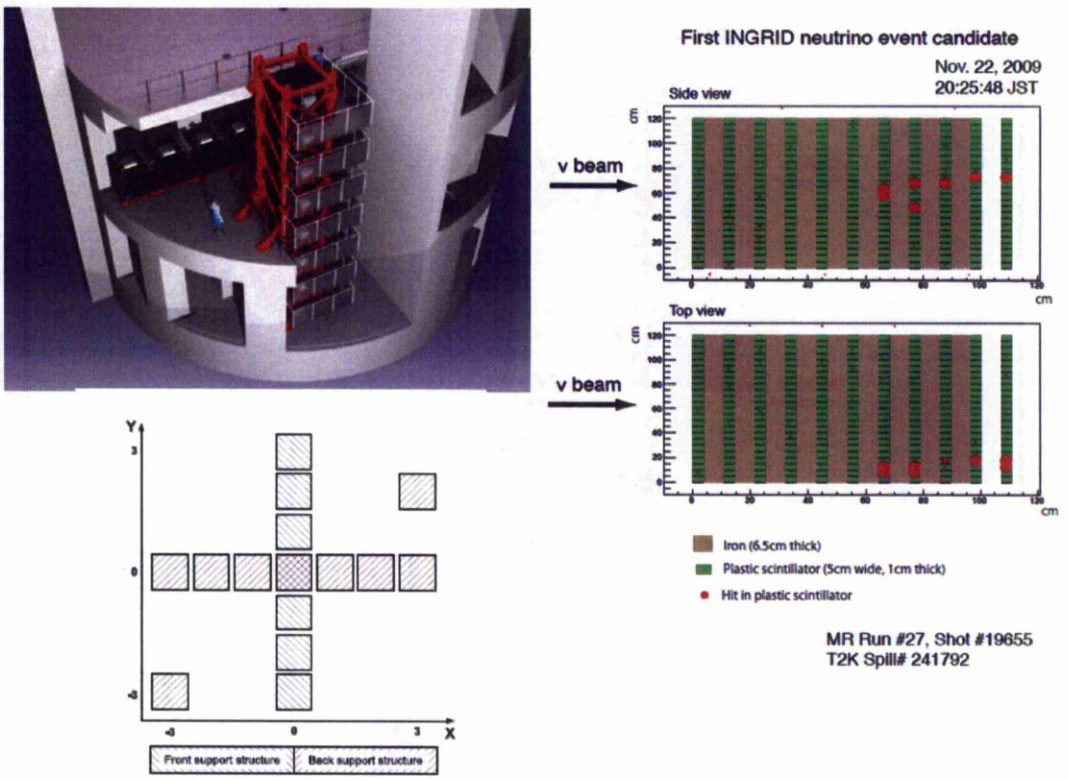

Figure 3.4: The INGRID near detector on the top left, the layout of the INGRID modules on the bottom left and the first T2K neutrino event observed at the bottom-most INGRID module on the right.

3.4 The off-axis near detector ND280

The off-axis near detector ND280 is actually a detector complex. The central region of the off axis complex is contained inside a metallic basket, with dimensions $6.5 \times 2.6 \times 2.5$ m, and consists of a π^0 detector (P0D), two fine grained detectors (FGD) and three time projection chambers (TPC), each following the P0D and the FGDs. The basket is surrounded by the electromagnetic calorimeter (ECal) and surrounding in the recycled UA1

magnet embedded with a side muon range detector (SMRD). An exploded view of the ND280 detector complex is shown on Figure 3.5.

The UA1/NOMAD magnet provides a magnetic field at 0.2 T. It is made of two identical halves each consist of 8 C-shaped parts. Each half consists of water cooled aluminum foils. The total weight of the magnet yoke is 850 tonnes. The magnet has inner dimensions $3.5 \times 3.5 \times 7$ m and external dimensions $5.6 \times 6.1 \times 7.6$ m. The presence of the magnetic field will help the physics analysis to determine the sign of the charge particles produced from neutrino interactions and also to measure their momentum with a good resolution.

The event display in Figure 3.6 shows a multi-track neutrino interaction in the P0D. A long track starting in the P0D, crosses the whole ND280 detectors, passes through the TPCs, FGDs and the DsECal.

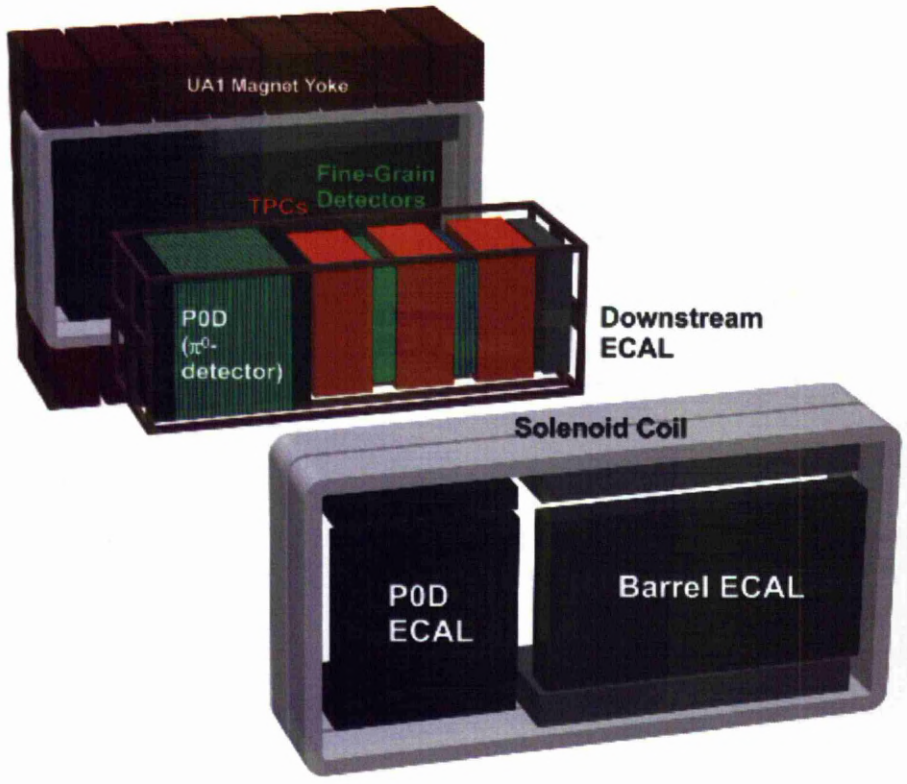

Figure 3.5: The ND280 detector complex.

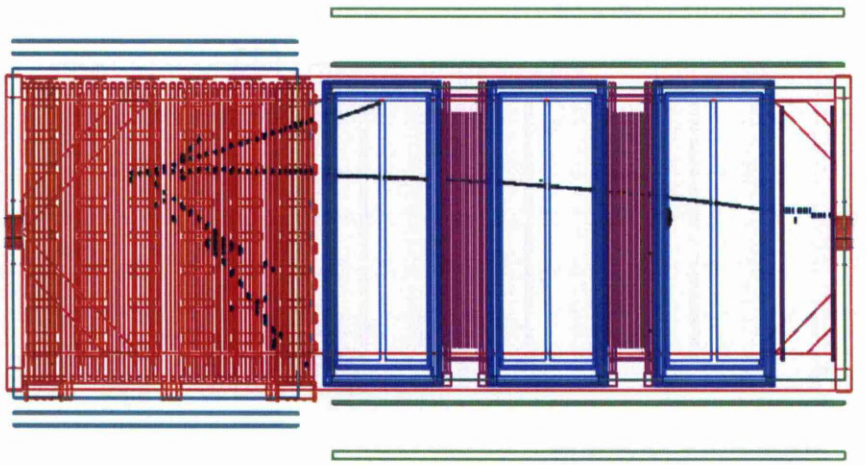

Figure 3.6: ND280 event display showing a multi-track neutrino interaction in the P0D. A long track starting in the P0D passes through the TPCs and the FGDs and goes in the DsECal.

3.4.1 The π-zero detector (P0D)

As it name suggests, P0D is specifically built to measure the neutrino π^0 interactions, focusing on the NC single π^0 channel. The necessity to measure this cross section is coming from the fact that it is a major background channel for the ν_e oscillation analysis at Super-Kamiokande. The cross section with the P0D full and empty of water will be measured, and the statistical subtraction of the two will give the event rate on water.

The P0D is located upstream in the ND280 detector complex and has dimensions $220 \times 234 \times 242$ cm. It is a sampling calorimeter detector with a large water target area in between of two electromagnetic calorimeters (Figure 3.7). The water target area consists of 26 tracking modules alternate with water modules. Between the tracker and water modules there is a thin 1.6 mm brass radiator. Two water bags are located vertically in each water

module. The two calorimeters at the front and the rear of the module consist of 7 tracking modules each with 4 mm thick lead radiators. This is because lead can stop particles much more quickly than brass, since lead's radiation length is shorter than brass'.

The dimension of each tracking P0D module is $220 \times 234 \times 3.9$ cm. P0D uses triangular scintillator bars, with 33.6 cm base and 17.25 cm height, in order to improve the particle's position resolution. The bars are oriented in alternate X-Y layers and 126 triangular bars are used along the X direction layer and 134 along the Y direction layer. The two perpendicular layers are separated with lead foil, which is used as a radiator. Each of the two layers is light-tightened from the inside with a rectangular PVC (3×3.85 cm) frame. The scintillation light is propagated using wave length shift fibers (WLS) and signal is read out using multi-pixel photon counters (MPPC) connected to a Trip-t Front-end Board (TFB) board.

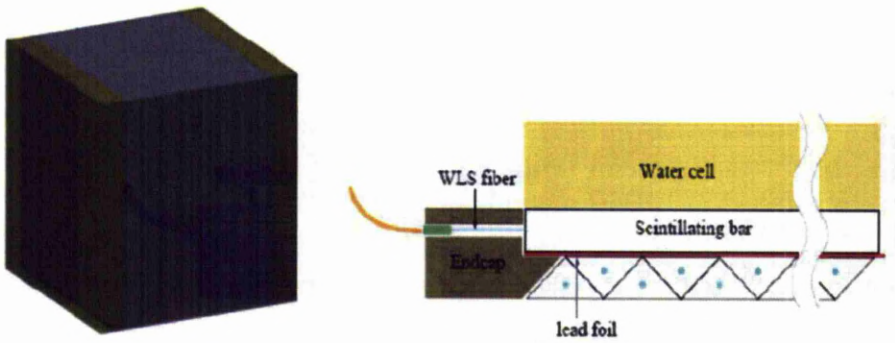

Figure 3.7: The P0D detector. On the left the water area in blue and on the right scintillator planes and water tanks.

3.4.2 The Fine Grain Detectors (FGD)

Like the POD, FGDs provide an active target for neutrino interactions, with the capability to measure short-range particles like recoil protons. Each FGD is followed by a time projection chamber, in order to characterize the charged particles produced from the neutrino interactions.

The first FGD is a scintillator detector, but the second one contains water as well. This way neutrino cross sections on carbon and water can be studied. The pure scintillator FGD has thirty X-Y layers each of 192 bars. Each layer consists of 192 bars along the horizontal direction glued to 192 bars in the vertical direction. A wavelength shifting fiber is passed through each scintillation bar. The scintillator bars, with dimensions $0.96 \times 0.96 \times$ 184.3 cm, are read from one end with an MPPC, while the other end is coated with reflective aluminium.

The second FGD has only 7 scintillation layers. It also has 6 water modules, 2.5 cm thick, in alternating position with the scintillation layers. Thus, the outermost of both FGDs consists of scintillation layers.

Both FGDs have the same external dimensions 230 $\times$ 240 $\times$ 36.5 cm and each contains approximately 1.1 tonnes of material. A difference between the FGD and the other scintillation detectors is that the MPPC is readout by the AFTER chip.

3.4.3 The Time Projection chamber (TPC)

The main purpose of the TPC is to measure the charged particle momentum using the curvature of a particle's track and also to measure the energy loss of charged particles, this being a powerful way of charged particle identification. The mean energy loss, in units of $MeVg^{-1}cm^2$, in the TPC is described by the Bethe-Bloch formula [57]

$$-\frac{dE}{dx} = 4\pi N_A r_e^2 m_e c^2 z^2 \frac{Z}{A}\frac{1}{\beta^2}\left(\frac{1}{2}ln\frac{2m_e c^2\beta^2\gamma^2 T_{max}}{I^2} - \beta^2 - \frac{\delta}{2}\right), \tag{3.2}$$

where N_A is the Avogadro number, r_e is the classical electron radius, m_e is the electron mass, z is the charge in units of e, Z is the atomic number and A is the atomic mass number of the absorber, β and γ are the relativistic parameters, I is the atom mean excitation energy,

T_{max} is the maximum kinetic energy of free electrons and δ is a correction factor due to density effects.

When a charged particle enters the TPC it will interact with the electrons of the gas molecules and lose energy by exchanging virtual photons. These photons will ionize the molecule if their energy is above the ionization potential. The primary electrons can produce secondary electrons by ionization or excitation of other molecules and if these electrons have enough energy they can create a separate track, called a δ-ray.

The propagation of a free electron or ion in a gaseous detector is also affected by drift and diffusion effects. Both drift and diffusion depend on the electric and magnetic fields present during the propagation of the electron or the ion. The drift effect is more important for electrons rather than ions. An ion, which is relatively heavy, does not scatter hard and loses more of its energy due to collisions. On the other hand, electrons scatter hard with the gas molecules and their direction can be randomly changed. The presence of the electric field can give some extra energy to the electron. The extra velocity picked up from the electron due to electric field is called the drift velocity. The diffusion effect describes how much the drift velocity of electron or ion cloud deviates from the average. The deviation is proportional to the square root of the ratio $\epsilon L/E$, where L is the distance traveled, E is the electric field and ϵ is the thermal energy.

The ND280 has 3 TPCs; one after the P0D, the second between the two FGDs and the third before the downstream ECal. The dimensions of each TPC is $1 \times 2.5 \times 2.5$ m filled with gas. The gas is mainly argon (95%) with small admixtures of CF_4 (3%) and iC_4H_{10} (2%) [63]. The reason for this mixture of the TPC gas is due to the avalanche created from the primary electrons. During the avalanche a lot of photons created can travel farther and create new avalanches, which could result in a higher charge deposit. Thus the presence of iC_4H_{10} can help to absorb these photons since this gas has a high photon absorption cross section. The CF_4 is important to increase the drift velocity in the drift region.

The ionization electrons are moving torwards the side walls of the TPC with the help of an internal 200 V/cm electric field. MicroMegas modules, each having an array of 6.8×9.7 mm pads with a 36×48 grid, then record the ionization electrons and the signal is

read out by the front-end electronics card (FEC). FEC uses a (72 ASIC) AFTER chip and each MicroMegas pad is connected to a channel. The AFTER chip allows for 511 samples, with 1-50 MHz frequency. When the chip is triggered, these samples are then fed to an external ADC.

The calibration of the TPCs is done using gas monitoring chambers and UV laser. The two gas monitor chambers are supplemented with two ^{90}Sr and a ^{55}Fe sources in order to study the gain and gas amplification. The first gas monitor chamber receives the TPC gas as the gas enters the TPC, and the second as the gas exits the TPC.

The UV laser emits light at 266 nm. An optical fiber is used to transfer the UV light to the TPC and is injected in the drift region. The UV light will eventually arrive on a central cathode and hit mounted aluminum strips and dots producing electrons via the photoelectric effect. These electrons drift towards the pad planes and eventually are detected by the MicroMegas modules producing a picture of the strips and dots. The laser calibration system is used to measure any distortions of the electric and magnetic fields, the drift velocity and to correct the gain due to temperature or pressure variations.

3.4.4 The DownStream Electromagnetic Calorimeter (DsECal)

The DsECal is located downstream the beam direction at the far end of the ND280 detector and after the last TPC. It has dimensions of $2 \times 2 \times 0.5$ m and it is built from 34 layers each containing 50 scintillator bars. Thin lead sheets, 1.75 mm thick, separate the layers. The DsEcal is a double ended read-out calorimeter. The construction and the characteristics of the DsECal follow very closely what is described for the BrECal modules in the next chapter. This module was the first installed in the basket and the only one of the ECal modules that has a leading role in the CC analysis for the Run-I (January-June 2010) dataset.

3.4.5 The Barrel Electromagnetic Calorimeter (BrECal)

The BrECal modules are very similar, but much larger than the DsECal module. In total, 6 BrECal modules are surrounding the tracker (FGD+TPC) region. Half the layers of the BrECal are single ended read-out, while the other half are double ended read-out. The next chapter gives a full description of the construction of these modules and more details about their dimensions and commission in the experiment.

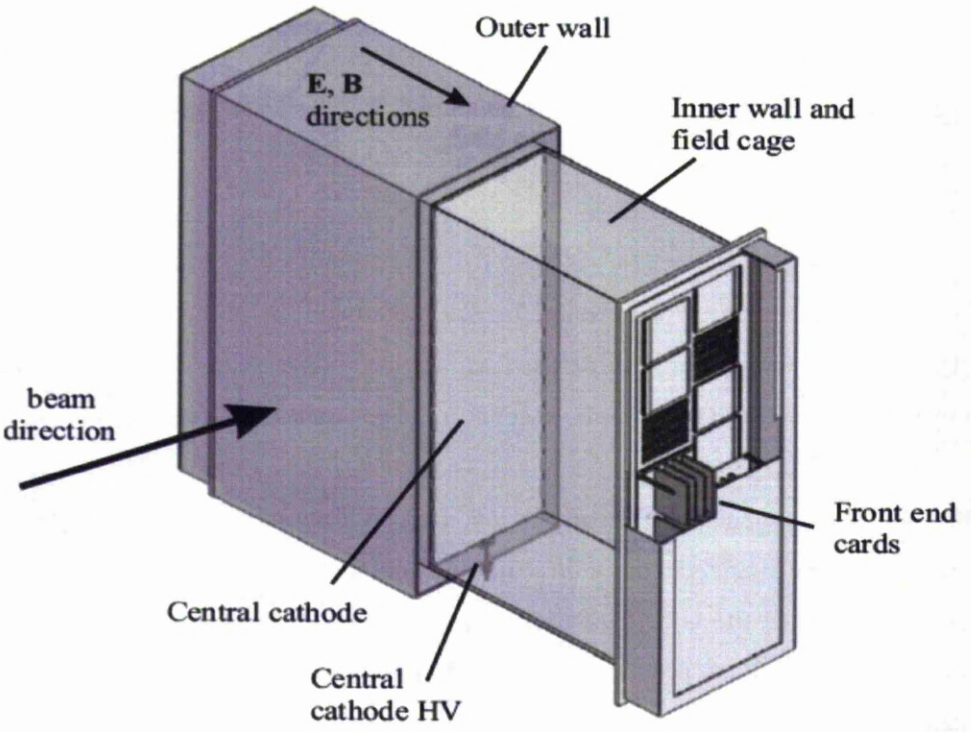

Figure 3.8: The TPC detector. From [64].

3.4.6 The P0D Electromagnetic Calorimeter (P0DECal)

P0DEcal modules, six in total and located inside of the iron yoke of the magnet and surrounding the P0D detector, are a miniature of the barrel and downstream ECals; see the sections describing these calorimeters for more details. The side modules have dimensions $2.6 \times 2.3 \times 0.5$ m and the top/bottom modules have dimensions $1.4 \times 2.3 \times 0.5$ m. All the modules have 6 scintillation layers, alternating with five 4 mm thickness lead layers. The side module layers consist of 58 scintillation bars while the top/bottom layers consist of 35 scintillation bars. The P0DECal modules are read out from one end only, while the other end is mirrored. The small number of layers of each module does not allow for a full π^0 reconstruction; instead the P0DECal aims to tag photons created with large opening angles in the P0D.

3.4.7 The Side Muon Range Detector (SMRD)

SMRD is scintillator detector located inside the magnet yoke. The magnet yoke was donated from CERN and it was previously used in the UA1/NOMAD experiment. The physics role of SMRD is to measure muon tracks produced from neutrino interactions in the tracker region, especially those tracks that are not very well reconstructed in the tracker. Also, it is used as a veto detector either for neutrino interactions from outside the detector or for cosmic muons. Detection of cosmic muons from the SMRD is also useful for calibration triggering. This is due to the fact that neutrino interactions occur only when a beam spill arrives in the detector. In the meantime between two different spills we are able to do other calibration measurements. If a signal is detected at the edges of the SMRD, top to bottom or left to right, indicating a passing muon, then all the basket detectors can verify that indeed they perform nicely. As the SMRD is located inside the magnet yoke, its shape is also controlled from the yoke design. SMRD uses the slits inside the yoke. The yoke is divided in two parts, each consists of 8 C-shape (called the Cs) sections, see Figure 3.9. Each scintillator unit consists of a plastic scintillator slab $870 \times 170 \times 0.7\times$ mm. The signal is read out using WLS fibers and MPPCs. In total 440 SMRD scintillation units were installed during the installation period in 2009.

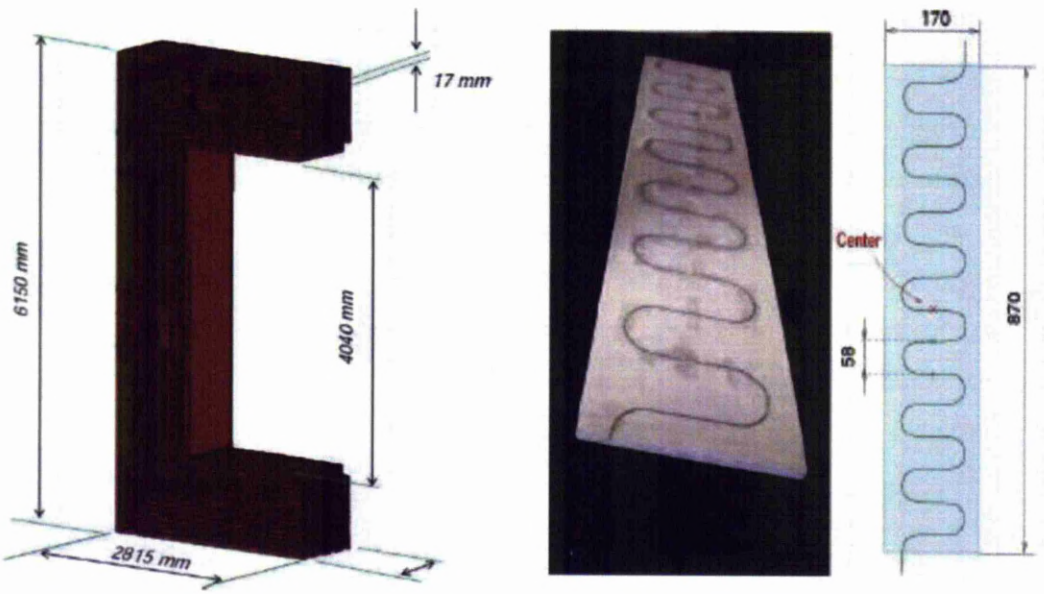

Figure 3.9: A C magnet yoke (left) and a scintillator unit (right) for the SMRD.

Chapter 4

The construction of the Barrel Electromagnetic Calorimeter

This chapter describes the construction of the Barrel Electromagnetic Calorimeter (BrECal) modules. The basic concepts in designing an electromagnetic calorimeter are described at the beginning of this chapter. This can also be considered as a preliminary introduction to calorimetry. Then the details of constructing the BrECal modules are described. A basic description of the devices and electronics used is also provided. Finally, some details of the installation of all the ECal modules in the near detector pit are given.

4.1 Basic Concepts Designing an EM Calorimeter

The basic principle of calorimetry is the absorption of a particle's energy in some material and then the measurement of its deposited energy. Photons, electrons and hadrons can interact with matter producing secondary particles and forming a shower which leads to a very efficient energy deposition. At relatively high energies ($>$ 10 MeV), photons lose energy mostly through electron-positron pair production and electrons mostly through bremsstrahlung. At lower energies, other effects like Compton scattering and photoelectric effect for photons, and ionization or excitation for electrons, are also important. On the other hand, muons lose energy mostly by ionization, thus they deposit only a minimal amount of their energy. We usually call these particles minimum ionizing particles (MIP).

The energy loss for electrons through bremsstrahlung is given by the simplified formula

$$-\frac{dE}{dx} = \frac{E}{X_0}, \tag{4.1}$$

with X_0 the radiation length. A very simplified model for the shower formation can be considered assuming that each electron, with energy higher than the critical energy, travels one X_0 and then gives up half of its energy to a bremsstrahlung photon. Analogously, each photon with energy higher than the critical energy travels one X_0 and then undergoes pair production equally splitting its energy to the electron-positron pair. Electrons with energy lower than the critical energy cease to radiate and lose energy through ionization. Defining the distance of a particle traveled, normalized in radiation lengths, $t = x/X_0$, the total number of particles after t is

$$N(t) = 2^t. \tag{4.2}$$

The shower energy of a particle at depth t is

$$E(t) = E_0/N(t) = E_0/2^t, \tag{4.3}$$

with E_0 the initial energy of the particle. As long as $E_0/N(t)$ is larger than the critical energy the shower development continues. The maximum depth t_{max} is reached when

$$E(t) = E_c = E_0/2^{t_{max}}, \tag{4.4}$$

with E_c the critical energy. Thus the maximum depth is then

$$t_{max} = \frac{\ln(E_0/E_c)}{\ln 2} \propto \ln(E_0). \tag{4.5}$$

The number of particles at maximum depth, t_{max}, is

$$N_{max} = \frac{E_0}{E_c}, \tag{4.6}$$

while the total number of charge particles (electrons and positrons) is $\frac{2}{3}N_{max}$.

After the energy of an electron drops below the critical energy, the particle will stop in one X_0. The above description for the shower development is very simple; in reality the shower development is much more complicated. However, even this simple model can qualitatively describe some of the main characteristics of shower development. The longitudinal dimensions of the calorimeter should be considered since the maximum development of the shower happens at t_{max}, while t_{max} is increasing logarithmically with the incident particle energy E_0. Also there is a linear connection between E_0 and the number of particles in the shower. Energy leakage occurs due to soft photons and also due to edge effects. Assuming Poisson statistics, the energy resolution of the calorimeter can be expressed as

$$\frac{\sigma(E)}{E} = \frac{1}{(2/3)N_{max}} \propto \frac{1}{\sqrt{E}}. \tag{4.7}$$

Beyond this simplified model there are more details that need to be considered, like the unequal energy sharing to electron-positron pair or to Bremsstrahlung photon, the difference between showers induced by photons or electrons ($\lambda_{pair} = \frac{9}{7}X_0$) and consider fluctuations since the number of electrons is not governed by Poisson statistics. Also the t_{max} value needs to be corrected by taking into account other secondary effects like electron scattering.

One other thing that is particularly important is the lateral spread of the shower. Multiple scattering, emission angle of Bremsstrahlung photons, the opening angle of the electron-positron pair can contribute to widening the shower. In general the lateral width scales with a parameter called the Moliere radius ρ_μ

$$\rho_\mu = X_0 \frac{E_s}{E_c}(g/cm^2), \tag{4.8}$$

with E_s=21 MeV. 95% of the shower is contained in a cylinder with diameter $2\rho_\mu$ independently from the particle's incident energy.

There are two main types of calorimeters. Homogeneous calorimeters use the same element for the collection of charge or light and for the shower development. These calorimeters can combine short attenuation length with large light output, resulting in a high energy resolution. The second type, and the one used at near detector ND280, is known as as

sampling calorimeters since only a part of the energy is sampled in the active medium. A sampling calorimeter consists of two different elements in a sandwich geometry. The signal is collected by layers of active materials (detectors) and the shower develops through layers of passive material (absorber). Although the energy resolution is worse for a sampling calorimeter, the segmentation allows the measurement of spatial coordinates which means much better position resolution than the homogeneous calorimeter. While the homogeneous calorimeter is used exclusively for electromagnetic calorimetry, the sampling concept can also be extended to a hadronic calorimeter as well. The number of particles for a sampling calorimeter is

$$N_{sample} \propto \frac{\frac{2}{3}N_{max}}{d[X_0]}, \tag{4.9}$$

with d the distance between the active planes. The sampling resolution is

$$\frac{\sigma_{sample}}{E} \propto \frac{1}{\sqrt{N_{sample}}} \propto \frac{\sqrt{d}}{\sqrt{E}}. \tag{4.10}$$

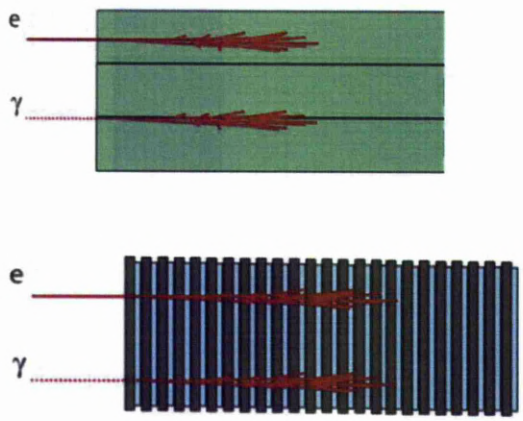

Figure 4.1: Example of a homogeneous calorimeter (top) and a sampling calorimeter (bottom)

4.2 Construction of the Barrel ECal modules

In total six Barrel ECal (BrECal) modules surround the tracker region in ND280. Two modules at the sides of the tracker and four, relatively smaller, modules located on the top and bottom of the tracker. All modules are constructed from 31 scintillation layers. The dimensions of the top and bottom modules are $4.2 \times 1.5 \times 0.5$ m, while the side modules are $4.2 \times 2.3 \times 0.5$ m. The construction of the first two modules started in July of 2009, with a parallel construction at Liverpool University and Daresbury Laboratory. The construction of all six modules took approximately one year; the last BrECal module was shipped to Japan in September of 2010.

The construction of a module starts by building the orthogonal metallic base and assembling the scanner (Figure 4.2). The scanner is programmed to pick up, using a robotic arm from a special radiation safety case, the radioactive source and move it a few mm distance from the layer surface. This is repeated for a lot of different positions along each scintillation bar. A full layer scan could take up to several hours to finish.

Then the bottom module base and the aluminum frame (called the bulkhead) are put together (Figure 4.3). The base of the module is a large aluminum frame surrounding a carbon fiber component. The carbon fiber component has a normal strength component and a high strength component getting wider near the edge. The properties of the carbon fiber panels are summarized on Table 4.1.

The height of a typical bulkhead is 40 cm and the width is 2.5 cm. The length varies according to the module and the side. The holes on the bulkhead are located so as to match each scintillator bar and allow the WLS fiber to pass through. The horizontal distance between each hole is 4 cm and the vertical distance is 2.5 cm. Each photosensor is held securely in place with a screw.

After the bulkhead is built, we continue with the procedure to put in and scan all the 31 layers. Two different types of layers are used. Long bar layers have 38 (57) scintillation bars for the top/bottom (side) modules. Short bar layers have 96 scintillation bars for all modules. The scintillation bars made from polysterine were constructed at Fermilab and shipped to the University of Sheffield. The colleagues from the University of Sheffield cut

Module	Carbon Fiber Panel Properties
Top BrECal	Dimensions: 3899 × 1551.5 × 40 mm Normal Strength Panel Thickness: 36 mm (28 mm at the edges) Normal Strength Panel Skins: 2 × 2 ply Carbon Fiber 650g E720-02 Normal Strength Panel Core: HEXWEB HRH - 10-3.2-48 Normal Strength Panel Adhesive Film: DF72 300g Hard Strength Panel Thickness: 2 mm (6 mm at the edges) Hard Strength Panel Skins: 10 ply Carbon Fiber 200g E720-02 Hard Strength Panel Core: HEXWEB HRH - 10-3.2-144 Hard Strength Panel Adhesive Film: DF72 300g
Bottom BrECal	Dimensions: 3899 × 1551.5 × 40 mm Normal Strength Panel Thickness: 37.6 mm (28 mm at the edges) Normal Strength Panel Skins: 2 × 2 ply Carbon Fiber 650g E720-02 Normal Strength Panel Core: HEXWEB HRH - 10-3.2-48 Normal Strength Panel Adhesive Film: DF72 300g Hard Strength Panel Thickness: 1.2 mm (6 mm at the edges) Hard Strength Panel Skins: 10 ply Carbon Fiber 200g E720-02 Hard Strength Panel Core: HEXWEB HRH - 10-3.2-144 Hard Strength Panel Adhesive Film: DF72 300g
Side BrECal	Dimensions: 3899 × 2287.5 × 50 mm Normal Strength Panel Thickness: 46 mm (34 mm at the edges) Normal Strength Panel Skins: 2 × 2 ply Carbon Fiber 650g E720-02 Normal Strength Panel Core: HEXWEB HRH - 10-3.2-48 Normal Strength Panel Adhesive Film: DF72 300g Hard Strength Panel Thickness: 2 mm (8 mm at the edges) Hard Strength Panel Skins: 10 ply Carbon Fiber 200g E720-02 Hard Strength Panel Core: HEXWEB HRH - 10-3.2-144 Hard Strength Panel Adhesive Film: DF72 300g

Table 4.1: The carbon fiber panel properties for the Barrel-Ecal modules. The panel core of the HEXWEB HRH - 10-X-Y should be read as X mm of honeycomb at Y kg/m^2.

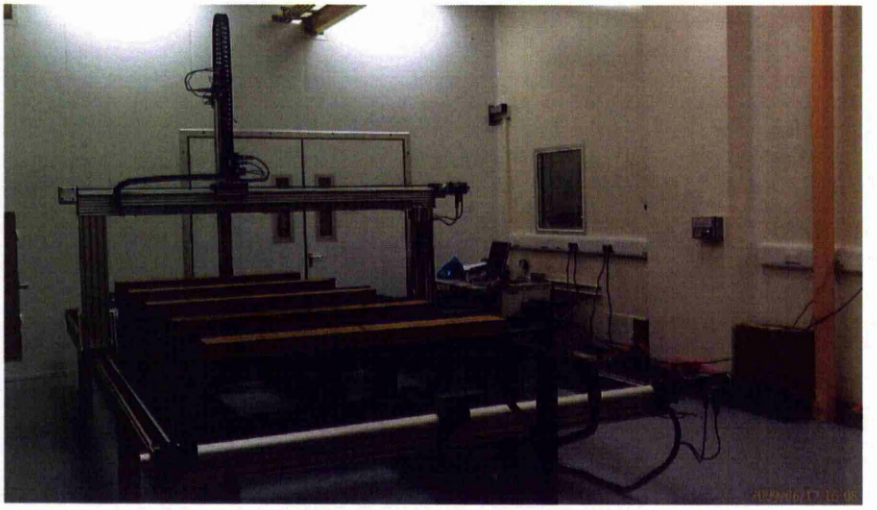

Figure 4.2: Construction of the metallic base and the scanner for the BrECal construction.

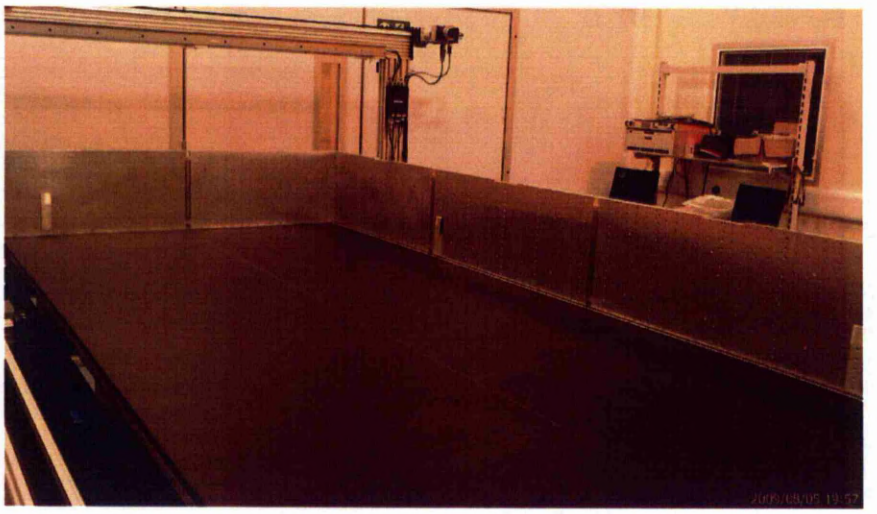

Figure 4.3: Assembly of the module base and the bulkhead

the scintillation bars according to the size of the module and distributed them to Lancaster University, to construct the top and bottom module layers, and to Daresbury Laboratory to build the side and top/bottom module layers.

The scintillation bars for the bottom and top modules have dimensions $380 \times 4 \times 1$ cm for the long bar layers and $150 \times 4 \times 1$ cm for the short bar layers. For the side modules, only the dimensions of the short bars are different, $230 \times 4 \times 1$cm. All scintillation bars have a tiny elliptical 1×2 mm hole in the center from where the WLS fiber is passed through. The white reflecting coating of the scintillation bar is a blend of polystyrene and TiO_2. Two dopants are also added in the polystyrene. The primary dopant is 2,5-diphenyloxazole (or PPO). This is an organic scintillator and is a 1% dopant by weight. It can absorb the ionizing energy of a passing particle and then excites an electron to a high energy state. The de-excitation of the electron produces light which becomes the signal for the detector. The secondary dopant (0.03% by weight) is 1,4-bis(5-phenyloxazol-2-yl) benzene or POPOP. This dopant is a wavelength-shifting scintillator with an absorption cut off at 400 nm and an emission maximum at 420 nm.

A layer consists of an aluminum frame surrounding the scintillation bars sandwiched by a 1.75 mm lead layer with a 2% Sb alloy. Once the scintillation bars are placed inside the aluminium frame, an adhesive is applied along the aluminium frame and across the top of the bar array. The thin lead layer is then dropped in using a vacuum lifter, and after waiting for a few hours for the adhesive to cure, the layer is ready to be used for installation in a calorimeter module.

All the BrECal modules have 16 short bar layers and 15 long bar layers and the layers are stacked in an alternate XY orientation. The Kuraray Y-11(200)M fiber with 1 mm diameter is used. The attenuation length for this type of fiber is > 3.5 m. To check for any damaged WLS fibers, each one is scanned with a Cs-137 source and the attenuation of each fiber is measured. 20 (10) points are scanned for the long (short) bar layers.

The signal read out is done using Multi Pixel Photon Counters (MPPC). The MPPC is an array of avalanche photon-diodes (APD) operated in Geiger mode. High gain can be achieved with a reverse operation voltage, V_{op}, above the APD's breakdown voltage V_{br}. When a photon arrives at the Geiger-mode APD, a carrier is released and accelerated by

the electric field in the depletion region. Each pixel will contribute an amount of charge to the total signal

$$Q = C(V_{op} - V_{br}) \tag{4.11}$$

where C is the capacitance of the pixel.

Typical breakdown voltage is $\sim 70V$ and usually the operation voltage is $\sim 1V$ above the breakdown voltage making the usage of MPPC quite easy. Thus, a gain $\sim 10^6$ can be achieved. A resistor R is integrated to each pixel so that it can be recovered with a time constant RC $\sim$ 13ns [65]. Each pixel is triggered independently and finally all pulses from each pixel are summed resulting in a large pulse. The number of photons is then known by measuring the height or the charge of the large pulse.

The MPPC model that ND280 is using is the Hamamatsu S10362-13-050C which is a square device with side length 1.3 mm and 667 pixels in total [66, 67] shown in Figure 4.4. MPPC is a compact and relatively low cost device. High photon detection efficiency, insensitivity to magnetic field, high gain and low multiplication noise are the main advantages of an MPPC. The main disadvantage of the MPPC is its sensitivity to temperature changes.

Cross-talk and dark current are two important sources of MPPC noise and must be taken into account. Cross-talk happens when a discharging pixel can leak to a neighbor one causing this pixel to discharge as well. Dark current is a more important source of MPPC noise since, due to thermal excitation, a pixel may fire without an incident photon. At the single photo-electron level the dark current is in the range of 300-800 kHz/mm^2. At the double photo-electron level the dark current is by an order of magnitude lower, but it is also of a significant percentage of noise hits. Dark counts at the 3 or 4 photo-electron levels can also occur but in lower rate. Since the dark current is temperature dependent and its stability is of vital importance, good temperature control is required and especially during the scanning operation.

The signal from the MPPCs is sent to the the Trip-t Front-end Board (TFB). The Trip-t chip was first designed at Fermilab for the D0 experiment [69]. Each TFB has 4 Trip-t chips mounted. Trip-t can integrate and store signal in a 48 channel deep analog pipeline and in total 32 channels are read out. The signal from the photosensor is capacitively divided into

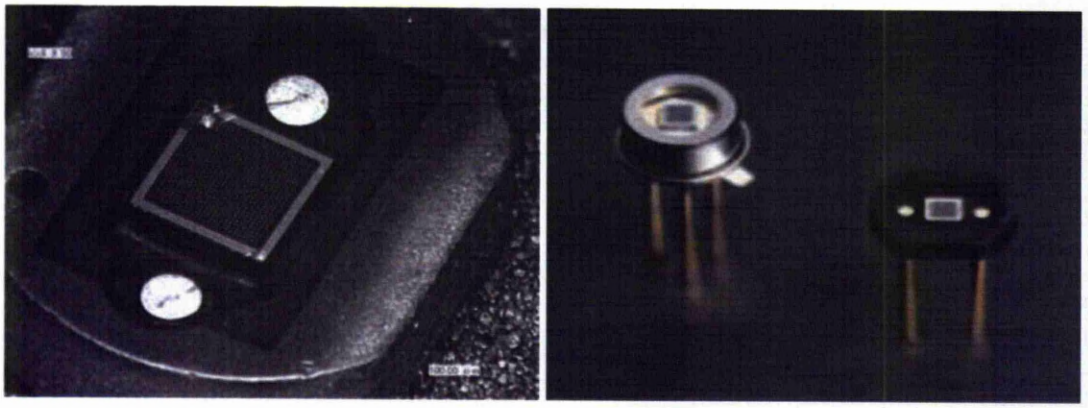

Figure 4.4: The MPPC device developed for ND280. From [67, 68].

two groups forming the 16 low and the 16 high gain channels. The high gain channels have their own discriminator and are used for a precision time-stamp. The high/low gain ratio is 10.

Each TFB can read up to 64 MPPCs. Each MPPC and the TFB board are connected with a short miniature coaxial cable. The 4 Trip-t chips on the TFB board are controlled by another chip, the field programmable gate array (FPGA). The MPPCs are connected to the TFB board with a thin coaxial cable. The two TFBs are also connected to the RMM. Source data are collected through the coordinated operation of two systems. One is the scanner machine controlling the positions to scan on the layer surface, and, the other is the DAQ machine selecting the data from the MPPCs.

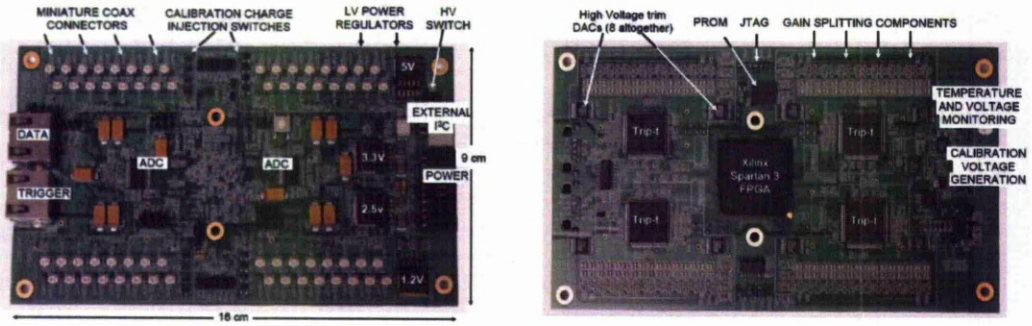

Figure 4.5: The top (left) and bottom (right) view of a TFB. From [69].

Long bar layers are read out from both ends while the short bar layers are read out from the one end only since the attenuation length of the Y11 fiber is > 350 cm, thus this effect is expected to be minimal for the short bar layers. To maximize the light collection the other end of the short bar layers is aluminized in order to reflect the secondary light emitted. On the other hand, fiber attenuation may be an important effect for long bar layers so signal readout from both ends is necessary.

After the first layer is installed, the Light Injection (LI) system, a strip of LEDs and focusing lenses, is also installed with responsibility from colleagues of the University of Sheffield. The LI is installed between the module base and the first layer, and is very useful for checking the integrity of each of the readout channels and also for time calibration and gain monitoring. The operation of the LI system must also be in a good shape providing uniform pulses and it must be free from optical or electromagnetic noise (Figure 4.6).

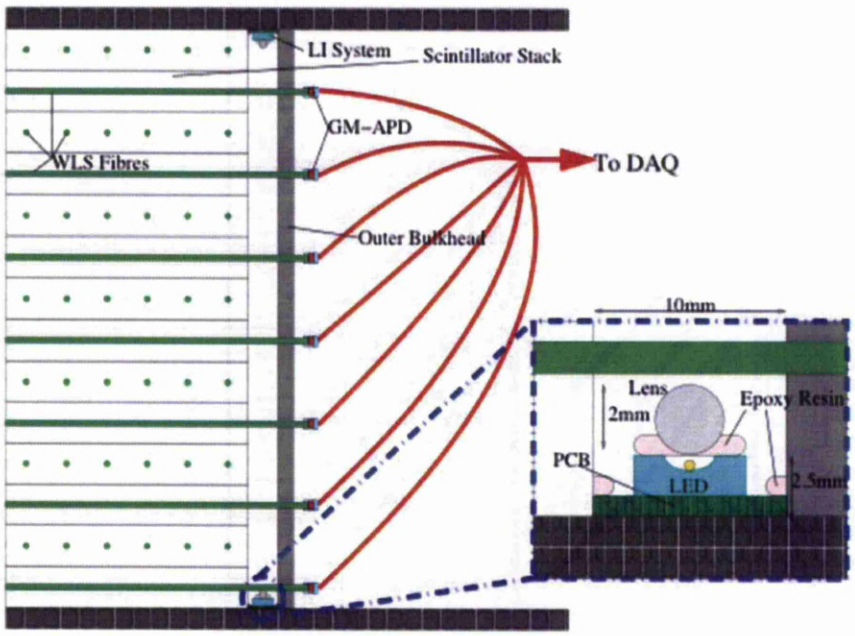

Figure 4.6: Installation of the LI system in a calorimeter module.

A vacuum lifter is used to install each layer in the module, and the layer is carefully fastened to the one below. Then a WLS fiber is passed through each scintillation bar. The WLS fibers come with three different lengths, in order to match the length of the scintilla-

tion bars. At the end of each fiber we need to glue a plastic ferrule, in order to connect it with the MPPC. For the short bar layers, the ferrule is already glued on the fiber, however, for the long bar layers we have to glue both ends on the ferrule. The glue used is BC-600. The refractive index of BC-600 Optical Cement is close to that of plastic scintillators. Thus, it can be used to optically bond the plastic scintillators to optical windows or acrylic light guides. It is a two part glue and approximately 100 gr from the resin has to be mixed with approximately 28 gr of the hardener. At room temperature the resin can take up to fpur hours to set and 24 hours to harden.

After all the WLS fibers are passed through the scintillation bars, the glue is gently applied to the edges of the WLS fiber. Then, from both ends, the ferrules are slowly inserted onto the fiber. To keep the ferrule in position, until the resin is set, special plastic caps with a spring embedded are used. The caps are temporarily screwed into the bulkhead and removed after the resin is set. It is important that the whole procedure takes place simultaneously at both ends of the fiber, as to make sure the springs won't bend the fiber significantly and potentially cause damage.

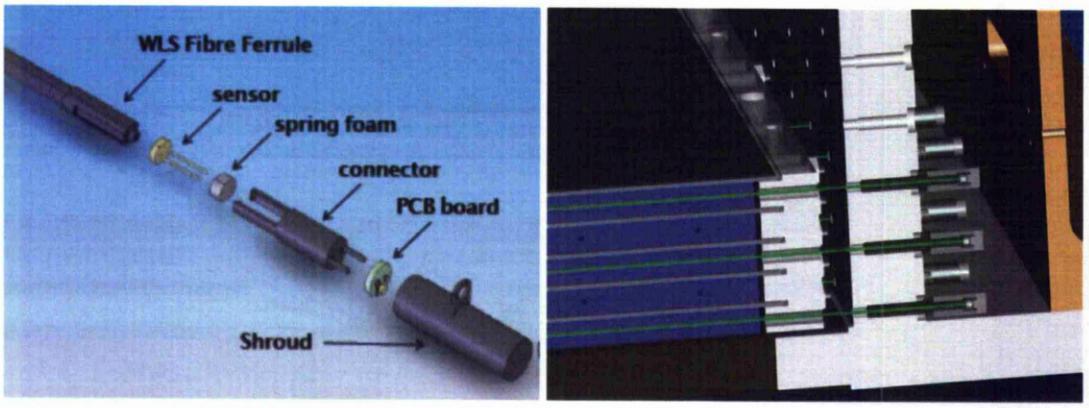

Figure 4.7: A cartoon showing the components of the plastic ferrule and the MPPC. The shroud is used for the long fibers in order to keep them in position until the resin is set.

As already mentioned, when the construction of a single layer is completed, we proceed with the scanning using a collimated 115 Mbq Cs-137 source. The purpose of scanning each layer is not to measure any physical quantities, but simply to test the fiber attenuation, in respect to the distance between the point scanned and the sensor. This is because the

mean energy of the photons coming from the Cs-137 source is 662 keV, much less than the energy regime at T2K. The photons from the Cs-137 source will eventually produce scintillation light which is selected from the optic fiber and the green light re-emitted is transmitted by internal reflection to the photosensor. In the case that a fiber is found to be damaged then it is replaced by a new one and it is scanned again.

During the scanning time we have to make sure that no external light reaches the module, in order to avoid the saturation of the MPPCs. For this reason, during the scanning period, the module is light tightened with a special black industrial coverage.

Figure 4.8: Scanner in action. The special case where the Cs radioactive source is located is also visible on the right.

To study the fiber attenuation each point was scanned with 2000 events for the first four modules. For the remaining two modules, after performing a lot of tests and using the experience gained from the first four modules construction, the number of scanned events was reduced to 1000. At the same time it was realized that the scanning of two layers was possible, without too much loss of attenuation profile, since we could still see a large

data to noise ratio. With these two modifications the construction and scanning time was eventually reduced by a factor of two.

The events are recorded in the MIDAS format [70, 71], a data acquisition format suitable for storing raw data from the readout electronics. MIDAS format has an internal mechanism to save raw data in the ROOT data analysis format [72]. Thus, the readout from a single MPPC over the 23 integration cycles for the low and high gain ADC and TDC is given in a plain ROOT format. For the fiber attenuation study only the high gain ADC values are used. The high gain raw ADC spectrum from a single scanning point is shown in Figure 4.9. The absolute gain can be computed by measuring the channel difference between two neighbor peaks

$$\text{gain}_{Abs} = (\text{Channel Difference} \times \text{ADC}_{\text{resolution}})/e, \tag{4.12}$$

where e is the elementary charge, $e = 1.6 \times 10^{-19} C$ and the ADC resolution is in units Coulomb/channel. A relative gain can be defined by the channel difference between the neighbor peaks. For the rest the relative gain will be used and will simply be referred to as gain.

From Figure 4.9 the mean value of a peak is computed by fitting a Gaussian function. The gain is then calculated from the mean value difference either from the first and second peak or from the first peak and the pedestal. The gain is also used to calibrate the distribution by shifting the raw spectrum with the quantity

$$\text{C} = (\text{ADC-Pedestal Mean})/\text{gain}, \tag{4.13}$$

so that the pedestal mean corresponds now to 0, the first photoelectron peak to 1, and so on, as shown in Figure(4.10).

The calibration is essential basically for two reasons. The first has to do with the temperature dependence of the MPPCs, as the value of the gain computed at different times can vary. The second reason is because of the way we are studying the fiber attenuation by comparing the ADC distributions before and after the scanning is taking place Figure 4.11.

From these two distributions the ratio of signal to background after the sixth photoelectron peak is calculated. The same procedure is repeated for all the scanning points along a bar, and finally the attenuation profile plot is generated as a function of the signal to background ratio with respect to the distance to the photosensor.

The attenuation profile is then fitted by the sum of two exponential functions

$$P(d) = \alpha e^{\beta + d/\lambda_{long}} + \gamma e^{\beta + d/\lambda_{short}}, \tag{4.14}$$

where d is the distance to the photosensor, λ_{long} is the long attenuation length, λ_{short} is the short attenuation length, β is a falling factor same for both exponentials and α, γ are shape parameters. The short attenuation length characterizes the wavelength shift and the long attenuation length the amount of light scattered. Figure 4.12 shows typical attenuation profiles for long bar layers. The error bar on the attenuation profile plots is $\pm\sqrt{N}$. Edge effects are also visible on these plots. The study for the fiber attenuation is basically done only for the long bar fibers. Because of the length of the short bar fibers, the double exponential function, equation 4.14, could not describe very well the short and long attenuation. Thus, for short bar fibers, we produce the attenuation profile similar to those of Figure 4.12, but only take care that the signal-to-background ratio is relatively increasing as long as the scanning position is moving closer to the sensor.

One other thing that we have to take care during the construction, especially for the bigger side modules, is a possible slight bending of the module either in the center or at the sides. Thus, after the first few layers are installed, using a micrometer we measure the distance difference between the center and the edges of the module. This difference has to be at the order of a few mm.

After all the 31 layers are installed and tested, all the "naked" fibers glued on the ferrule must be clipped to a MPPC inserted into a special plastic cylindrical cap. As seen in Figure 4.13 special screws are needed to clip the plastic cap on the first layer's MPPCs. Each MPPC is bar coded and this unique identification is important in case any problems appear during the full module operation in Japan. Each MPPC has also to be connected to a TFB channel. It is also important to connect each MPPC to a mapped position on the TFB.

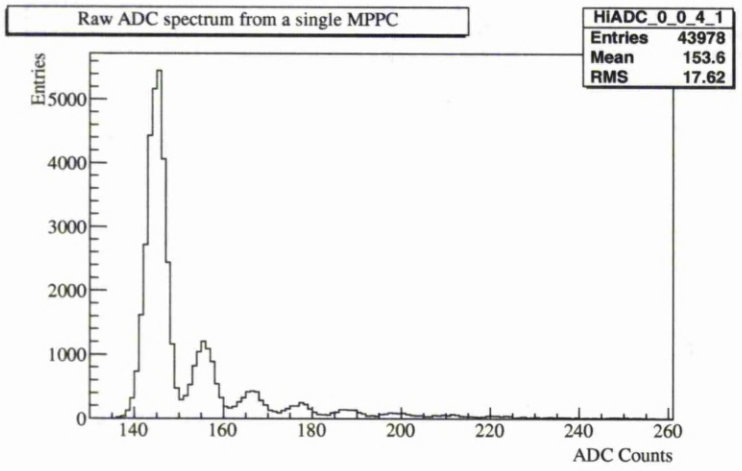

Figure 4.9: Raw ADC counts from a single MPPC.

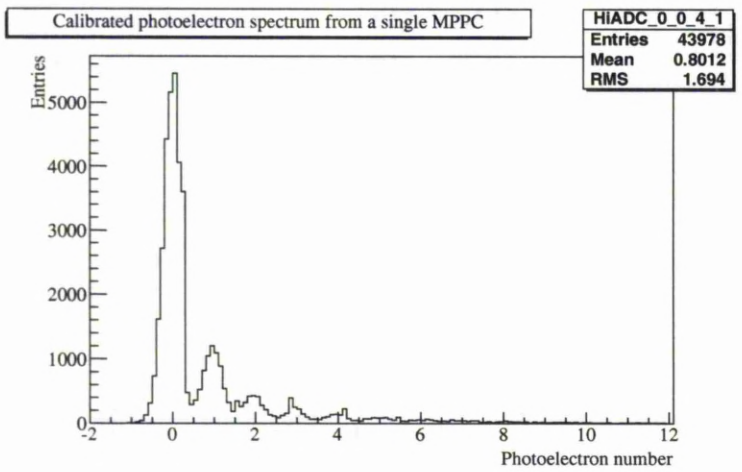

Figure 4.10: Calibrated spectrum, using equation 4.13 from a single MPPC.

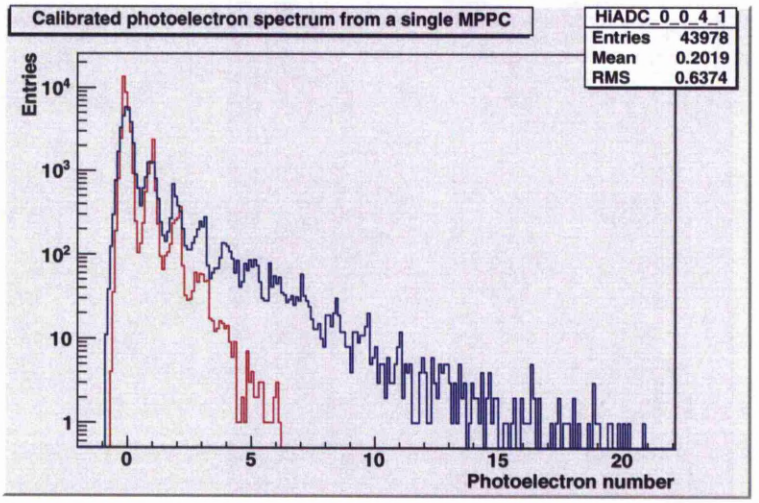

Figure 4.11: The calibrated signal (Blue) and background (Red).

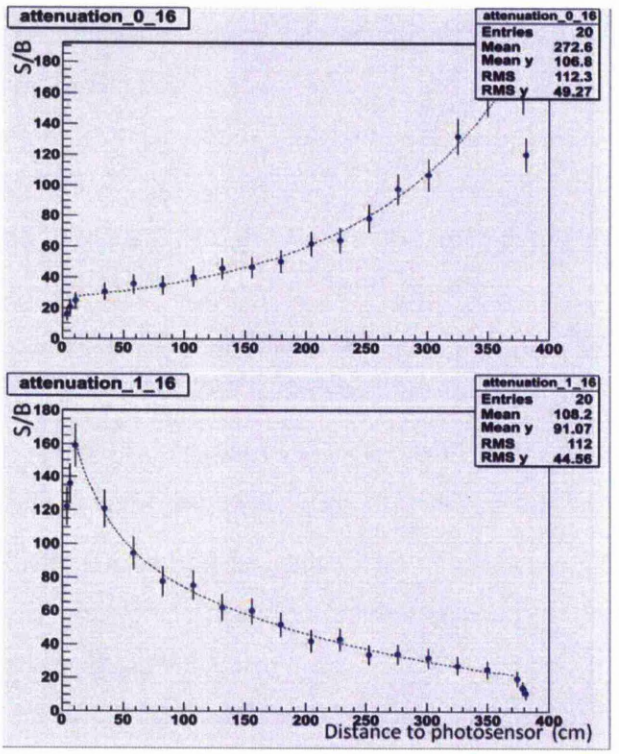

Figure 4.12: Typical fiber attenuation curves for long bar layers. The attenuation is read from both ends of the fiber and is fit using equation 4.14. The edge effects are visible at the first and last points of the attenuation curves.

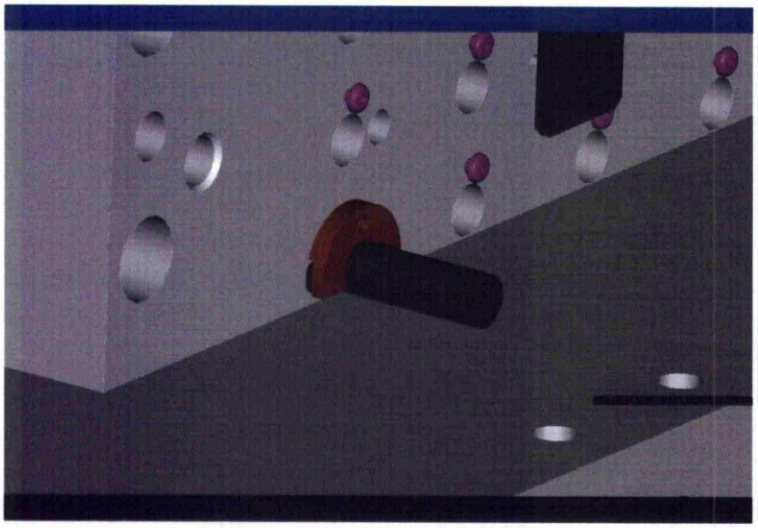

Figure 4.13: Clipping the plastic cap with the MPPC attached on the first layer's ferrule.

The TFBs are attached on a aluminum cooling plate. In total 44 TFBs are needed for the top/bottom modules and 52 for the side modules. After all the MPPCs are connected on the TFBs and the cooling plates are in position on the module, a series of voltage calibration tests take place, in order to make sure that everything is functioning appropriately, to check that everything is wired correctly, and also to do a last check for any damaged MPPC or TFB.

The TFBs are powered by copper bars running around the center of the module, and each metallic bar is assigned to a specific low voltage value. Also, the MPPC's high voltage is provided on a different line. Each TFB must also be connected to the RMM using a category-5 ethernet cable. Each ethernet cable must be cut to the appropriate length.

Water cooling pipes are attached along the perimeter of the cooling plates. After the pipes are welded the system is pressure tested. An LI system has to be installed on the top of the module and before the lid is fixed. Finally, the patch panel is affixed and all ethernet cables are threaded through. A black backing plate is fixed on the open side of the module, in order to minimize any light leakage.

The module is then ready for transport to Japan, and installed in J-PARC. A private company was hired for the transportation and the module is fixed and sealed in a special

box, assuring a safe transportation.

The construction of the barrel ECal modules was a strong collaboration from many universities across the country. From the University of Liverpool and the Daresbury Laboratory, which had the general responsibility for the construction, a lot of academic and research staff, a lot of PhD and Masters students and engineers methodically worked, within short time limits, to build, test and transport the modules to the J-PARC site in Japan. During this time, a lot of significant effects and improvements were studied as topics for Masters thesis programs, taking care of the edge effects, statistical methods to separate healthy from damaged optic fibers, improve the optic fiber attenuation studying different functions to fit the attenuation profile plots and study the MPPC behavior under temperature changes.

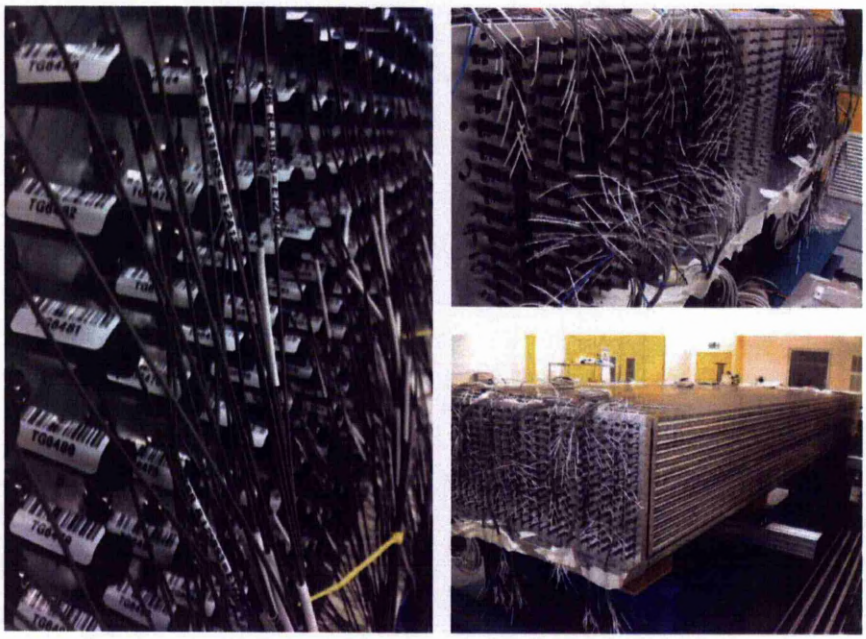

Figure 4.14: Clipping MPPC to the fibers.

4.2.1 Details of the calorimeter construction

The details of the ECal construction near the edges and the active volume are shown in Figures 4.17-4.19. These include the active volume distance of the ECal from the bulkhead and cooling plate. All the ECal modules are shown here for comparison. Finally, Figures 4.20-4.22 show the installation details and the distances between the calorimeters

Figure 4.15: MPPCs connected on the TFBs. The TFBs are attached on the cooling plates. The bottom pictures are showing the module after all the MPPCs are connected and the cooling plates put in place.

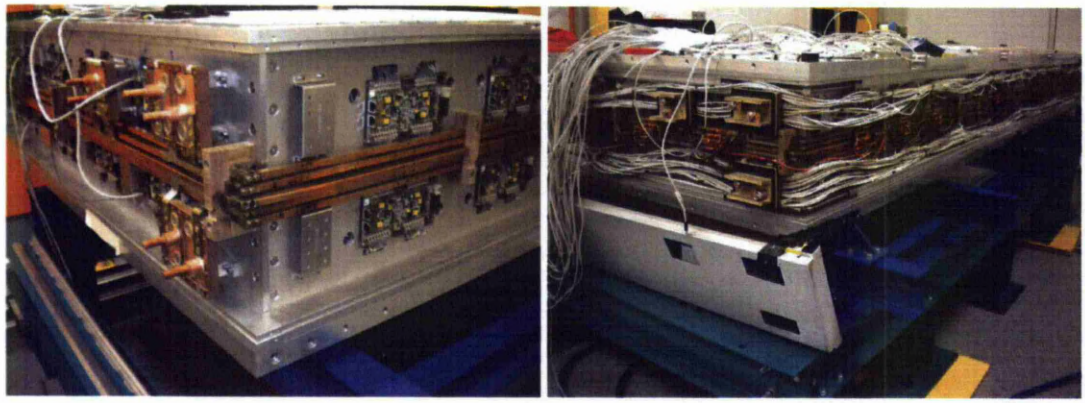

Figure 4.16: Metallic bars supplied the TFB voltage, cooling pipes and ethernet cables attached on the module

inside the basket. All units are in mm.

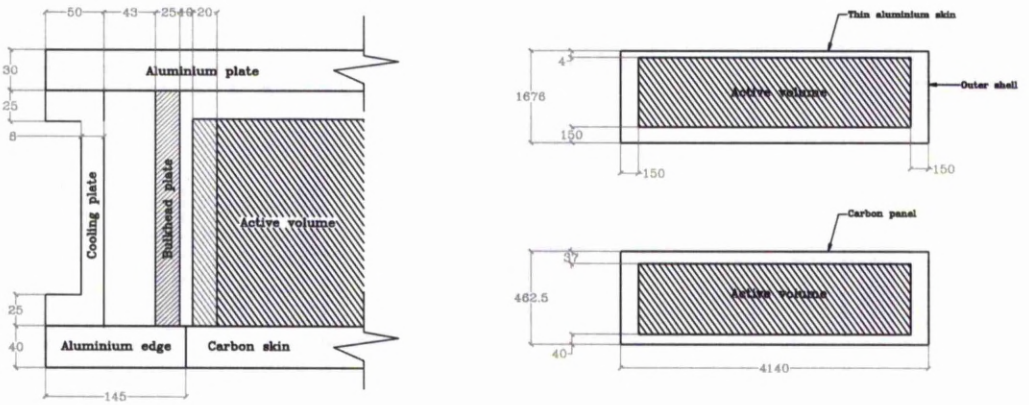

Figure 4.17: The active volume and details near the edge of the top/bottom BrEcal.

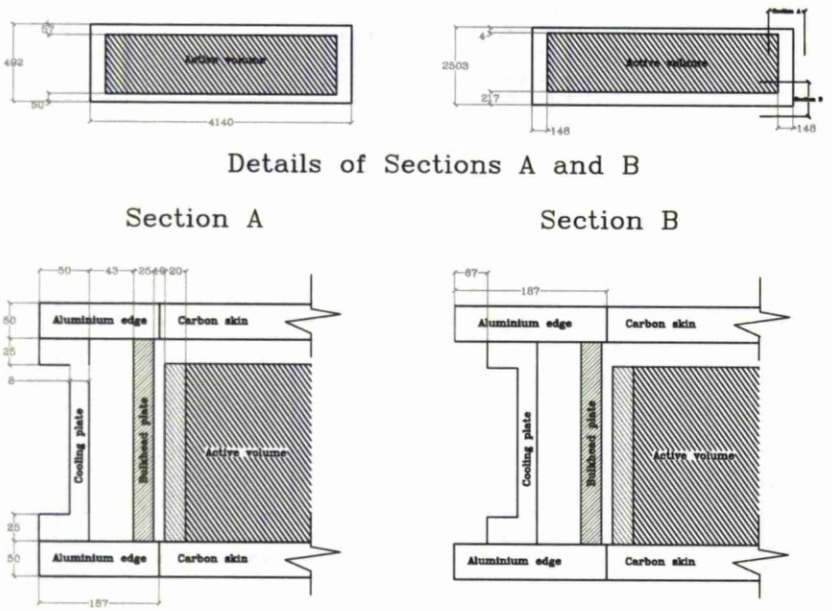

Figure 4.18: The active volume and details near the edge of the side BrEcal.

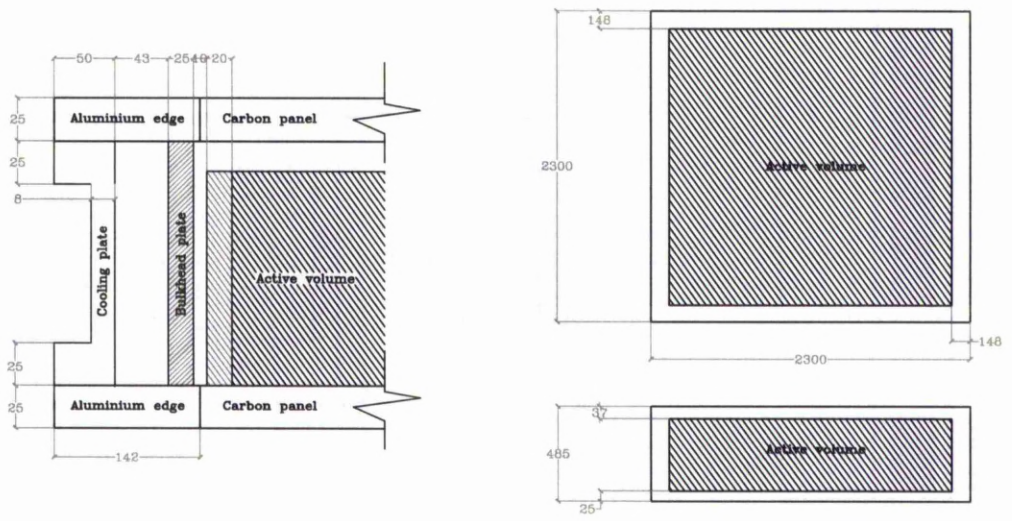

Figure 4.19: The active volume and details near the edge of the DsEcal.

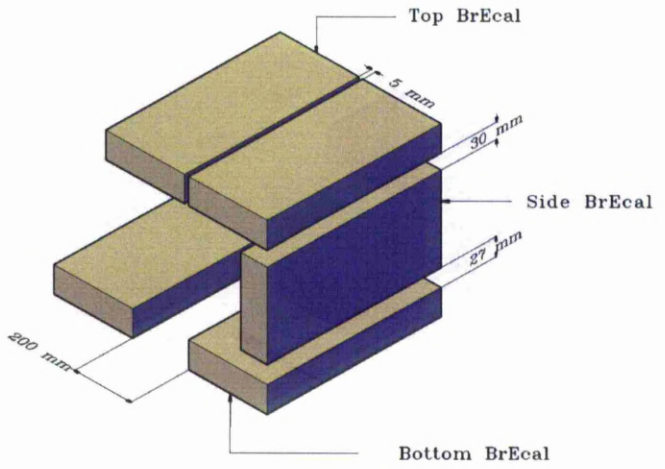

Figure 4.20: A 3D view of the commission of the BrEcal modules.

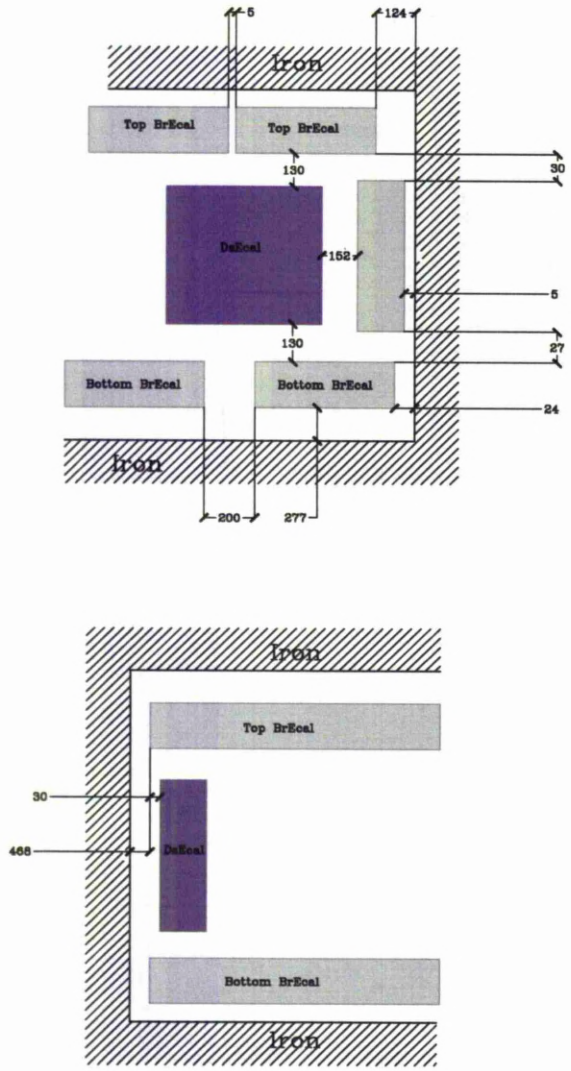

Figure 4.21: The back view (top) and side view (bottom) of the BrEcal and DsEcal modules as they are installed in the basket.

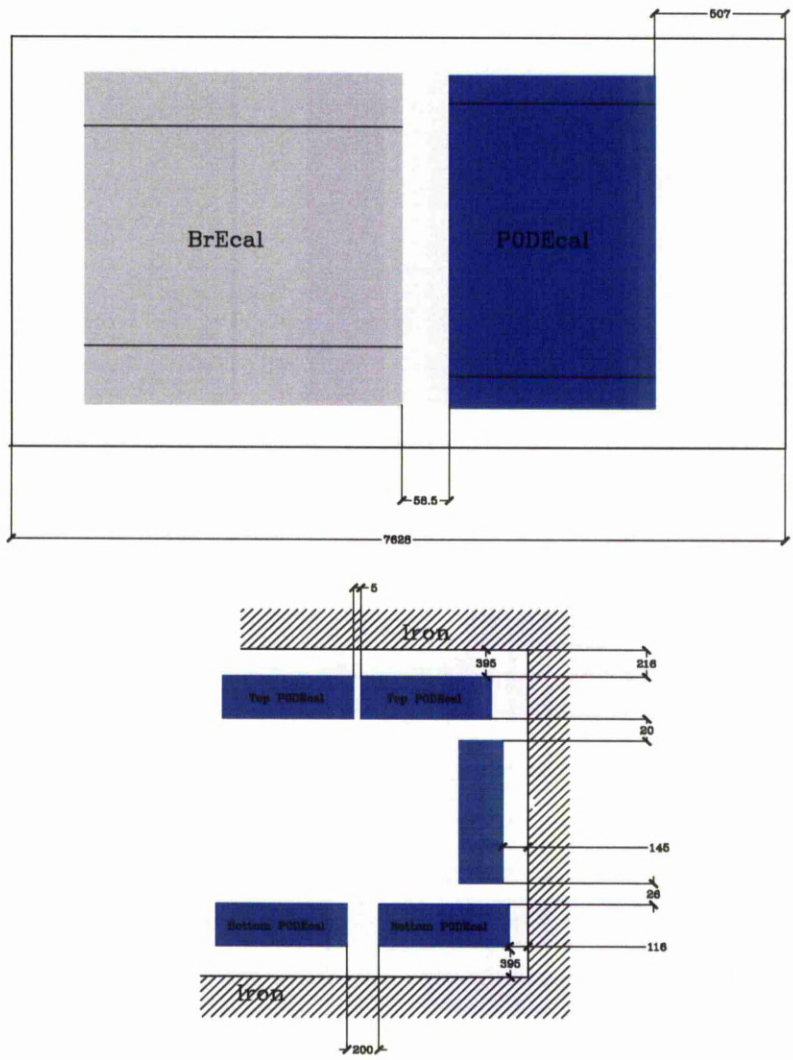

Figure 4.22: The side view of the BrEcal and P0DEcal modules (top) and the back view of the P0DEcal modules (bottom) as they were installed in the basket.

Chapter 5

Simulating the T2K

This chapter deals with the simulation of T2K. The simulation is separated into four main parts; the beam simulation, the neutrino interactions, the particle propagation in the detector material and the electronic simulation.

5.1 Beam Simulation

The purpose of the beam simulation is to produce the T2K neutrino (and antineutrino) fluxes for the near and far detectors. The proton interactions with the target and the propagation of the generated particles through the decay volume are simulated with the beam simulation algorithm called *jnubeam*. The pions and kaons produced are then decayed in order to provide the neutrino spectrum. Hadronic interactions are simulated using FLUKA [73]. GEANT3 [74, 75] is used for the particle propagation with the GCALOR [76] model to simulate the primary and secondary interactions outside the target area. The validation of the beam simulation is done using data from the NA61/SHINE experiment [77, 78], measuring the hadron production of 30 GeV protons smashed on a graphite target. The expected neutrino spectrum at Super-Kamiokande is shown in Figure 5.1.

5.2 Modeling the neutrino interactions

The understanding of neutrino interactions with matter is of particular importance with a lot of experimental and theoretical/phenomenological interest. In T2K we use two neutrino generators, GENIE [79, 80] and NEUT [81]. Although both generators use the same theoretical models to describe neutrino interactions, other things like the Fermi gas implementa-

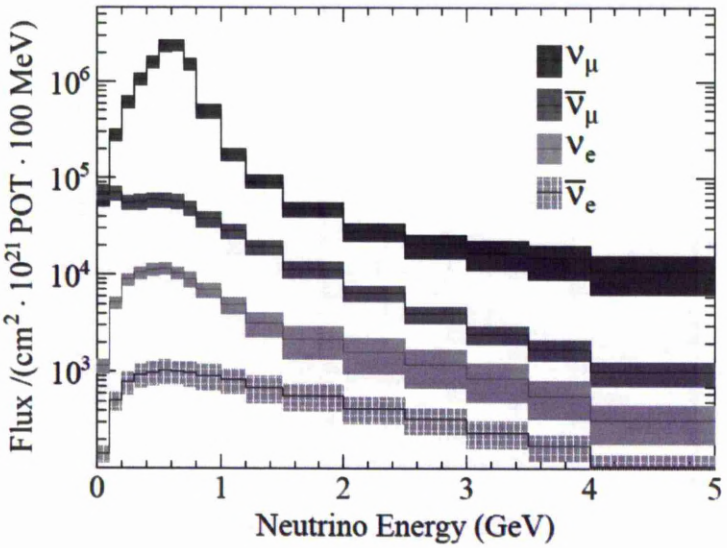

Figure 5.1: The expected neutrino flux at Super-Kamiokande. The shadow regions are the estimated error bars [62].

tion, hadronization and the resonance-DIS transition region are treated differently and may lead to different final state results. This comes with the necessity to compare the final state interactions from the two generators and understand the differences. The most important inclusive channels for Charge Current (CC) and Neutral Current (NC) neutrino scattering are shown in Table 5.1. Apart from these main neutrino interaction channels other channels are also simulated. For example, GENIE can also simulate quasi-elastic and DIS charm production, inverse muon decay and neutrino-electron elastic scattering [79, 80].

5.2.1 Quasi-Elastic Scattering

The quasi-elastic (QE) neutrino scattering is the most important neutrino interaction channel for T2K. Since the CC-QE interaction is a two-body interaction, the energy of the incoming neutrino can be reconstructed even if the hadron has not been observed.

The Llewellyn-Smith [82] model is used to model the CC-QE neutrino scattering, $\nu_l + n \rightarrow l^- + p$. In this model the hadronic current has the general Lorentz invariant V-A structure. Two of the six independent form factors are set to zero since they violate the invariance of strong interactions under the isospin transformations. Thus, the hadronic

CC Quasi-Elastic	$\nu + N \rightarrow l^- + N'$
CC Resonant	$\nu + N \rightarrow l^- + R$
CC DIS	$\nu + N \rightarrow l^- + X$
CC Coherent	$\nu + A \rightarrow l^- + A + \pi^+$
NC Quasi-Elastic	$\nu + N \rightarrow \nu + N$
NC Resonant	$\nu + N \rightarrow \nu + R$
NC DIS	$\nu + N \rightarrow \nu + X$
NC Coherent	$\nu + A \rightarrow \nu + A + \pi^0$

Table 5.1: Main inclusive channels for Charge Current (CC) and Neutral Current (NC) neutrino scattering. N and N' stand for a nucleon, A for a nucleus, R for a resonance and X for a multi-hadronic system.

current has the general form

$$J^{CC} = cos\theta_C \bar{u}(p) \left(\gamma_\alpha F_V^1 + \frac{i\sigma_{\alpha\beta} q^\beta F_V^2}{2M} + \gamma_a \gamma_5 F_A + \frac{q_\alpha \gamma_5 F_P}{M} \right) u(n), \tag{5.1}$$

with $Q^2 = -q^2$, M the nucleon mass, θ_C the Cabbibo angle, $F_V^{1,2}$ the vector form factors, F_A the axial form factor and F_P the pseudoscalar form factor. The differential cross section is expressed as [82]

$$\frac{d\sigma}{dQ^2} = \frac{M^2 G_F^2 \cos^2\theta_C}{8E_\nu^2 \pi} \left(A(Q^2) \mp B(Q^2) \frac{s-u}{M^2} + C(Q^2) \frac{(s-u)^2}{M^4} \right), \tag{5.2}$$

where the minus sign stands for neutrino and the plus sign for antineutrino, and,

$$\begin{aligned} A(Q^2) &= \frac{m_l^2 + Q^2}{M^2} \left\{ (1+\tau) F_A^2 - (1-\tau) \left(F_1^V\right)^2 + \tau(1-\tau) \left(F_2^V\right)^2 + 4\tau F_1^V F_2^V - \right. \\ &\left. - \frac{m_l^2}{4M^2} \left(\left(F_1^V + F_2^V\right)^2 + (F_A + 2F_P)^2 - \left(\frac{Q^2}{M^2} + 4 \right) F_P^2 \right) \right\}, \end{aligned} \tag{5.3}$$

$$B(Q^2) = \frac{Q^2}{M^2} F_A \left(F_1^V + F_2^V\right), \tag{5.4}$$

$$C(Q^2) = \frac{1}{4}\left(F_A^2 + \left(F_1^V\right)^2 + \tau\left(F_2^V\right)^2\right), \tag{5.5}$$

$$\tau = \frac{Q^2}{4M^2}, \tag{5.6}$$

$$s - u = 4ME_\nu - Q^2 - m_l^2. \tag{5.7}$$

Using the conserved vector current hypothesis (CVC) [83, 84] the vector form factors can be related to the electromagnetic form factors which have been measured in electron scattering experiments [85]. Different ways to parameterize the electromagnetic form factors can be found in the literature. The default option in GENIE is the BBBA2005 [86] form factors. BBA2003 [87] and Sachs [88] form factors are also available inside GENIE. Sachs form factors are used as default in NEUT.

Using the partially conserved axial current hypothesis (PCAC) [84] the pseudoscalar form factor F_P and the axial form factor can be related:

$$F_P(Q^2) = \frac{2M^2 F_A(Q^2)}{Q^2 + m_\pi^2}. \tag{5.8}$$

Thus, the 4 unknown form factors can be reduced to only one unknown axial form factor F_A. Usually the dipole approximation is used to parameterize the axial form factor:

$$F_A(Q^2) = \frac{g_A}{\left(1 + \frac{Q^2}{M_A^2}\right)^2}, \tag{5.9}$$

where M_A is the axial mass and $g_A = 1.267$ is the axial vector constant. M_A is now the only parameter left and needs to be measured from neutrino scattering experiments. The default value in GENIE is $M_A = 0.99\ GeV/c^2$ [79], while in NEUT using the K2K results [89] the default value for M_A is set to $1.2\ GeV/c^2$ [81].

For the elastic neutral current processes, GENIE uses the Ahrens *et al* model [90], with strange quark contribution to the axial from factor. In NEUT the neutral current elastic cross section is calculated using the relations from [91, 92].

5.2.2 Baryon Resonance Production

The Rein-Sehgal [93] model is used to model the baryon resonances for CC interactions

$$\nu_l + N \rightarrow l^- + N^* \tag{5.10}$$

and NC interactions

$$\nu + N \rightarrow \nu + N^*, \tag{5.11}$$

where $N^* \rightarrow \pi + N'$ is the produced resonance and N,N' the nucleons. The simulation follows the CC-QE, again with only one free parameter, the axial vector mass M_A

In NEUT, 18 resonances with $W < 2\ GeV/c^2$ are simulated. The cross section is calculated by summing the amplitude of each resonance production and then is multiplied by the resonance's probability to decay to a pion and a nucleon. With the same way and simply changing the decay products of the resonance, the cross section for resonance production of single η and K is computed. The interference of neighboring resonances and resonance absorption effects are taken into account. The default value of M_A is set to $1.2\ GeV/c^2$ [81].

In GENIE, only 16 resonances out of the 18 mentioned in the original Rein-Sehgal paper are considered. Interference between neighboring resonances is not taken into account. The default value for the axial mass is $M_A = 1.12\ GeV/c^2$ following the calculations in [94].

5.2.3 Deep Inelastic Scattering

The differential cross section for the CC deep inelastic scattering is given in terms of 5 real structure functions [95]

$$\frac{d^2\sigma}{dxdy} = \frac{G_F^2 M_N E_\nu}{\pi \left(1 + Q^2/M_W^2\right)^2} \sum_{i=1}^{5} A_i(x,y,E) F_i(x,Q^2), \tag{5.12}$$

where $Q^2 \equiv -q^2$, $x = \frac{Q^2}{2M_N(E_\nu - E_l)}$, $y = \frac{E_\nu - E_l}{E_\nu}$, $Q^2 = 4E_\nu E_l \sin^2\frac{\theta}{2}$, E_ν is the neutrino energy, E_l is the produced lepton energy, G_F is the Fermi Constant, M_N is the nucleon

mass, θ the scattering angle of the outgoing lepton and

$$A_1 = y\left(xy + \frac{m_l^2}{2M_N E_\nu}\right), \tag{5.13}$$

$$A_2 = (1-y) - \left(xy\frac{M_N}{2E_\nu} + \frac{m_l^2}{4E_\nu^2}\right), \tag{5.14}$$

$$A_3 = \pm xy(1-\frac{y}{2}) - y\frac{m_l^2}{4M_N E_\nu}, \tag{5.15}$$

$$A_4 = \frac{m_l^2}{xM_N^2}\left(xy\frac{M_N}{2E_\nu} + \frac{m_l^2}{4E_\nu^2}\right), \tag{5.16}$$

$$A_5 = -\frac{m_l^2}{M_N E_\nu}. \tag{5.17}$$

The plus sign in the A_3 structure factor applies to neutrinos while the minus sign for antineutrinos.

In GENIE, for the low q^2 region the modification suggested by Bodek-Yang [96] and the default values for the structure functions are determined using GRV98 parton distribution functions [97]. The resonant-DIS transition region is modeled assuming that the total differential cross section is the sum of the contribution from the differential cross section from the resonant channel and the differential cross section from the DIS channel. The resonant term expresses the low multiplicity channels and the cross section is calculated using the Rein-Seghal model. The DIS component uses the appropriate Bodek-Yang model plus an extra term expressing the multiplicity of the hadronic system. All the components also include an acceptance factor in order to match the low multiplicity channel, where the resonant contribution is important, to experimental data.

In NEUT, the Bodek-Yang [96] correction is implemented for GRV98 parton distribution functions [97]. To avoid double counting for $W < 2$ GeV, NEUT only generates events with more than one pion. An internal library is used to generate the events with $W < 2$ GeV using a probability function for the pion multiplicity, while for $W > 2$ GeV the PYTHIA/JETSET [98] library is used. The NC DIS cross sections are computed using the relations obtained from experimental data [99, 100].

5.2.4 Coherent Pion Production

The coherent neutrino-nucleus interaction is modeled using the Rein-Sehgal model [101, 102]. These processes, for CC interactions

$$\nu + A \rightarrow l^- + A + \pi^+, \tag{5.18}$$

and for NC interactions

$$\nu + A \rightarrow \nu + A + \pi^0, \tag{5.19}$$

where A is the target nucleus, assume a low momentum transfer to the target nucleus which is related to the pion field using the PCAC hypothesis [84].

5.2.5 Nuclear Effects

Since the nucleons are bound to the nuclei, Fermi motion and Pauli blocking are two important effects that need to be taken into account. The Pauli blocking accounts for the case that the interacting nucleon must receive enough energy to free itself from the Fermi sphere, thus its momentum must exceeds the Fermi momentum. For instance, in the case of carbon, the Fermi momentum is 221 MeV/c [103].

The intra-nuclear scattering of the produced mesons and nucleons are also important and need to be considered as well. For the T2K energy regime pion intra-nuclear scattering is one of the most important to consider. The pion absorption, charge exchange and scattering are implemented in the simulations. The scattering effect changes the final state pion momentum. The pion absorption and the charge exchange also change the final state topology. The nucleon scattering is also important since the nucleon momentum and direction can be changed. This is important for the near detector analysis, since the momentum threshold for the proton can be changed.

The intra-nuclear scattering effects for 1 GeV charged current muon neutrino interactions on oxygen, for both GENIE and NEUT is shown on Table 5.2 [104]. As it can be observed from this table there are some significant differences considering the π^0 intranuclear interactions, which may effect the MC prediction for the estimated background on the ν_e selection.

	GENIE	NEUT
$\pi^0 \rightarrow \pi^0$	75%	57%
$\pi^+ \rightarrow \pi^+$	75%	65%
$\pi^0 \rightarrow 0\pi$	20%	28%
$\pi^+ \rightarrow 0\pi$	20%	27%
$\pi^0 \rightarrow \pi^+$	2%	7%
$\pi^0 \rightarrow \pi^-$	2%	6%
$\pi^+ \rightarrow \pi^0$	4%	6%

Table 5.2: The intra-nuclear scattering effects for GENIE and NEUT. Event rates for single or non-pions final states, if there was a pion in the initial state [104].

5.2.6 Total CC cross section

Figure 5.2 shows the total ν_μ CC cross section for quasi-elastic, single pion and inclusive scattering from an isoscalar target for GENIE. Details for the data points appearing on the plot can be found in [79]. Figure 5.3 shows the total ν_μ CC cross section for NEUT. Details for the data points appearing on the plot can be found in [81].

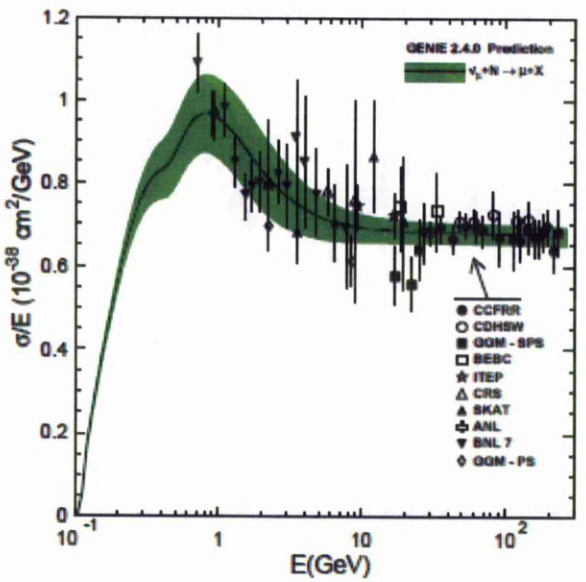

Figure 5.2: The total neutrino CC cross section for GENIE. Solid line shows the simulated cross section. The green band shows the estimated uncertainties. From [79].

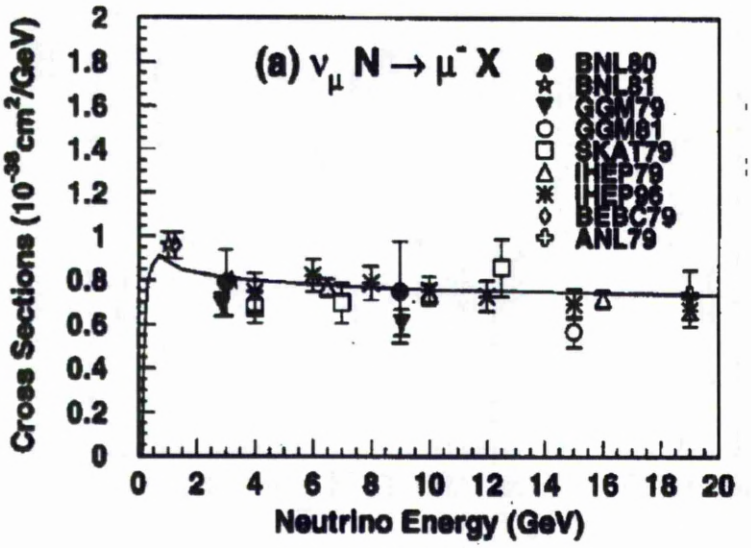

Figure 5.3: The total neutrino CC cross section for NEUT. Solid line shows the simulated cross section. From [81].

5.3 Super-Kamiokande detector simulation

The final state particles generated from the neutrino generators are propagated through the Super-Kamiokande detector. SKDETSIM is then responsible to simulate the propagation of these particles in Super-Kamiokande. SKDETSIM is based on GEANT3 along with the CALOR physics package for a better simulation of the hadronic interactions in the water. However, for pions with momentum below 0.5 GeV/c, special routines have been written to improve the simulation [105].

5.4 ND280 detector simulation

The neutrino generators can simulate the neutrino interactions and store all the kinematic variables for the final state particles. The next step is to propagate the final state particles through the detector material using realistic detector geometry. GEANT4 [74, 75] is used to simulate the passage of the particles through the ND280 detector, simulating the energy deposit of a particle along its path length into digits. Each digit can save the information about the energy deposit amount, the position and the time. The electronics simulation takes these digits and transforms them into hits. The hits have the same format as the actual

experimental data and are input into the calibration and reconstruction software.

For scintillator detectors, we simulate the position of a hit in a scintillation bar and the amount of energy that this hit should have deposited in the corresponding bar. This energy is then converted to a number of photons produced by the WLS fiber. Birk's law correction [106] is applied to describe the scintillator energy response and then an attenuation effect is also applied to the photons depending on the hit's distance to the MPPC. The MPPC is parameterized as a net of pixels, each one firing a charge amount if a photon hits it. Cross talk and after-pulsing effects are also taken into account. Thus the generated hit will eventually associate with a total charge given in photo-electrons.

The TPC simulation approximates the waveform analysis of the AFTER chip by saving the charge and the time information for each pad. The response function for the AFTER chip depends on the electronics parameters and mainly from the conversion factor from electrons to ADC, the shaping time and the sampling time. The simulation of the ionization energy loss along a TPC track includes the effect of the electric and magnetic field and drifting the electron cloud to the MicroMegas. The number of electrons is given from the division of the energy loss estimation to the ionization potential, $W_I = 26.8$ eV. The electrons are then drifted, with a constant drift velocity, to the detection point. Thus, the drift time is only proportional to the drift distance. The MicroMegas gain is simulated individually for each electron arriving at the readout plane. Event by event fluctuations for the gain simulation are also considered.

Chapter 6

Event Reconstruction in ND280

The purpose of the chapter is to discuss the details about the event reconstruction in the near detector ND280, and particularly for the FGD, TPC and ECal, since these are the main detectors used for the data analysis and particle identification (PID) presented in the next chapters. The beginning of this chapter will also give a basic introduction to the ND280 off-line software which is important for the data processing and for the reconstruction algorithms. The global[1] tracking and vertexing will be discussed towards the end of this chapter.

6.1 The ND280 off-line software

The ND280 off-line software is suite consists of about 55 packages responsible for simulation and reconstruction of particles passing through the ND280 sub-detectors. The main package, responsible for the software handling from the time the raw files are converted into the off-line format until the very end of the software routine, is called "oaEvent". Calibration constants are applied during processing time and they are retrieved from a MySQL database. All sub-detectors have dedicated software packages responsible for their calibration and reconstruction. The RecPack [107] reconstruction toolkit is used as a framework for the reconstruction along the detector. The final stage of the software chain is the translation of the oaEvent library into a plain analysis library, which is a pure ROOT format.

[1] The definition of global reconstruction refers to any track or vertex reconstructed using information from more than one sub-detector.

6.2 Tracker Event Reconstruction

The two FGDs will provide the target for the neutrino interactions and are described in chapter 3.4.2. A brief introduction to the FGD reconstruction will be discussed in this chapter. The TPC is the main tracking and PID tool measuring the energy loss of a charged particle. The description of the T2K TPCs are presented in chapter 3.4.3. Here a brief description on the TPC reconstruction and PID will be discussed. Although the TPC-FGD matching is performed as a part of the tracker reconstruction it will be discussed in more detail in the global reconstruction section 6.5.

6.2.1 FGD reconstruction

The reconstruction of the FGD hits is important for the neutrino interaction vertex reconstruction and for the TPC-FGD matching. First, different sets of FGD hits are created based on their time. The TPC tracks are then matched to the FGD hits using a Kalman filter as discussed in section 6.5. For tracks that do not enter the TPC, the FGD standalone reconstruction takes the isolated FGD hits and using a pattern recognition algorithm tries to connect them and create the FGD track. This is performed separately for the XZ and YZ projections. The two projections are finally matched together to create a XYZ track.

6.2.2 TPC reconstruction

The TPC reconstruction creates clusters and then joins these clusters to reconstruct the track. The clusters are formed by a sequence of spacetime overlapped wavefunctions. A wavefunction represents the charge selected by a pad along with the readout time. After the pad by pad charge selection is completed the gain calibration and the noise reduction are applied. The total charge of the cluster, C_C, is then the sum of all the pad charge which are consistent in space and time and in the same MicroMegas column.

The clusters are then connected to form a track using a pattern recognition algorithm. The pattern recognition algorithm connects clusters to create track segments in such a way that the longest possible track segment is reconstructed. The time of a reconstructed TPC track can't be obtained since the electron drift time is 3 μs, which is much larger than the beam spill time. Thus the primary time for a track is obtained either from the FGD or from

the ECal, with a resolution of a few ns. A track crossing the whole TPC consists of 72 clusters.

For the track reconstruction two methods can be used. The likelihood method takes the angle and the direction of the track to predict the deposited charge and then compares that with the observed charge. The charge deposit is assumed to be constant for each row. The second method is called the point reconstruction method and uses a helix model to fit the reconstructed points.

After the track reconstruction the TPC particle identification routine is applied. The PID in the TPC is performed using the truncated mean method. The truncated mean energy deposit per horizontal segment is defined as [108]

$$C_T = \frac{1}{\alpha N} \sum_{i}^{\alpha N} C_C(i), \tag{6.1}$$

where α is the truncation factor, N is the number of clusters in the TPC and $C_C(i)$ is the energy of the i cluster.

As can be seen from equation 6.1 the truncated mean depends on the number of clusters and on the length of the track. Thus, a more useful expression could be the calibrated truncated mean defined as [108]

$$\bar{C_T} = \frac{1}{\alpha N f(N)} \sum_{i}^{\alpha N} g(d_i) C_C(i), \tag{6.2}$$

with $f(N)$ a calibration factor depending on the number of clusters and $g(d_i)$ a calibration factor depending on the sample track. Both $f(N)$ and $g(d_i)$ approximate to one for horizontal tracks.

With the truncated mean method, the most probable deposited energy of a particle with mass m is calculated which is only a function of the $\beta\gamma$ [108]. This is different from the Bethe-Bloch formula calculating the average energy deposit per unit length.

The sigma, σ_T, on the truncated mean calculation is given by [108]

$$\sigma_T = \sigma_0 \zeta(d) \xi(N) \sqrt{\frac{C_E}{C_E(MIP)}}, \tag{6.3}$$

with σ_0 the Gaussian width for the MIP reference track, $\zeta(d)$ and $\xi(N)$ the calibration factors, C_E the expected energy loss for the measured track and $C_E(MIP)$ the expected energy deposit for the MIP reference track.

6.3 ECal Event Reconstruction

The main purpose of the ECal reconstruction algorithm is to take the raw ECal hits and create a cluster. A cluster is a set of hits assumed to belong to the same particle, carrying also information about the particle's kinematics and energy. The reconstructed cluster will then be used as input for the particle identification (PID) algorithm, responsible for making the particle hypothesis.

The first part of the clustering algorithm takes the individual hits, splits them into 2D views and group them according to their time. For the double ended bars, a summed charge and charge weighted mean from both bars is calculated.

The hit is calibrated in terms of MIP units. A MIP unit is defined as the amount of charge a MIP particle will deposit traveling a distance of 1 cm of scintillator in the detector. The charge is also corrected for the attenuation of the scintillation light traveling through the WLS fiber to the MPPC.

Once the hit reconstruction is done, the basic clustering algorithm is called to cluster neighboring hits. The highest charge hit is used as the seed hit. A scan is performed to search for hits around the seed hit; these hits must in two layers distance or in the neighbor bar and have 15 ns time difference from the seed hit. For the hits matched, the same procedure continues to find more unmatched hits. Finally all the hits matched are grouped to form the cluster.

After the hits are grouped and calibrated, the clustering algorithm tries to combine separate clusters, split during the first stage of the clustering algorithm. This step takes the longest cluster and calculates its direction using a principal component analysis (PCA). The cluster is then extrapolated in both forward and backward directions looking for other neighboring clusters. The clusters matched must also be in time. The clustering expansion has a second step trying to combine a cluster with individual un-clustered hits. The cluster expansion is a similar method with the cluster combine method using the PCA to define an

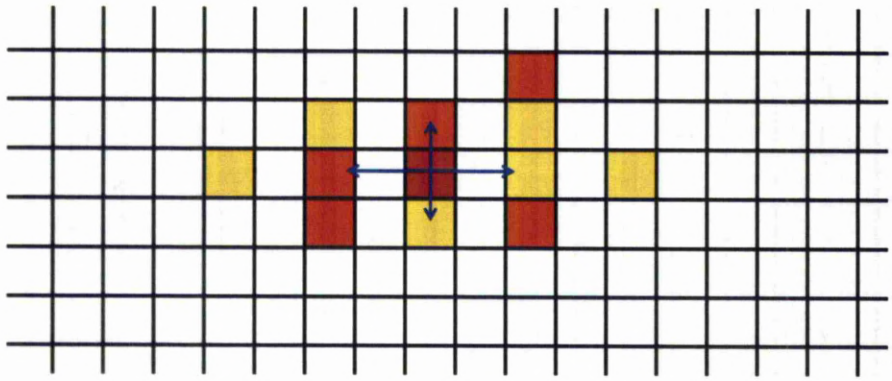

Figure 6.1: A cartoon demonstrating the basic cluster algorithm. The highest charge hit is used as the seed hit and a search for hits in the neighbor bars and second layer is performed. The same procedure continuous for all the other hits matched with the seeded hit.

ellipse in space and time, looking for un-clustered hits along the direction of the cluster. A timing cut at 40 ns is also applied to remove any noise contamination.

After the combine and expand cluster algorithm the cluster match algorithm takes the 2D views of a cluster and matches them together to generate a 3D cluster by checking a likelihood fit with two input parameters, the charge ratio and the difference in the starting position of the clusters. The minimum number of hits to form a cluster for each 2D view is three, thus for a 3D cluster the minimum number of hits required is six [2]. Since the orientation of each ECal is different, different views are fitted for different ECals.

After the clustering algorithm is finished the energy of a cluster is reconstructed. The

[2]This is the case at the time this analysis is performed. Recent developments have reduced the minimum number of hits required to make a cluster below six.

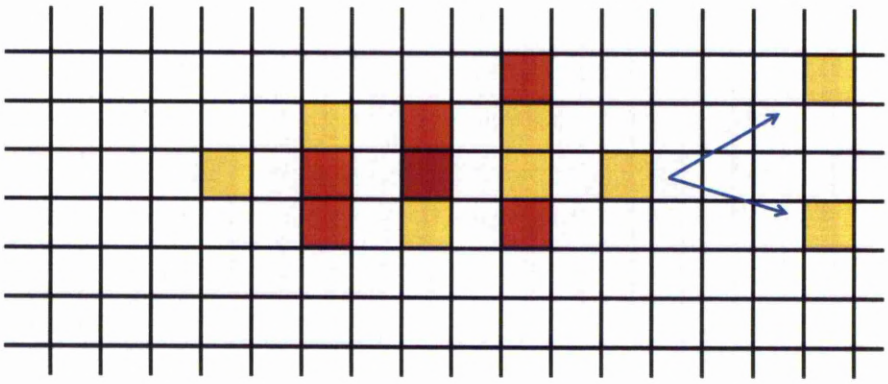

Figure 6.2: A cartoon demonstrating the expand cluster algorithm. The seed cluster is extrapolated backward and forward to match with neighboring hits or clusters.

energy reconstruction algorithm assumes that the incoming particle is either a photon or an electron. The energy reconstruction is tuned by firing photons into the calorimeter in a range of 53 known energies from 75 MeV up to 25 GeV. The energies of these photons are not uniformly distributed in the 75 MeV-25 GeV range; most of them are populated below 2 GeV. For each energy the total charge, the skew of the charge and normalized RMS of the charge (i.e. the RMS of the charge divided by the mean of the charge) are selected. Since these parameters are depending on the input energy, they are also correlated with it. The selected parameters are fit to a multi dimensional skewed Gaussian function with correlations, and the most likely energy of a particle is extracted from the likelihood fit. Thus, the reconstructed energy fit for EM particles is expected to be good, while for MIPs or hadronic particles it is expected to be incorrect. For through-going MIPs, the energy fit result is independent of the MIP momentum, since MIPs will deposit in average the same

amount of charge per cm until they exit the detector.

The energy reconstruction has been tuned only on MC, it is sensitive to calibration routines and electronic simulation, but, it has been tested using the DsECal testbeam (see chapter 7).

After the energy reconstruction, the PID algorithm is run in order to classify a cluster as a track or a shower. Both the track and the shower hypothesis are fit and the output is saved for analysis purposes. The separation between hadronic and electromagnetic showers can also be performed to some extent but is energy dependent. The ECal PID power for electrons and photons is poor at the moment, but the presence of the TPC can tag an electron track and help to distinguish them. For low energy particles, $p < 150$ MeV/c, with only a few cluster hits it is very hard for the PID to distinguish between a stopping track and a shower. The ECal PID algorithm also returns a likelihood with information about the track or shower hypothesis. The next sections describe with more details the output and the performance of the ECal PID.

An independent method for the particle PID has been developed using the Kalman filter [109, 110] to follow the trajectory of a track or a shower on a hit by hit basis. More detail about this PID can be found in the next sections of this chapter and at the next chapter where the DsECal testbeam is used to demonstrate the performance of the Kalman filter PID.

The final step for the ECal reconstruction algorithm is to find the kinematics and space properties of each track or shower. For tracks, each hit along a bar defines a track node. The track node is basically a 3D position for each hit, but can also store other information as well such as the direction and the curvature. While the hit position stored in the track node is computed earlier in the reconstruction, the direction of the track node is computed from a straight line fit by taking four neighboring (two forward and two backward) nodes. The node closest to the tracker region is taken as the initial node for the reconstructed track. This is under the assumption that the tracks are always coming from the tracker. The curvature is not defined since for such high density objects as the ECals, the scattering probability increases dramatically, thus a single curved track can't be assumed. Hence the curvature is set to zero.

For showers, the fit along its direction is more complicated, as the shower can have a non-isotropic spatial spread. The PCA is used to create an ellipse in order to describe the shower shape or if assuming that the particles come from the tracker a cone is defined with a position, direction and an opening angle. Another approximation to determine the shower direction is to use the thrust analysis. The thrust analysis uses the back/front asymmetry of the shower and the front of a shower to point the direction.

The ECal reconstruction also looks for Michel electrons by searching for delayed clusters or hits. If any delayed clusters or hits are found each cluster is then tagged as a Michel electron cluster.

6.3.1 Particle Identification in the ECal

During the ECal reconstruction a set of variables are produced in order to distinguish between a track and a shower. Electromagnetic and hadronic showers can also be distinguished to some extent. A short description of the main ECal PID variables is given below; more details can be found in [111]. The variables described here are those used as input in the neural network calculation or used later to discriminate between a track and a shower during the physics analysis. The TMVA package [112] is used as the framework for the neural network. The returned track-shower variable (TrShVar) from the neural network ranges from 0 to 1. For perfect tracks TrShVar should be approximately one, while for perfect showers it should be approximately zero. The distribution of the input parameters in the neural network is shown in Figures 6.4- 6.7, using the DsECal testbeam (see chapter 7 for more details). The differences between MIPs and showers are visible from these plots.

Axis Max Ratio (AMR)

AMR (Figure 6.3) follows a cluster along its direction and searches for the position of the hits. At each step the ratio of the length of the cluster to the width is calculated, weighted by the hit charge, and the maximum value is finally returned. If the computed ratio is infinitely large then it is set to 300. Thus, the AMR should approximate zero for a shower and be significantly larger than zero for a track.

Maximum Charge Ratio

Computes the per layer ratio of the highest charge hit to the lowest charge hit (Fi-

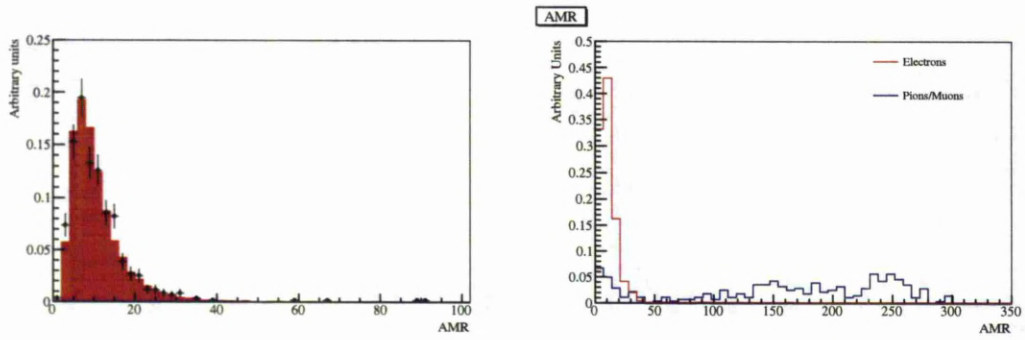

Figure 6.3: AMR distribution for testbeam electrons (left) and testbeam electrons with pions/muons (right) at 1 GeV/c.

fure 6.4). Since this variable depends only on the hit charge, it is then sensitive to noise and calibration routines. For example, due to temperature instabilities during the DsECal testbeam (chapter 7), the shape difference observed for electrons in Figure 6.4 could suggest some noisy hits or differences in the highest hit charge between data and MC.

Shower Angle

PCA is used to determine the direction and the angle of a cluster (Figure 6.5).

Shower Width

Shower width, shown in Figure 6.6, computes the width of a cluster.

Electromagnetic energy fit likelihood

The likelihood for the energy fit can also be used as a PID tool. Since the energy is reconstructed assuming electrons or photons, the likelihood of the energy fit is expected to be worse for hadrons and muons (see Figure 6.7).

6.4 The Kalman Filter and the ECal PID

Although the main purpose of the Kalman filter [109, 110] is to match long tracks between the subdetectors (see the Global Analysis section 6.5 for more details of the Kalman filter and the detector matching) it can be also used as a PID tool to discriminate between a track and a shower in the ECal. The key idea is that the Kalman filter can follow the path of a particle in the ECal on a hit by hit basis.

Starting with an initial seed state, each hit position along the particle's path is fitted with

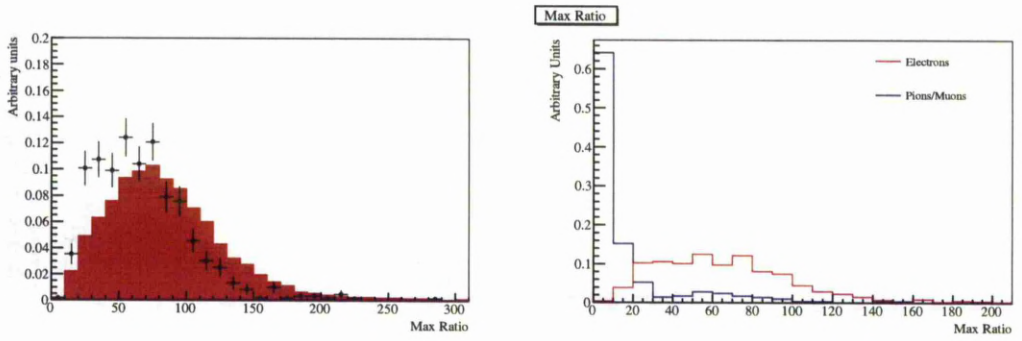

Figure 6.4: Maximum charge ratio distribution for testbeam electrons (left) and testbeam electrons with pions/muons (right) at 1 GeV/c.

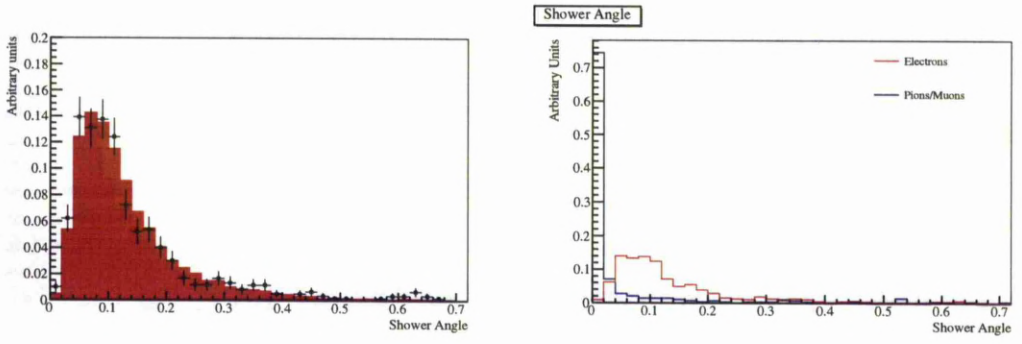

Figure 6.5: Shower angle for testbeam electrons (left) and testbeam electrons with pions/muons (right) at 1 GeV/c.

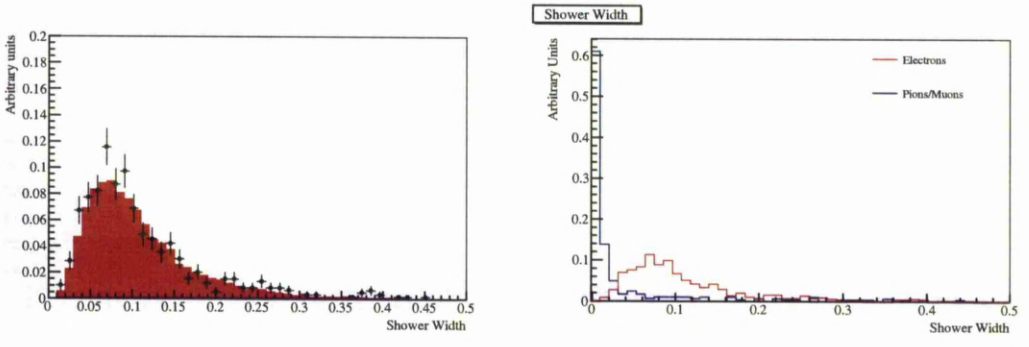

Figure 6.6: Shower width for testbeam electrons (left) and testbeam electrons with pions/muons (right) at 1 GeV/c.

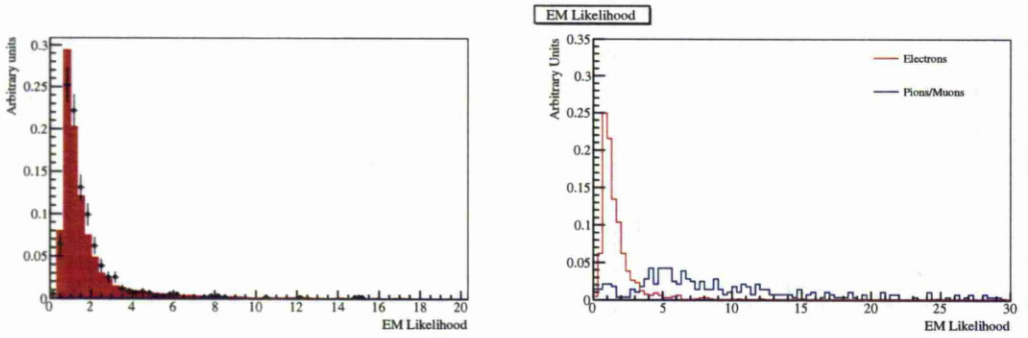

Figure 6.7: EM energy likelihood fit for testbeam electrons (left) and testbeam electrons with pions/muons (right) at 1 GeV/c.

respect to the last seed state and if the fit is successful, the hit will be added to the track or shower. For tracks, this is continued until the track exits or stops in the ECal or if the fit fails for two continuous hits. For showers on the other hand, some special care needs to be taken. This is done with two approaches.

The first is a geometrical approach. In the geometrical approach the hits are sorted by increasing layer and if two continuous layers with more than two hits are found then the Kalman filter stops and the object is treated as a shower. The second approach is to leave the Kalman filter to fit all the shower hits and then store the worst hit fit. The idea behind this is that we can initially define a representation (i.e. a direction) along which the Kalman filter will look for hits, for example along the z-direction. The filter will easily follow the trajectory of a track along the default representation and the calculated χ^2 is expected to be small. But for showers, since they widely spread along the three dimensions the χ^2 along the default representation will be worse.

If a TPC track exists the initial ECal seed state needed is taken from the last state of the TPC track and is then extrapolated to the ECal. If the extrapolation is successful, the TPC track is matched to an ECal cluster and the routine described above continues. So this method can also be used to incrementally match the ECals with the other detectors. For neutral clusters, a seed state close to the first hits is reconstructed and the Kalman filter is called to perform the PID check.

The limitation of this method is for particles entering the ECal at very large angles. This

is because the Kalman filter has been set to follow the path of a particle along a specific direction, but at very high angles the particle's more probable direction may be different from the Kalman filter chosen. This may lead to a relatively higher mis-identification rate for tracks going through the entire ECal. The validation of the Kalman filter as a PID tool in the ECal will be demonstrated using the DsECal testbeam data in the next chapter.

6.5 The Global Reconstruction

The global reconstruction is responsible for combining the reconstruction from all the ND280 detectors and returning a global object. The global object will carry along all the useful information from the reconstruction including vertexing, charge, momentum and the PID from all the detectors.

One of the most important properties of the global reconstruction is the track matching between the detectors. After the TPC reconstruction, the TPC tracks are extrapolated forward and backward searching for hits in the two FGDs. The matched FGD hits are then grouped as FGD tracks. Then the TPC and FGD tracks are merged together to create a combined TPC-FGD track. Thus FGD1-TPC1, FGD1-TPC2, FGD2-TPC3, and FGD1-TPC2-FGD2 tracks are created. The pairs created are then matched together and if the matching quality is good then they are merged together using the Kalman filter [109, 110] to create the tracker tracks. The implementation of the Kalman filter is defined in the RecPack [107] package. RecPack is also used to estimate the energy loss of a particle in the TPCs. The track momentum and energy loss in the TPC have a negligible impact in the FGD-TPC matching.

If a track goes through both FGDs, the time difference between FGD2 and FGD1 is checked and if it is less than 3 ns then the track direction is reversed.

Any other tracks in the POD, the ECals and the SMRD are reconstructed individually and they are finally matched together with the tracker tracks using the Kalman filter to create the longest possible track in the whole detector. Possible expansion of the incremental matching between the tracker and other detectors is also possible.

The SMRD-Tracker incremental matching works in a similar way as the FGD-TPC matching described above. The reconstructed tracker track is extrapolated in the SMRD

planes looking for SMRD hits. Each SMRD hit is filtered and merged in the track and the trajectory of the track is expanded through the whole SMRD.

The ECal-Tracker incremental matching is currently working only for the TPC-ECal. The last reconstructed state of the TPC track is extracted and is matched with hits from the reconstructed ECal cluster. If an ECal cluster is found, then an attempt to match the first reconstructed hit of the cluster with the seeded last state of the tracker track is performed. If the fit quality is good then the next ECal hit is filtered along the chosen direction (the direction to look for ECal hits is different due to different orientation of the ECal modules). For ECal tracks, this is continued until the track exits the ECal or until the hit filter fit fails twice. Because of the shower possibility of the ECal, special care must be taken. Thus, the hits are first grouped per layer and if two continuous layers with more than two hits is found then the Kalman filter is stopped and the object is treated as a shower. Also a second fit is performed, leaving the hit filter to fit all the shower hits and the corresponding χ^2 is stored.

The vertex point is also associated with the global object. This is currently working on the top of the tracker reconstruction algorithm and looks for vertices in the tracker region. The vertex finding quality depends on the input track quality. For example, broken tracks or misfit hits for a track could decrease the efficiency of the vertex finding algorithm. The method is equivalent to choosing the initial position of the track for events with a single track, but it is much more sophisticated to find the vertex position for multi-track events.

One of the most important characteristics of the vertex reconstruction algorithm is to have a first estimate of the vertex position. The first estimation of the vertex position is assumed from reconstructed tracks in the XZ-plane (i.e. the direction with no perturbation from the magnetic field). A straight line propagation in the XZ-plane is used to find the initial and final points of each track. The angle and the Z-distance of the tracks are checked to make sure that they are not part of a longer, broken track. If a track is found to be broken the most downstream position along Z is taken for the vertex position calculation. The closest point of approach is then computed analytically between each pair of tracks. The cluster position from the pair is then calculated from the closest position in y from the track end. More tracks are then added to the same cluster if the x and z position are matched with

some precision. Since the position of the cluster is now known, the track state closest to the cluster is found. The position and each track state are then given as input to the Kalman filter.

The cluster position is then set as the vertex position and all the tracks are filtered using RecPack in descending momentum order. The χ^2 is calculated for each attempt to fit the closest track state to the vertex position. If the χ^2 is higher than a nominal value the corresponding track is removed. If there are at least two tracks associated with the vertex position the inverse Kalman filter is run. The inverse Kalman filter, starting from the vertex position, will remove an individual track checking the χ^2.

The vertex position with the highest momentum track and most downstream z-position is selected as the vertex position. If the most energetic track associated with the vertex position lies farther down the vertex position, then the vertex is qualified as a secondary vertex. If the highest momentum track, from all tracks (not only those that associated with the vertex position), is not associated with the vertex position and is more downstream from the z vertex position, then its position is assumed to be the vertex position.

More details and validation of the vertex reconstruction algorithm can be found in [113]. The vertex reconstruction will be studied in more detail during the analysis procedure in Chapter 8.

Chapter 7

The DsECal Testbeam

For calibration purposes the DsECal was shipped to CERN and tested using the T9 beamline. The proton synchrotron facilities at the east experimental area at CERN smashes protons on a solid target and the resulting particles will form a beam aimed at the DsECal. The beamline can produce particles with momentum from 300 MeV/c up to many GeV/c. Particles with momentum from 300 MeV/c up to 4 GeV/c are selected. A simplex of magnets is then used to focus the particles and select their momentum and polarity; electrons, pions and protons are mainly produced and a contamination of muons is expected. Kaon and deuteron population contamination is expected to be tiny. We positioned the ECal to collect particles with incident angle at 0, 30 and 60 degrees. The testbeam experimental set up is shown in Figure 7.1. More details about the experimental setup of the T9 beamline and the expected composition of particles can be found in [114].

For the particle identification before the particles enter the DsECal, two carbon dioxide Cerenkov counters and a time of flight (TOF) detector are used. The Cerenkov counters separate electrons from the other particles, the TOF is used to separate pions from protons at momenta below 1.8 GeV/c. For momenta above this only an electron-hadron separation is possible. The TOF and Cerenkov channels are connected to a low and high gain ADC. A cut on the ADC values for both Cerenkov and TOF is applied in order to select the best quality particles with the highest efficiency. For TOF the well defined peaks for electrons/pions and protons are fitted with a Gaussian and the particles within 3σ of the peaks are selected. Both the Cerenkovs, must return a signal above 180 ADC to be selected as an electron and zero to select pions or protons. The TOF peak for electrons/pions and protons, and

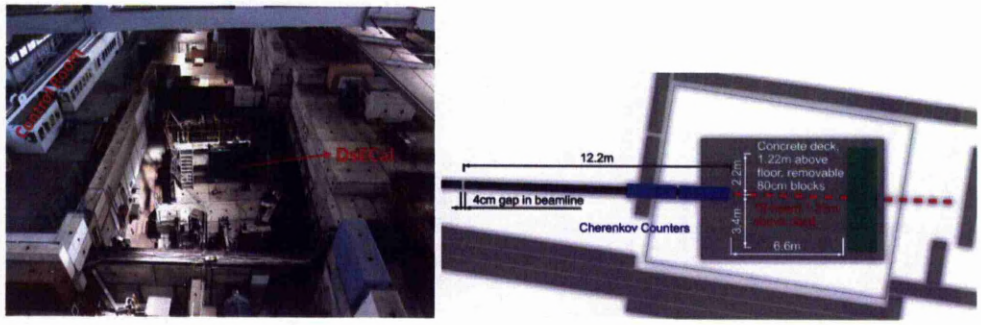

Figure 7.1: The experimental set up for the DsECal testbeam at the CERN T9 experimental area.

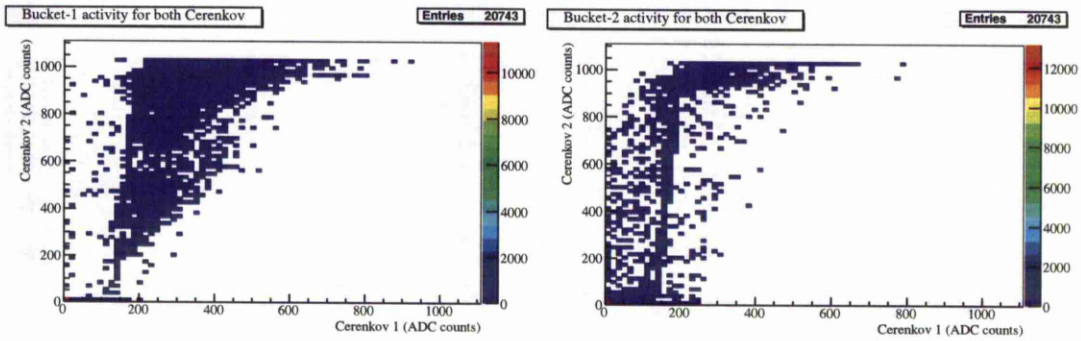

Figure 7.2: Cerenkov detector activity for negative charge particles with momentum of 0.8 GeV/c.

the Cerenkov activity at 0.8 GeV/c for negative and positive charge particles are shown in Figures 7.2,7.3.

Before testing the ECal PID and the energy reconstruction, three cuts are implemented. The first is a cut on the average hit time in order to reject non-beam events. The second is by selecting events with only one reconstructed cluster, in order to remove double counting. The last cut is to remove events reconstructed near the edges of the DsECal.

The current DsECal testbeam analysis is particularly focused on electrons. The unknown contamination of muons in the pion sample, makes the pion study to be quite challenging. The negative charged dataset at 30 degrees has been chosen for the testbeam electron analysis. The 30 degrees dataset appears to be the most appropriate for analysis purposes since for the 0 degrees dataset no regular pedestal run was taken, making the cal-

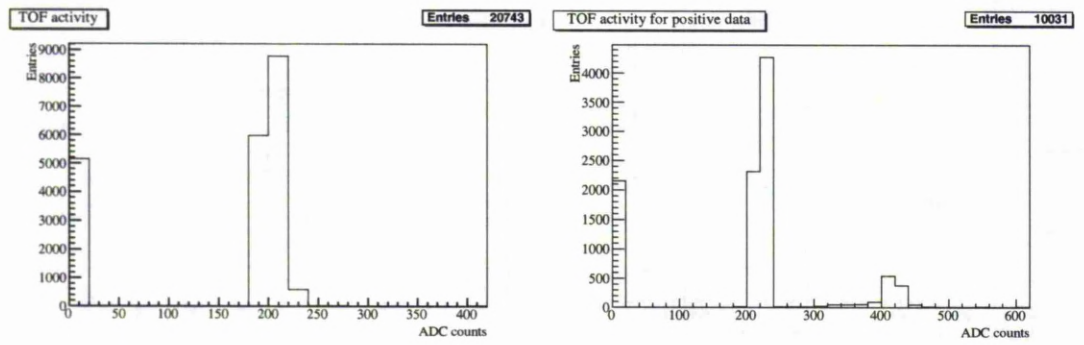

Figure 7.3: Time of flight detector activity for negative charge particles (left) and positive charge particles (right) with momentum of 0.8 GeV/c. The high peak corresponds to electron/pion/muon and is visible on both negative and positive data. The smaller proton peak is also visible in the positive data.

ibration much more challenging. Also the negative dataset has been chosen instead of the positive, since it has more statistics and is less noisy. For momenta above 2 GeV/c, since a pion could also leave a signal in the Cerenkov detectors, a cut at 3 σ from the energy mean is applied for the electron selection. Table 7.1 summarises the negative particle selection for all momenta at 30 degrees.

The reconstructed energy for each momentum is fitted with a Gaussian distribution. A 8.5 % correction is uniformly applied to all the testbeam momenta in order to centralise the reconstructed energy to the nominal momentum. A positive 5-10 % discrepancy on the reconstructed energy for the data below 0.6 GeV/c has been observed. The reason why this data, even after the energy correction, fits at higher momenta is currently unknown. A possible explanation could be that the data below 0.6 GeV/c is much more noisy than the other data. Although a basic noise reduction has been applied at the calibration and reconstruction stage, a run by run check for noise reduction has not been applied. A check during the analysis stage for channels continuously firing a large amount of charge has been performed returning none. Another possible explanation could be because of the beam focusing magnet instability at low momenta. As it is shown later, when the DsECal PID is tested the data below 0.6 GeV/c agrees quite well with the MC. For the study of energy resolution for the problematic momentum region the reconstructed energy is assumed, but, with a larger error corresponding to the difference from the nominal momentum.

Nominal Momentum (GeV/c)	Electrons Selected	Pions/Muons Selected
0.3	1324	167
0.4	3039	343
0.5	1034	157
0.6	5675	858
0.7	1672	260
0.8	1607	454
0.9	846	174
1.0	862	272
1.2	284	189
1.4	612	424
1.6	377	481
1.8	294	606
2.0	338	1033
2.4	116	771
2.8	207	2063
3.0	54	1020
3.2	272	3365
4.0	40	1548
Total	18653	14185

Table 7.1: Number of selected electrons and pions/muons at 30 degrees negative beam during the DsECal testbeam at CERN T9 experimental area in 2009.

For the MC, electrons are shot in a 30 degrees angle to the DsECal for all the momenta, see Table 7.2. The MC reconstructed energy is also fitted with a Gaussian distribution and the correction applied to centralise to the nominal momentum is 5.2 %. For the energy resolution study, this difference on the reconstructed energy correction between the data and the MC is treated as a systematic uncertainty. The reconstruction efficiency shown on Table 7.2 is defined as

$$\text{ECal Reconstruction Efficiency} = \frac{\text{Reconstructed electrons}}{\text{Generated electrons}}. \tag{7.1}$$

The difference in the low and high momenta is due to the fact that at higher momenta quite energetic electrons or photons from the primary shower can create secondary showers. These events are rejected since if the secondary electrons are quite energetic they could lead to underestimate the reconstructed energy of the primary electron shot into the ECal.

Table 7.3 shows the energy reconstruction for data and MC in the momentum range 0.7-2.0 GeV/c. The energy reconstruction, number of cluster hits and the track-shower discrimination variable for the 0.8 Gev/c and 2 GeV/c momentum are displayed in Figure 7.4. The ECal PID is also tested for the electron and the pion/muon samples for the 0.8 GeV/c and 2 GeV/c momenta. Figure 7.5 shows the PID for electrons/pions/muons in these momenta.

The electron mis-identification probability is also important. Figure 7.6 shows the fraction of events with TrShVar > 0.4, i.e. electrons mis-identified as tracks for all the testbeam momenta, with a good agreement between data and MC. The TrShVar, as described in section 6.3, is the output from neural network and approximates one for perfect tracks and zero for perfect showers.

Figure 7.7 displays the ECal energy resolution. Both the data and the MC are fitted with a stochastic resolution term in the range 0.3-2 GeV/c,

$$\frac{\sigma}{E} = \frac{A}{\sqrt{E}}. \tag{7.2}$$

For the data

$$A_{Data} = (9.8 \pm 0.2), \tag{7.3}$$

with $\chi^2/\text{ndof} = 13.1/12 = 1.1$. For the MC

$$A_{MC} = (7.3 \pm 0.2), \tag{7.4}$$

with $\chi^2/\text{ndof} = 2.6/12 = 0.2$.

The difference between the testbeam data and MC is due to a small, unknown spread in the beam momentum while the MC only simulates a monoenergetic beam, and, also due to high temperature variations during the testbeam data taking. Thus, since the energy reconstruction is at first order proportional to the total charge deposit, any variations between data and MC for the total charge deposit (noise etc), would have an impact on the reconstructed energy.

Finally, the reconstructed energy over the testbeam momentum is shown in Figure 7.8.

Momentum (GeV/c)	MC Electrons	Reconstruction Efficiency (%)
0.3	13733	98.1
0.4	13743	98.2
0.5	13711	97.9
0.6	27430	98.0
0.7	13701	97.9
0.8	13675	97.7
0.9	13652	97.5
1.0	13664	97.6
1.2	6792	97.0
1.4	6754	96.4
1.6	6705	95.8
1.8	6691	95.6
2.0	6633	94.8
2.4	6617	94.5
2.8	6488	92.7
3.0	6482	92.6
3.2	6459	92.3
4.0	6251	89.3

Table 7.2: Number of MC electrons at 30 degrees in the DsECal.

Momentum (GeV/c)	Data Mean (GeV)	MC Mean (GeV)
0.7	0.72	0.70
0.8	0.81	0.80
0.9	0.89	0.90
1.0	1.00	1.00
1.2	1.22	1.20
1.4	1.41	1.40
1.6	1.63	1.60
1.8	1.81	1.80
2.0	1.98	1.99

Table 7.3: Reconstructed energy for the DsECal testbeam in the momentum range 0.7-2.0 GeV/c.

The plot shows all momenta below 2 GeV/c after all the corrections have been applied.

7.1 Validation of the Kalman filter PID using the DsECal testbeam

The validation of the Kalman filter PID described in section 6.4 is done using the DsECal testbeam. Since the Kalman filter can follow the trajectory of a track or shower crossing the ECal on a hit by hit basis it makes it a powerful PID tool. First, the base seed state of

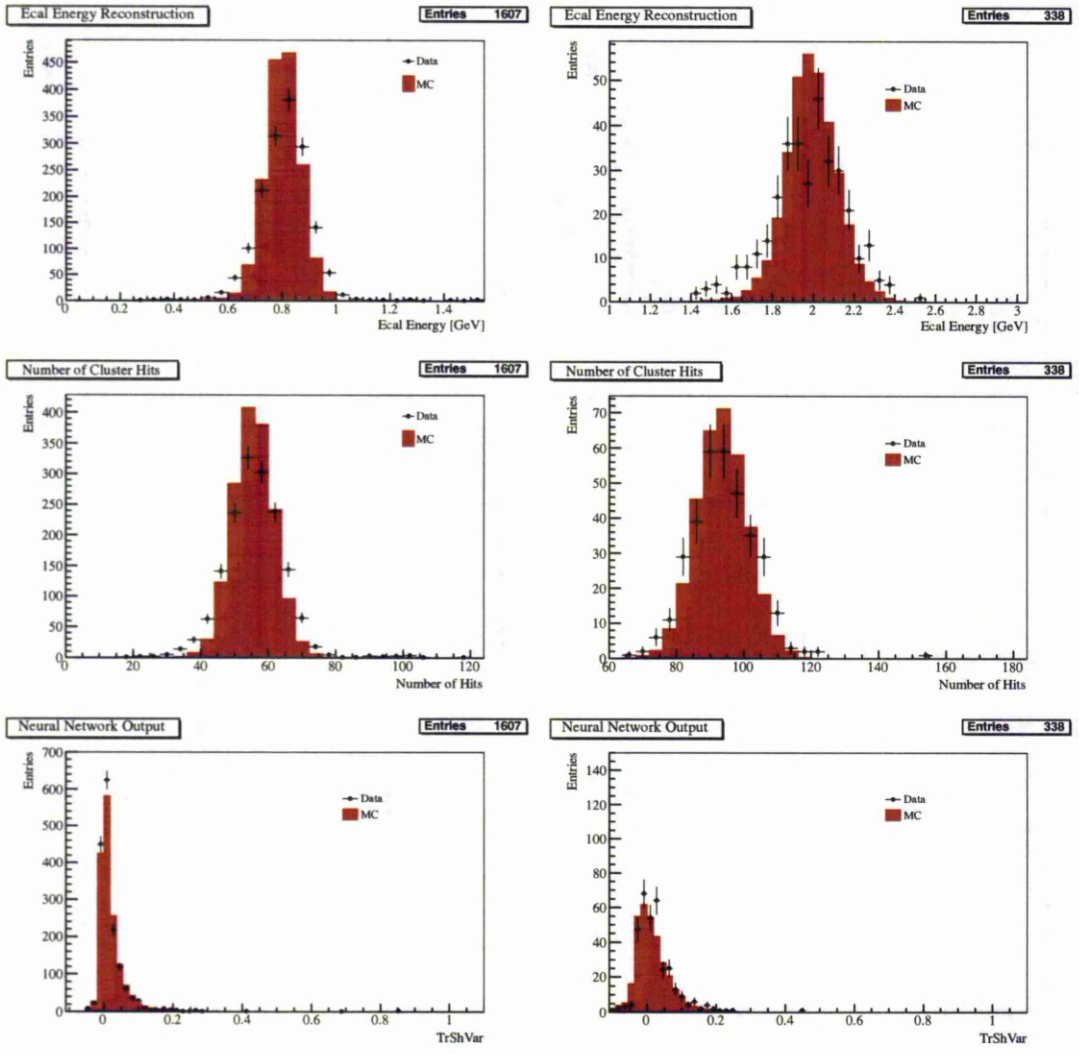

Figure 7.4: The reconstructed ECal energy (top), the number of cluster hits (middle) and the track-shower discrimination variable (bottom) for 0.8 GeV/c (left) and 2 GeV/c (right) testbeam momenta. All plots are normalized by area.

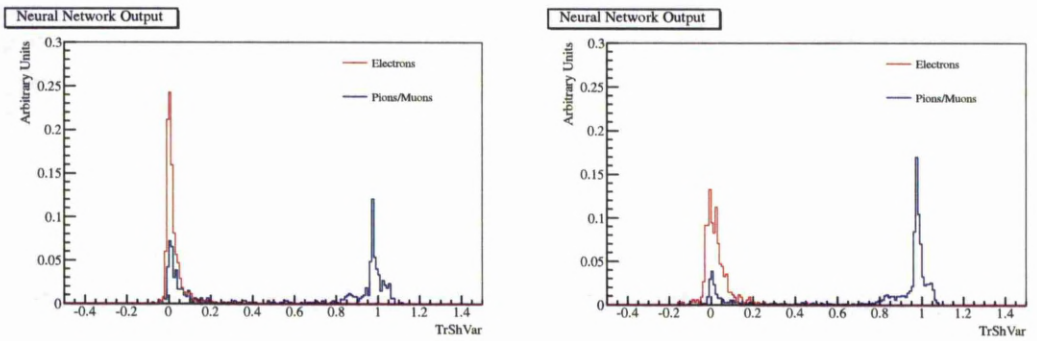

Figure 7.5: The performance for the ECal PID, track-shower discrimination variable, for 0.8 GeV/c (left) and 2 GeV/c (right) testbeam momenta.

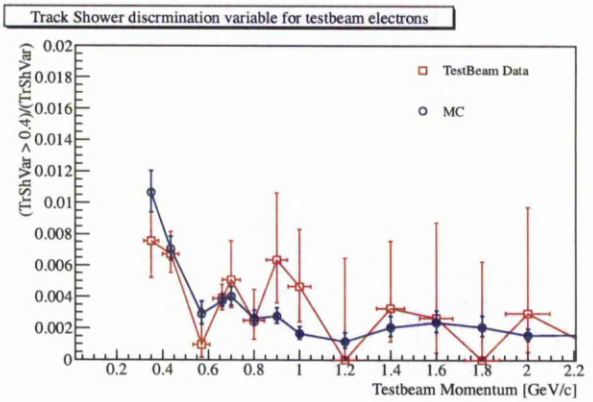

Figure 7.6: The electron mis-identification probability from the DsECal testbeam.

the track or shower is found using the simple fitter from the ECal reconstruction algorithm. Then each layer is scanned for reconstructed cluster hits and if a hit is found it is then fit to the previous state of the track or shower. If the fit is successful the hit is added to the existing track or shower creating a new seed state. The hit filter stops if two continuous layers with more than two hits are found or if two continuous layers with no hits are found or if the hit filter fails continuously twice or if the track exits or stops in the ECal. The number of filtered hits and the layer the hit filter stopped in are compared with the total cluster hits and to the last cluster layer. Two parameters are then defined. The Kalman

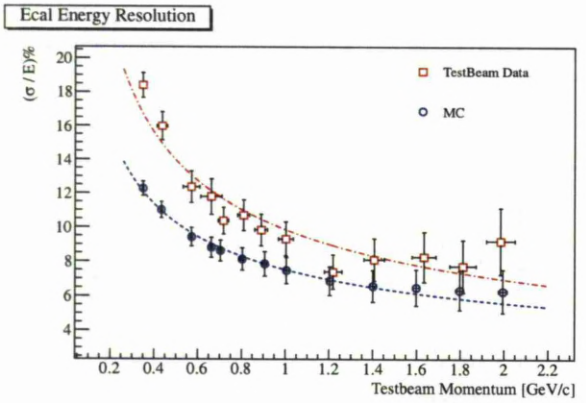

Figure 7.7: The ECal energy resolution from the DsECal testbeam. The error bars on the Y-axis is the standard deviation from the Gaussian fit. The error bars on the beam momentum is the difference between the nominal and fit momentum.

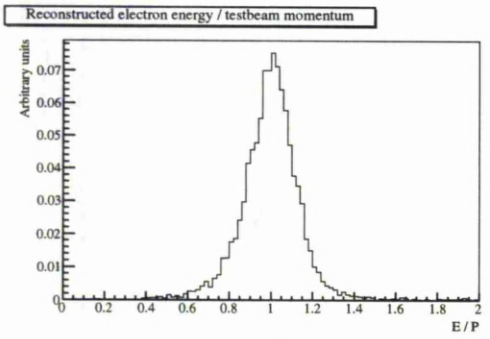

Figure 7.8: E/P for 30 degrees testbeam electrons for all momenta below 2 GeV/c.

filter parameter, KF Parameter,

$$\text{KF Parameter} = \frac{\text{layer the hit filter stopped in}}{\text{last cluster layer}}, \tag{7.5}$$

and the Kalman filter nodes parameter, KF Nodes Parameter,

$$\text{KF Nodes Parameter} = \frac{\text{number of hits filtered}}{\text{all cluster hits}}. \tag{7.6}$$

Also the total number of hits successfully filtered and the worst χ^2 from all the filtered hits are stored.

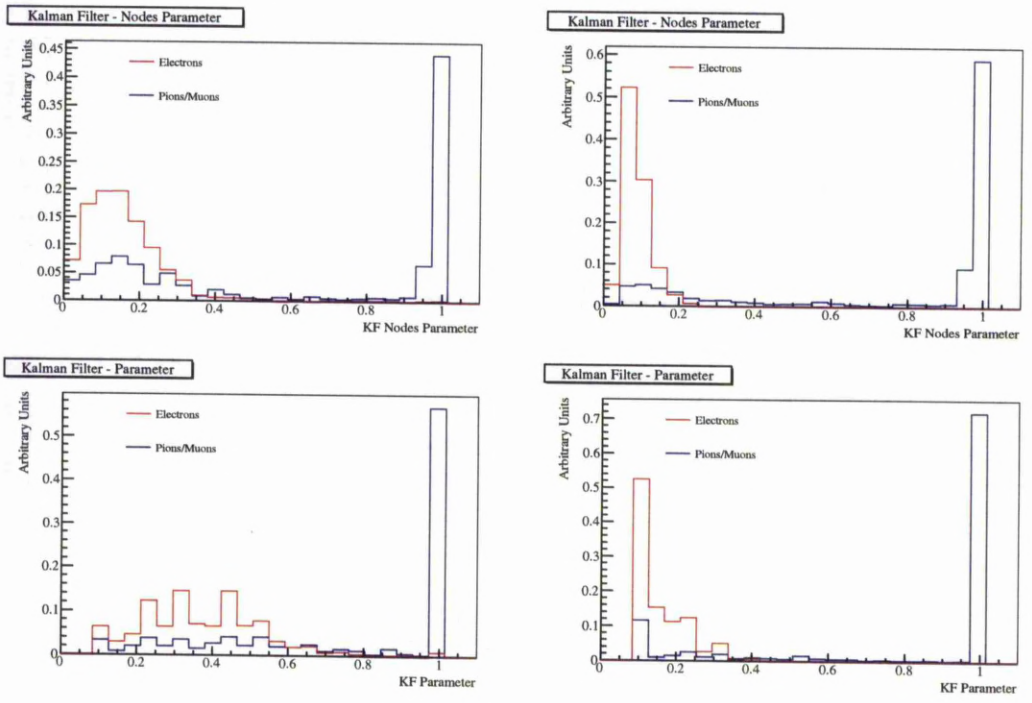

Figure 7.9: The KF Nodes Parameter (top) and the KF Parameter (bottom) for the testbeam at 0.8 GeV/c (left) and 2 GeV/c (right) at 30 degrees.

For MIPs, since they deposit only one hit per layer until they stop or escape the ECal, both Kalman filter parameters are expected to be close to one. For showers on the other hand the Kalman filter parameters are expected to be close to zero. A separation between electrons and pions is also possible, since usually a pion will travel some distance in the ECal before it starts showering. A comparison between electrons and pions/muons from the DsECal testbeam for 0.8 GeV/c and 2 GeV/c at 30 degrees is shown in Figure 7.9. A comparison between data and MC for the Kalman filter parameters for the same momenta is shown in Figure 7.10. Finally, a comparison between the Kalman filter PID and the neural network output for testbeam electrons and pions/muons for the momenta mentioned above is displayed in Figure 7.11. The performance of the Kalman filter PID is strongly dependent on the ECal noise level. Particularly noisy events will tend to return lower values for the Kalman filter parameters. From these plots it is possible to easily separate between a track and a shower and also to make a separation between EM shower and hadronic shower.

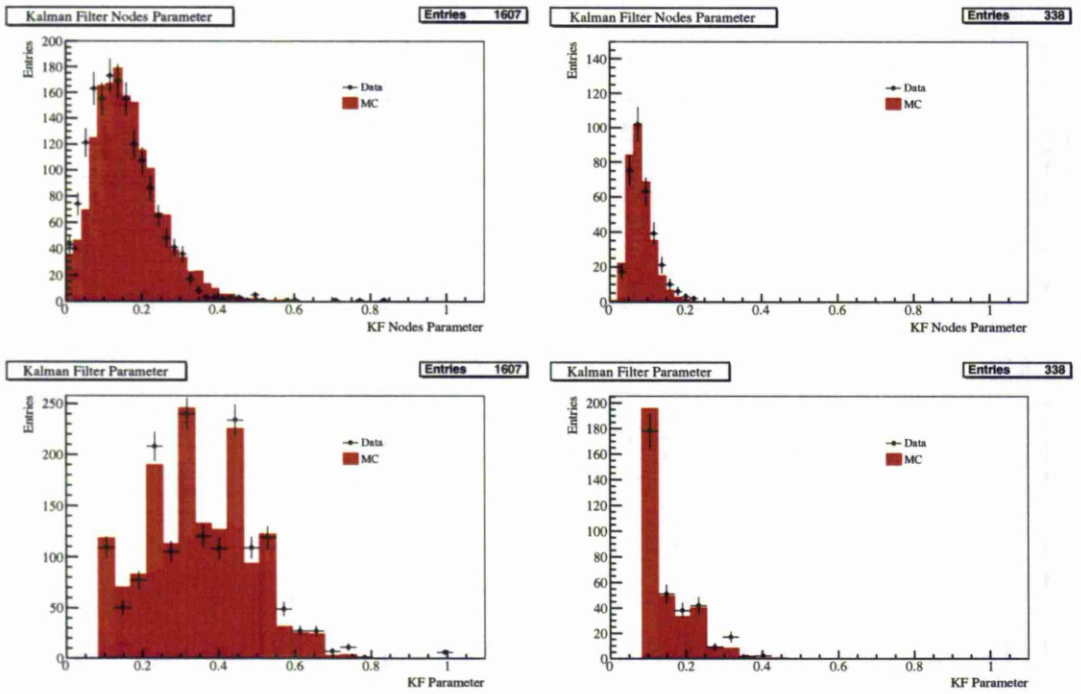

Figure 7.10: The KF Nodes Parameter (top) and the KF Parameter (bottom) for testbeam electrons at 0.8 GeV/c (left) and 2 GeV/c (right) at 30 degrees.

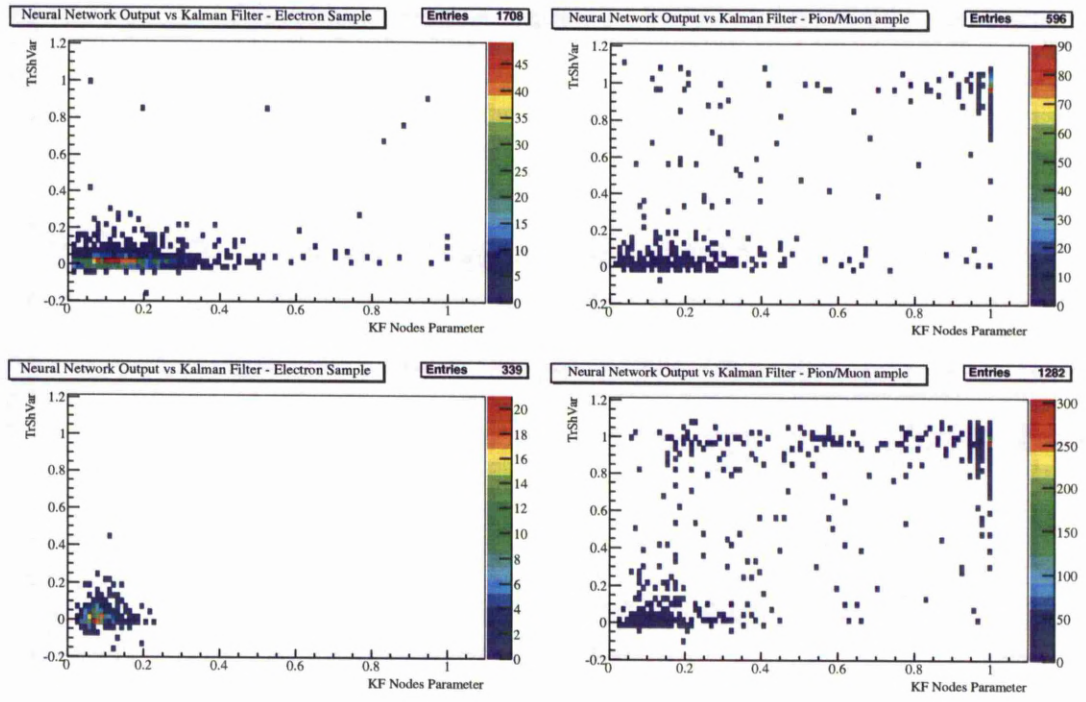

Figure 7.11: The KF Nodes Parameter for electrons (left) and pions/muons (right) compared with the neural network output for testbeam electrons at 0.8 GeV/c (top) and 2 GeV/c (bottom) at 30 degrees.

Chapter 8

Electron neutrino selection using the tracker detectors and the ECals at ND280

The measurement of the $\nu_\mu \rightarrow \nu_e$ oscillation signal, which is the main goal of the T2K experiment, is affected by two main background sources. The first is the intrinsic ν_e beam contamination and the second is the NC π^0 where the π^0 can mimic the electron signal in Super-Kamiokande. The measurement of these two background channels is particularly important and the near detector is crucial to understand them.

The electron neutrino spectrum is produced by kaon and muon decays. These muons and kaons are produced when the proton beam is smashed into the graphite target. Kaons can decay to electron neutrinos through the lepton decay channels, $K^+ \rightarrow \pi^0 + e^+ + \nu_e$ and $K^0_L \rightarrow \pi^\pm + e^\pm + \nu_e(\bar{\nu}_e)$. Muons are produced from decayed pions and decay to electron neutrinos through $\mu^+ \rightarrow e^+ + \bar{\nu}_\mu + \nu_e$. Together these combinations form the ν_e spectrum. The electron neutrinos from kaon decay are in general more energetic than those from muon decay and populate the high energy tail of the neutrino energy spectrum. The off-axis construction produce a narrow band ν_μ beam. The same does not occur with ν_e production due to 3-body decays, resulting in a broader ν_e spectrum.

The data collection at the near detector, ND280, had been separated into two main periods: Run-I from January to June of 2010 and Run-II from November of 2010 to March of 2011. The main differences of the two run periods is the absence of the barrel ECal modules surrounding the tracker area for Run-I and the increase of the number of bunches from 6 to 8 for Run-II. The beam power is also much higher for Run-II resulting in higher

number of delivered proton on target (POT).

The analysis searches for charged current (CC) electron neutrino interactions with a vertex point inside the FGD fiducial volume (FV) and the time inside one of the 6 or 8 bunches. The presence of the magnetic field will help to distinguish between positive and negative charge particles and thus help to select electrons rather than positrons. The TPCs and the ECals are responsible for the particle identification (PID).

The electron selection is challenging for two reasons. The first is the small number of electrons produced from a CC ν_e interaction, compared to the large fraction of muons from ν_μ interactions (see Table 8.1). Adding also the pion and the proton contamination, the PID must work extremely well to obtain a pure electron selection. The second reason is the huge number of background electrons coming from other sources such as π^0. Decay products (stopping muons etc) and δ electrons can further increase the electron background contamination. Rejection and estimation of background electrons is important for the measurement of the ν_e beam contamination.

8.1 Datasets and Monte Carlo (MC)

The total POT selected for Run-I and Run-II is 1.39×10^{20}. After the detector and beam data quality (DQ) cuts (see section 8.2) the total POT at ND280 is reduced to 1.068×10^{20}. Run-I consists of four beam-runs 31-34, delivering in total 0.297×10^{20} POT after DQ. Run-II consists of three beam-runs 36-38, delivering in total 0.771×10^{20} POT after DQ.

The MC sample used for the analysis is 16.33×10^{20} POT; 4.56×10^{20} POT simulates Run-I and 11.77×10^{20} POT simulates Run-II. The neutrino interaction breakdown in the FGDs as simulated from the GENIE neutrino generator is displayed on Table 8.1.

During data taking the beam power is continuously changing. For Run-I, the beam power was in the range 20-90 kW, while for Run-II it was up to 145 kW. For the MC the beam power is constant at 100 kW. The difference in the beam power between data and MC could result in some differences in the background estimation for the event selection.

The data/MC ratio is approximately the same for both Run-I and Run-II:

$$(\text{Data/MC})_{\text{POT}} = 0.065. \tag{8.1}$$

Neutrino	Fraction (%)	CC (%)	NC (%)
ν_μ	95.3	71.2	28.8
$\bar{\nu}_\mu$	2.8	67.3	32.7
ν_e	1.7	72.7	27.3
$\bar{\nu}_e$	0.2	69.0	31.0

Table 8.1: The neutrino interactions in the two FGDs simulated from the GENIE MC.

8.2 Data Quality (DQ)

Good data selection is essential for the analysis. The DQ is separated into two main parts, the selection of good beam spills and the detector performance. The performance of the sub-detectors and the magnet are continuously checked during data taking.

8.2.1 Good beam spill selection

The neutrino beam is produced in spills of six or eight bunches as described in section 3.1. Good beam spills are selected if they are marked as "physics run" and all horns are on. The "Beam Trigger" flag must be on to make sure the beam exists during the main ring (MR) operation and also to check the two GPS times; $|$ GPS1-GPS2 $| < 200$ ns. To exclude spills with no beam in the MR, the number of protons per spill should be $> 1 \times 10^{11}$. The current of all horns is checked to be stable at 253 ± 5 kA. The muon monitor is used to check the beam size and the beam angle is within 1 mrad precision.

8.2.2 ND280 Data Quality

Beam spills flagged as good are checked for the sub-detector and magnet performance and stability.

The magnet was operated with a current of 2.6 kA or 2.7 kA for Run-I and 2.9 kA for Run-II. The magnet current was checked on a 10 minute basis for both Run-I and Run-II. The periods with current < 2.55 kA are not selected.

For the TPC, the data quality flags are identified by checking for electronic low voltage, MicroMegas and cathode high voltage, and the gas mixture status (temperature and pressure). Further monitor studies are performed checking the TPC dE/dx, the latency, pedestal and MicroMegas spark checking.

The FGD DQ flags are determined by checking the beam timing, cosmics, the beam and

Beam-Run	Run period	POT delivered (10^{19})	POT after DQ (10^{19})
31	18/03/2010-25/03/2010	0.195	0.156
32	13/04/2010-01/05/2010	0.762	0.746
33	07/05/2010-01/06/2010	1.180	1.172
34	07/06/2010-28/06/2010	0.909	0.897
Run-I	18/03/2010-28/06/2010	3.05	2.97
36	18/11/2010-25/12/2010	4.03	1.288
37	18/01/2011-28/02/2011	5.56	5.176
38	04/03/2011-12/03/2011	1.26	1.245
Run-II	14/11/2010-12/03/2011	10.85	7.71
Run-I+Run-II	18/03/2010-12/03/2011	13.90	10.68

Table 8.2: Protons on target selected after detector data quality (DQ) cuts.

cosmic trigger to check for dark noise, the neutrino event rate and the vertex distributions.

For the ECal, the DQ flags are reported by checking the global slow control (temperatures, voltages and cooling water flow) and performing raw data analysis (dead channels, gain and pedestal monitoring, beam timing, Trip-t occupancy).

More details about the DQ flags, including the POD and SMRD, can be found in [115, 116]. Table 8.2 summarizes the total POT selected after good DQ selection.

8.3 ND280 bunch structure

The beam structure consists of six (Run-I) or eight (Run-II) bunches per spill. The time stamp from all the possible reconstructed vertices is shown in Figure 8.1. A delay of the ND280 trigger caused the double peak structure for Run-II data, which is visible from this plot. The delay was introduced in order to move the bunch time to the center of the Trip-t integration cycle for the BrECals. Thus, the bunch structure has 3 different time periods and each of the periods is treated separately. These periods are: period-I for Beam-Runs 31-34, period-II for Beam-Run 36 and period-III for Beam-Runs 37-38.

The reconstructed vertex candidate has to be inside of one of the characteristic bunches. Thus, each of the bunches is fitted with a Gaussian distribution (Figure 8.2) and the vertex candidate is selected if it is within four sigma from the mean value. Tables 8.3, 8.4, 8.5 summarize the details of the data bunch structure. The mean bunch difference is approximately 582 ns for both data and MC as expected. The bunch width increases in data due

Bunch number	Mean Time (ns)	σ	Mean bunch difference(ns)
1	2839.8	14.67	-
2	3422.8	15.89	583.0
3	4006.1	15.75	583.3
4	4588.9	15.90	582.8
5	5170.8	15.79	581.9
6	5753.6	16.84	582.8
Mean			582.6

Table 8.3: Bunch structure for Run-I (Runs 31-34).

to the beam power increase. For the MC, the same procedure as with data is followed and Table 8.6 summarises the MC bunch structure.

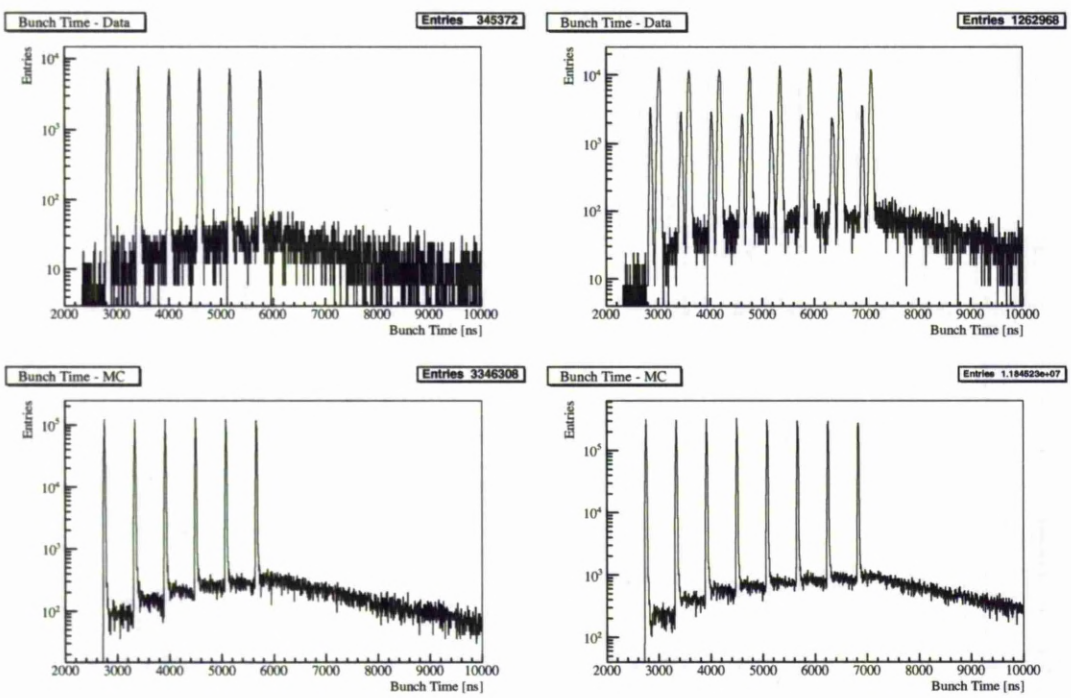

Figure 8.1: Bunch structure for data (top) and MC (bottom) for Run-I (left) and Run-II (right). The two characteristic time bunches for Beam-Run 36 and Beam-Runs 37-38 is also visible corresponding to a delay of the ND280 trigger.

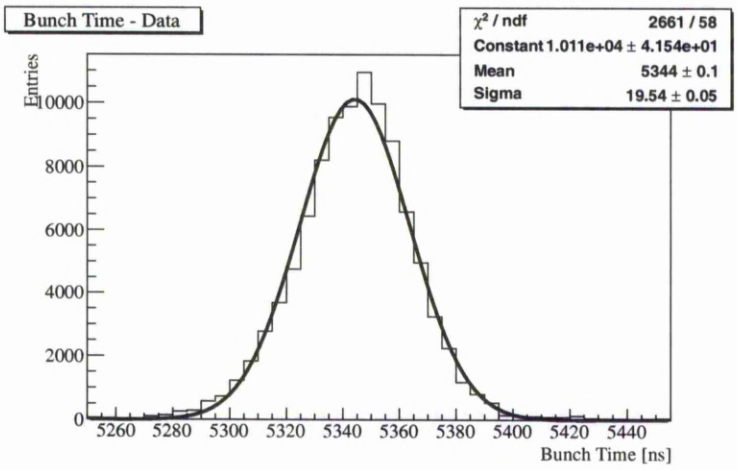

Figure 8.2: An example of a Gaussian fit in one of the data bunches. This is from Beam-Run 37, bunch 5. Similar for all the other bunches for all data Runs and MC.

Bunch number	Mean Time (ns)	σ	Mean bunch difference(ns)
1	2855.0	15.75	-
2	3444.5	18.27	589.5
3	4026.9	18.76	582.4
4	4614.4	20.48	587.5
5	5178.0	21.24	563.6
6	5767.1	20.23	589.1
7	6349.7	21.74	583.6
8	6924.0	16.68	574.3
Mean			581.4

Table 8.4: Bunch structure for Run 36.

Bunch number	Mean Time (ns)	σ	Mean bunch difference(ns)
1	3017.3	20.37	-
2	3596.9	21.35	579.6
3	4181.1	21.63	584.2
4	4764.6	20.56	583.5
5	5345.6	20.83	581.0
6	5925.0	22.11	579.4
7	6506.8	21.87	581.8
8	7092.6	21.89	583.8
Mean			581.9

Table 8.5: Bunch structure for Runs 37-38.

Bunch number	Mean Time (ns)	σ	Mean bunch difference(ns)
1	2757.0	11.29	-
2	3339.3	10.90	582.3
3	3921.4	11.30	582.1
4	4503.4	11.65	582.0
5	5084.8	12.30	581.4
6	5666.5	12.44	581.7
7	6249.4	13.85	582.9
8	6831.1	13.60	581.7
Mean			582.0

Table 8.6: Bunch structure for the MC. First 6 bunches are used for Run-I simulation and all 8 bunches are used for Run-II simulation.

8.4 Vertex reconstruction

A Kalman filter approach is used to estimate the vertex position from a neutrino interaction in the FGD, as described in section 6.5. A detailed description of the algorithm and the validation can be found in [113]. If a primary vertex is reconstructed, a search is performed in a radius of 5 cm around the vertex position. If any good quality tracks are found inside this radius, they are then stored in a container. The search for the most energetic negative track is then done with the tracks stored in the container. This way any broken tracks, or tracks far away from the vertex point are not selected. In the case that more than one primary vertex is reconstructed, the highest momentum track's reconstructed front position is assumed to be the vertex position.

Although the reconstruction efficiency of the vertex algorithm is on the order of 90 %, if no vertex is reconstructed but there is at least one good reconstructed track in a TPC, the event is not rejected. In this case the most energetic track from all the tracks is selected, and its front position is assumed to be the vertex position. The vertex reconstruction efficiency and the difference between the true and reconstructed position is studied using the MC and are demonstrated in Figure 8.3.

8.5 FGD fiducial volume

In order to reduce the background coming from outside the FGDs, only events reconstructed inside the FGD fiducial volume (FV) are considered. The FV area is defined

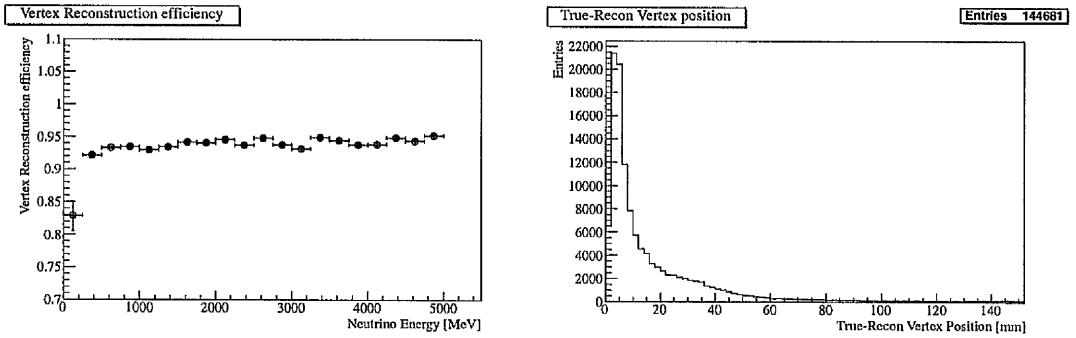

Figure 8.3: The vertex reconstruction efficiency (left) and the difference between the reconstructed and true vertex position (right).

leaving 100 mm of the x-y edges from the FGDs and 7.4 mm from the beginning of each FGD along the z-direction. A detailed study of the selection of FV is performed in [117]. The FV cuts in the detector coordinates are

- X: -832.17 $\rightarrow$ 832.17 mm
- Y: -777.17 $\rightarrow$ 887.17 mm
- Z: 123.35 $\rightarrow$ 447.05 mm (FGD1), 1481.35 $\rightarrow$ 1807.05 mm (FGD2)

8.6 Charge reconstruction

The trajectory of a track is fitted with a helix and the bend is defined as the curvature. The charge of a track is reconstructed in a single TPC. For tracks going into two FGDs, the time of flight between them is assumed and if the track direction is inverted then the charge is also inverted. For long tracks the Kalman filter is used to do the matching between the detectors and the addition of other detectors could invert the charge curvature. Multiple scattering is also an effect that could compromise the charge reconstruction. Finally, the effect of the magnetic field on very high momentum tracks is small, leading to an incorrect calculation of the curvature.

8.7 Electron Selection overview

The electron selection is based on the selection of the most energetic track among all negative tracks. The selected track must be inside one of the 6 or 8 bunches and has an associated

reconstructed vertex with a reconstructed position in the fiducial FGD volume. A minimum of 36 TPC hits is required for good quality TPC track selection. The most energetic negative track surviving these cuts is then filtered through the TPC and ECal PID. The TPC PID measures the energy loss of a particle traveling through the TPC comparing with the expected energy loss for a particle hypothesis. The ECal PID uses a neural network to separate between a track and shower. For the electron selection, only tracks that agree with the electron hypothesis in the TPC are selected. In addition, if the track goes into the ECal then it must be reconstructed as a shower as well, otherwise further TPC PID cuts are applied. In terms of PID application the analysis is separated into three main categories:

- **Case 1:** The selected most energetic track does not enter the ECal or enters the ECal near the edges or has momentum $p < 250$ MeV/c. In these cases only the TPC PID is applied.

- **Case 2:** The selected most energetic track goes into the DsECal far away from the edges and with $p > 250$ MeV/c.

- **Case 3:** The selected most energetic track goes into the BrECal far away from the edges and with $p > 250$ MeV/c (only for Run II data).

The momentum threshold at 250 MeV/c for applying the ECal PID has been studied through the MC and also using through-going muons (i.e. muons passing through the 3 TPCs and going into the DsECal and filtered to agree with the muon hypothesis in all 3 TPCs) and studying the performance and the muon mis-identification probability of the ECal PID. This study is performed in section 8.13. In general, the ECal PID is not reliable below this momentum threshold.

Also, the ECal PID is not applied if a track enters the ECal near the edges, that is the cluster reconstructed position must be in the front of the ECal and $|x|, |y| < 850$ mm. Energy leakage and too few reconstructed hits make the energy reconstruction and the ECal PID unreliable. In these cases only the TPC PID is applied.

At the time this analysis was performed, a number of reconstruction and calibration issues did not allow the inclusion of the BrECal in the analysis. However, the flexible

analysis structure allows to repeat the electron selection in the near future, when the reconstruction and calibration issues are resolved including the BrECal. As it will be shown in the next sections the combination of the TPC and ECal is the most powerful for the PID.

After the application of the TPC and ECal PID, the effort is continued in order to remove the background contamination. The muon background is almost eliminated, but further cuts are required to remove background electrons. Electrons from photons are rejected and also activity outside the tracker and ECal region is a possible sign of background; POD activity is studied in detail and events found with activity in the POD are rejected.

Finally, the kinematics and the angular reconstruction are studied. Tracks at high angles are rejected since it is most probable that these tracks come from a photon. In general it is expected that electrons from a CC ν_e interaction will propagate mostly in the forward direction. However, electrons from π^0 or from photons, either inside or outside the tracker detectors, should propagate in a random direction. Also a cut on the neutrino energy, reconstructed under the CCQE assumption, is applied in order to remove the low momentum background, while the total number of reconstructed tracks is also checked.

In general, the data has much more activity than expected from the MC. This could be due to various reasons. First, as already mentioned the beam power for the data varies, while it is kept constant in the MC. Secondly, the MC does not simulate sand muons; these are muons created outside the detector but penetrate through the detector. As a result, δ-electrons are not simulated as well and their population might be different than expected. Other things, like noise, cosmics, under-estimation of the π^0 number and detector matching differences between data and MC can also lead to a discrepancy between data and MC.

8.8 DsECal PID

The DsECal PID is based on two parameters for tracks entering the DsECal with momentum above 250 MeV/c and far from the edges of the ECal. The neural network output (called TrShVar) returns zero for a perfect shower and 1 for a perfect track and is used as the main PID tool. The reconstructed energy, E_{rec}, is also used but only for tracks with momentum above 450 MeV/c. A shower is selected only if TrShVar < 0.4 and if $E_{rec} > 400$ MeV when the particle's momentum is more than 450 MeV/c. The selection of

cuts is based on the studies performed using through-going muons (section 8.13) and the ECal testbeam (chapter 7).

The differences between data and MC shown in Figure 8.4, especially on the PID, could be due to different reasons. Run-II was much more noisy than Run-I which could explain the fact that the data-MC difference appear mostly in Run-II. Other reasons like data-MC differences in the angular distribution for tracks entering the DsECal, underestimation or overestimation of the muon tracks going into the ECal and differences in detector matching between data and MC could also contribute.

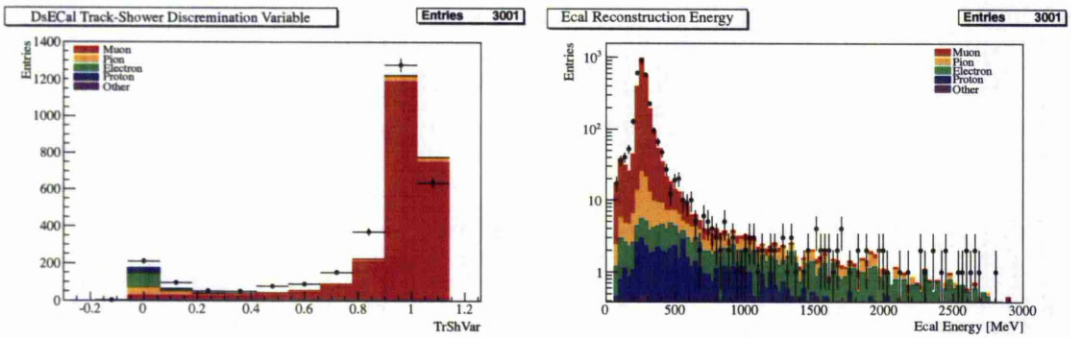

Figure 8.4: The ECal PID for the tracks going in the DsECal and with p > 250 MeV/c. The track-shower discrimination variable (left) shows the output from the neural network and is one for a perfect track and zero for a perfect shower. The ECal energy is reconstructed under the assumption that the incoming particle is either a photon or an electron (right).

8.9 TPC PID

The energy loss in the TPC is estimated using RecPack. The estimation of the energy loss is currently available only for MIPs. For electrons an extra correction based on testbeam data has been applied. The method chosen to describe the energy loss in the TPC is the truncated mean method. The pull for each particle species is then calculated

$$\delta_i = \frac{C_T^{meas} - C_T^{exp}(i)}{\sigma_T}, \tag{8.2}$$

with i = muons, electrons, pions, protons and kaons. The C_T^{exp} has been provided from the testbeam data at TRIUMF.

Ideally, the muon pull should be centralized at zero. However, detector operation inefficiencies may move the mean pull from zero. A calibration factor is then applied to the measured C_T in order to centralize the muon pull at zero. The C_T calibration is performed using muons going through the three TPCs and the DsECal. The ECal PID is used to make sure that true muons are selected. The details of the calculation and the C_T calibration applied per Beam-Run and per TPC can be found in section 8.13.

The correction applied to electrons, centralizes the pull at one. The energy loss of the electrons is overestimated in MC, something which has been also observed during the TPC testbeam data [108]. To fill the gap between data and MC, the data is then shifted to match the MC and the electron pull is centralized to one. The electron pull is centralized to zero by applying a correction factor 0.95 to both data and MC.

The energy loss in the TPC for the most negative energetic track with more than 36 TPC hits and a reconstructed vertex position in the FGD FV is shown in Figure 8.5. A contamination of charge mis-identified protons is also visible. Figure 8.6 shows the muon and electron pull. The difference in the tracker activity between data and MC is visible from this plot.

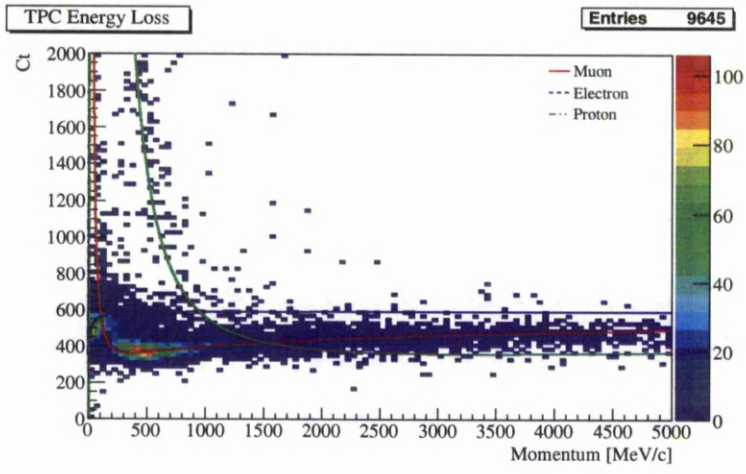

Figure 8.5: The energy loss in the TPC for the most negative energetic track reconstructed in the FGD FV and with more than 36 TPC hits.

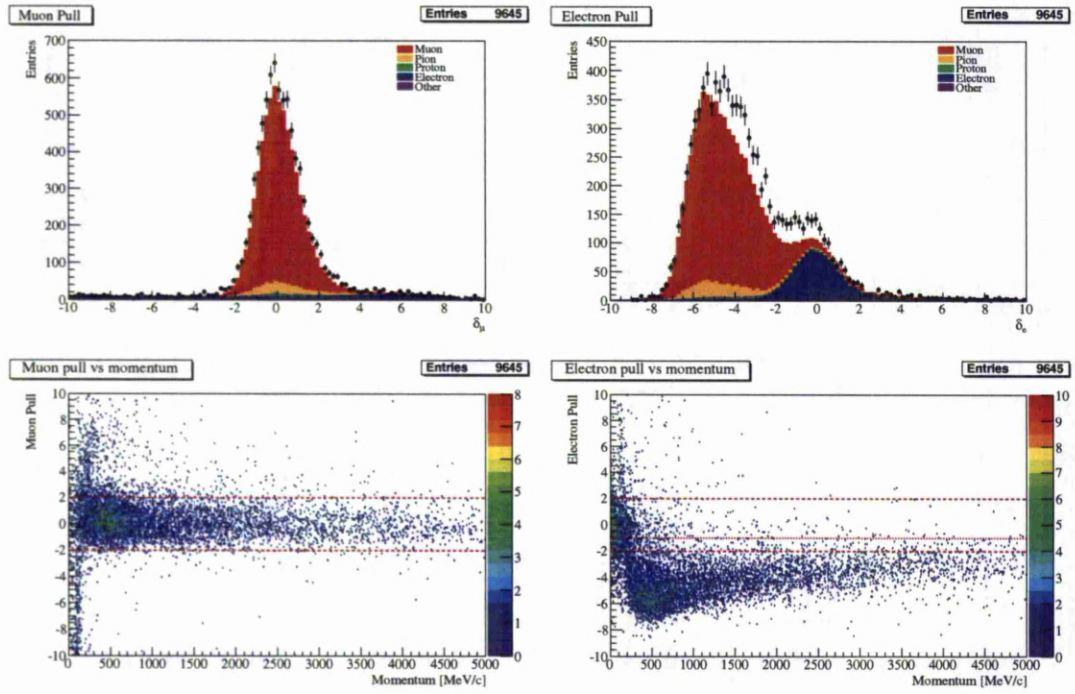

Figure 8.6: The TPC PID. Top plots show the muon (left) and electron pulls (right) for the most energetic negative track selected in the FGD FV. Bottom plots show the muon (left) and electron (right) data pulls with respect to the reconstructed momentum.

8.10 Electron selection from the TPC and ECal PID

An electron candidate is selected if it has a TPC and a DsECal segment and momentum more than 250 MeV/c and if

- $-2 < \delta_e < 2$
- TrShVar < 0.4 and $E_{rec} > 400$ MeV if the particle's momentum is more than 450 MeV/c

or it only has a TPC segment or momentum below 250 MeV/c and if

- $-1 < \delta_e < 2$
- $\delta_\mu > 2$
- $\delta_\pi > 2$

If a track goes into a second TPC then the track is rejected if the electron pull is higher than three and the muon or pion pull is less than two.

A comparison between the TPC and the ECal PID is done using MC for true electrons and muons, Figure 8.7. The TPC pull could agree and with both the electron and muon hypothesis, thus the presence of the ECal is important to improve efficiency and purity.

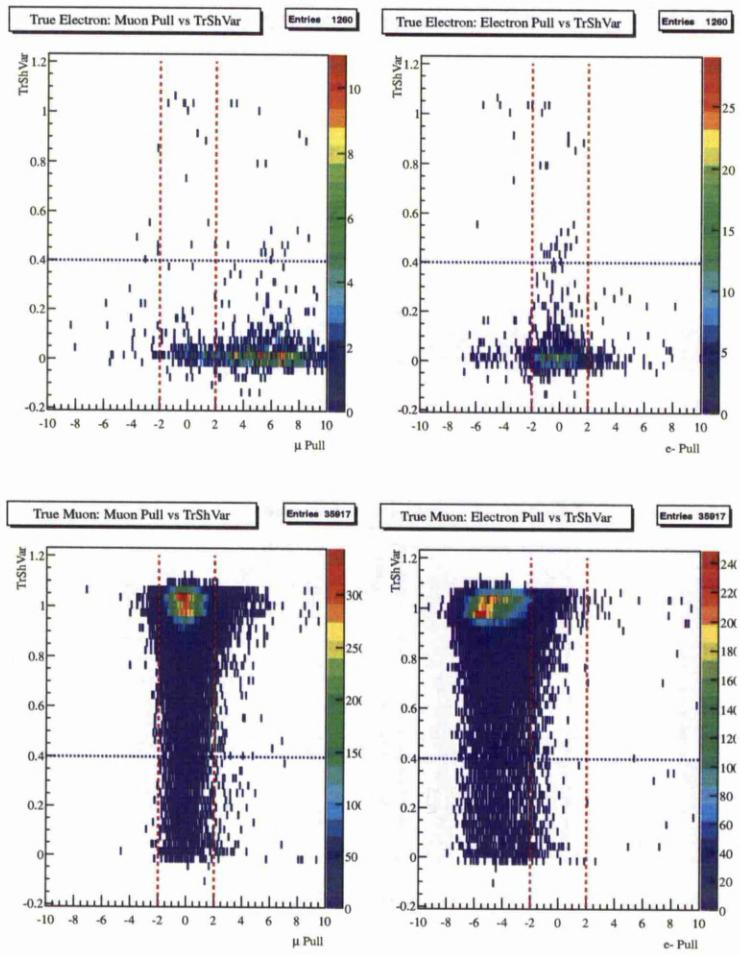

Figure 8.7: A comparison between the TPC and the ECal PID for the most energetic negative track selected in the FGD FV for true MC electrons (top) and true MC muons (bottom).

8.11 Background Rejection

Background rejection is also an important aspect for the ν_e selection. Although the TPC and ECal PID have a significant role to select electrons and reject other particles, the background rejection aims to reject electrons that do not come from a ν_e interaction. The main categories for background rejection, as described in the next part of this section, are: electrons coming from photons, activity in the P0D and kinematic variables from the electron distributions. Figure 8.8 shows the events selected after applying the PID and before applying the background rejection. The low momentum region is populated from the background coming from outside the tracker. At higher momenta the background contribution from CC ν_μ is more significant.

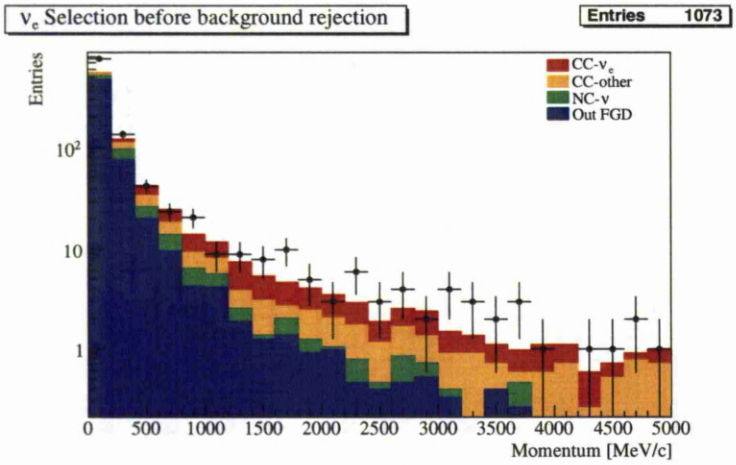

Figure 8.8: Momentum distribution of the selected events after the TPC and ECal PID.

8.11.1 Photon rejection

We reject photon background by looking for e^-e^+ pairs, by comparing our candidate along with other tracks in the event selected. The opening angle and the invariant mass are reconstructed using the XZ direction of the two tracks, which in the local ND280 co-ordinates is the direction where the magnetic field value is zero. In this direction, the angular distribution difference from an electron-positron pair coming from a photon is expected to be almost zero. Thus, the invariant mass is expected to be close to zero. An electron candidate

is assumed to come from a photon if it is matched with another track in a distance less than 5 cm away and has the following properties

- full opening angle, $\cos(\theta) > 0.9$
- opening angle along XZ direction, $\cos(\theta_{XZ}) > 0.94$
- invariant mass, $m_{inv} < 30\ MeV/c^2$.

Events with multiple tracks increase the probability to accidentally select a fake e^-e^+ pair. Thus, the search for photon background is performed only on events with less than five tracks. Events that matched the above properties are displayed in Figure 8.9 and rejected.

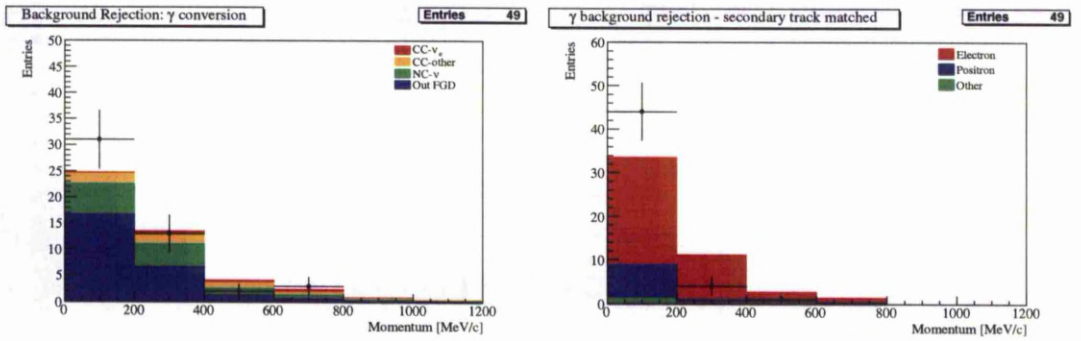

Figure 8.9: Momentum of the events rejected after applying the photon rejection (left) and the momentum of the secondary track matched (right).

8.11.2 Other detector activity

Activity in other parts of the ND280 detector, outside the tracker and inside the same bunch as the selected electron candidate, may provide useful information to reject electron candidates not coming from a ν_e interaction. The analysis searches for activity in the POD. If any reconstructed track is found in the POD, then the event is rejected. Although SMRD could also provide similar information, the activity of SMRD in data is much larger than in the MC. The small number of SMRD hits required to reconstruct an SMRD track (some SMRD modules have as few as two layers) makes it very hard to distinguish between real SMRD tracks and noise. For this analysis the SMRD activity is not considered. Events with POD activity are displayed in Figure 8.10 and rejected.

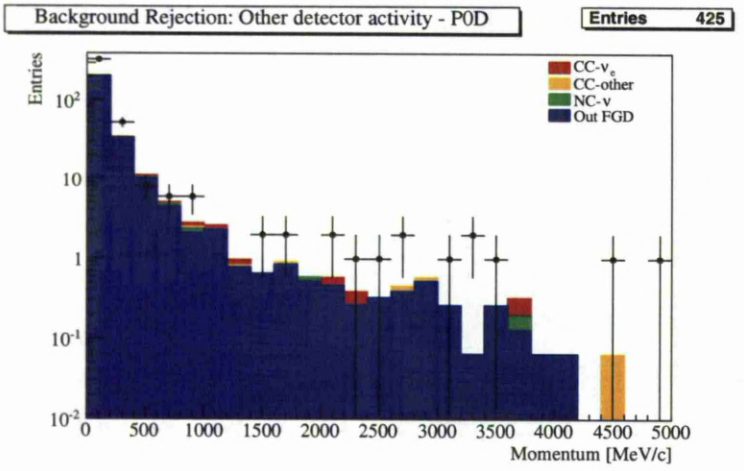

Figure 8.10: Momentum distribution of the events with POD activity.

8.11.3 Angular distribution

Electron candidates coming from a ν_e interaction are mainly propagating in the forward direction. On the other hand, electrons coming from π^0 or photons outside the tracker should propagate in random directions. Thus, a cut on the polar angle of the reconstructed track rejects some of the background electrons with small efficiency loss. If $\cos(\theta) < 0.37$, then the event is rejected (Figure 8.11).

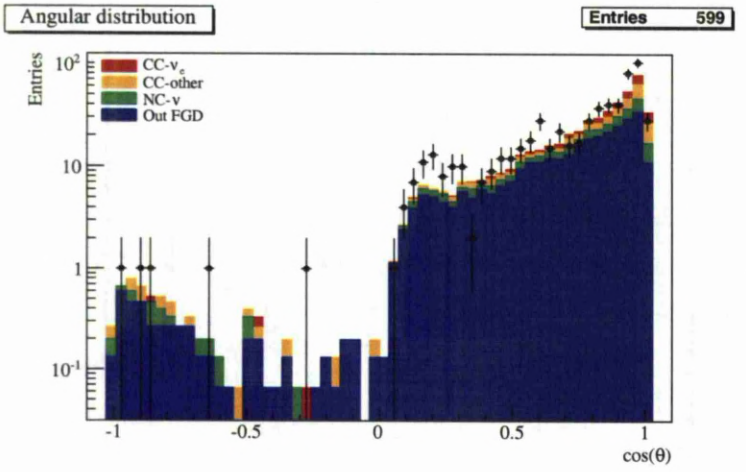

Figure 8.11: A distribution of the polar angle for the selected events.

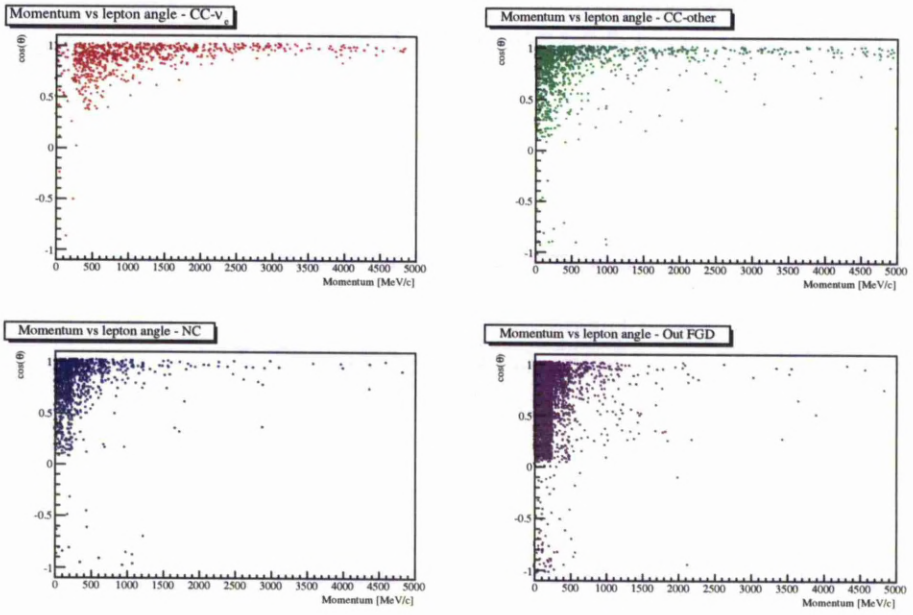

Figure 8.12: The momentum-angle distribution for the selected events. Top left is the CC ν_e, top right is the CC non ν_e, bottom left is the NC and bottom right is the out of FGD events.

8.11.4 Neutrino energy reconstruction

Neglecting the electron mass the reconstructed neutrino energy, E_ν^{rec}, under the CCQE assumption will take the simplified form

$$E_\nu^{rec} = \frac{m_N p_e}{m_N - p_e(1 - \cos\theta)}, \tag{8.3}$$

with m_N the nucleon mass, p_e the electron momentum and $\cos\theta$ the electron angle.

A cut on the the reconstructed neutrino energy would help to reject all the low momentum background plus a few more high momentum background events leaking into the low neutrino energy reconstruction area. Events with $E_\nu^{rec} < 300$ MeV are rejected (Figure 8.13).

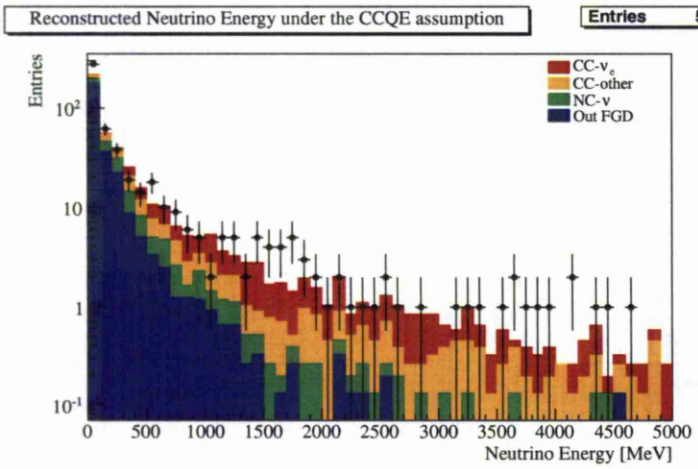

Figure 8.13: The distribution of the reconstructed neutrino energy for the selected events.

8.11.5 Track multiplicity

The final cut on the background rejection is to check for the total number of reconstructed tracks. Events with high track multiplicity are either multi π^0 events, events with a lot of secondaries, tracks coming from outside the tracker or events with multiple broken tracks. All of the cases could result in a bad vertex reconstruction position or the selection of the wrong most energetic track if the tracks are significantly spread. Events with more than nine reconstructed tracks are rejected (Figure 8.14).

8.12 Kinematic properties of the selected electron neutrino candidates

After all the cuts have been applied, 142 ν_e candidates survived. From the MC, 129.8 events were expected, with 11.2 % overall efficiency and 35 % purity. The efficiency is defined as

$$\text{efficiency} = \frac{\text{Signal true CC-}\nu_e\text{ selected}}{\text{All CC-}\nu_e}, \tag{8.4}$$

and the purity

$$\text{purity} = \frac{\text{Signal true CC-}\nu_e\text{ selected}}{\text{Signal and background selected}}. \tag{8.5}$$

The efficiency and purity plots and the data/MC comparison are demonstrated in Figure 8.17. The ratio data/MC is separated into two momentum bins, 0-2 GeV/c and 2-

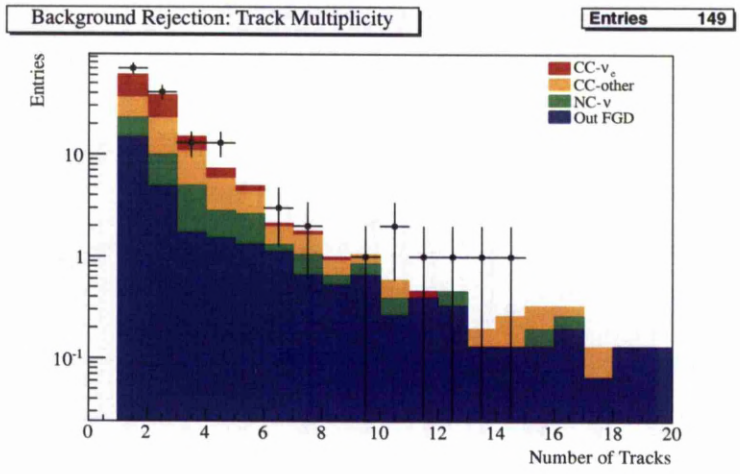

Figure 8.14: The number of reconstructed tracks for the selected events.

5 GeV/c and is shown in Figure 8.16. A small excess of the order of 10 % has been observed for both bins in the data. The electron purity is very good and is above 80 % for momenta less than 1 GeV/c and above 50 % for all momenta.

The Table 8.7 summarises the selection of the ν_e candidates after applying all the selection criteria. More events are selected in FGD2, with a good agreement with the MC. The excess of events in the data is observed only in FGD1.

The momentum of the selected CC ν_e candidates is shown in Figure 8.18. The position of the reconstructed vertex is in Figure 8.19 and the selection in FGD1 and FGD2 in Figure 8.20. The events selected in the TPC+ECal and in the TPC only are shown in Figure 8.21. The combination of the TPC and ECal proved to be a very powerful combination for the electron PID. The neutrino interaction breakdown for the expected ν_e candidates is in Figure 8.22. A selection of event displays for ν_e candidates are shown in Figures 8.23, 8.24 and 8.25. Finally, the events selected per Beam-Run are shown in Table 8.8. The table shows that the excess in the data is only observed in Run-II.

	Data	MC expected	CC-ν_e expected	FOM $S/\sqrt{S+B}$
All CC-ν_e	-	-	408.76	-
1.At least one track in TPC	312995	198493	358.40	3.15
2.Vertex with negative track	52798	30114	114.26	2.57
3.Vertex in FGD FV	11441	9371.26	85.48	3.45
4.TPC Quality	9645	8273.04	83.78	3.60
5.TPC and ECal PID	1073	825.36	52.32	7.12
6.γ rejection	1024	776.38	49.97	7.01
7.P0D activity	599	504.18	48.85	8.51
8.Polar angle	528	449.70	48.33	8.91
9.Neutrino energy	149	134.14	45.65	15.41
10.Track multiplicity	142	129.82	45.58	15.64
FGD1	67	55.0	18.9	-
FGD2	75	74.8	26.7	-

Table 8.7: Summary of the cuts applied for the CC-ν_e selection and the separation between FGD1 and FGD2.

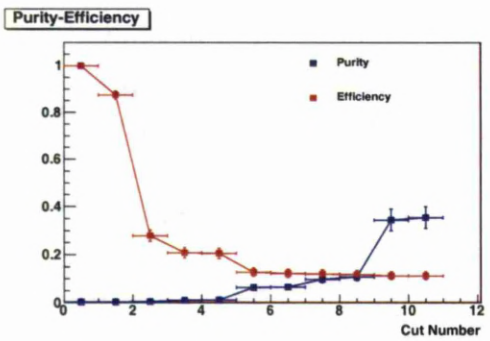

Figure 8.15: Purity and efficiency reduction for the cuts applied. The cut order follows Table 8.7.

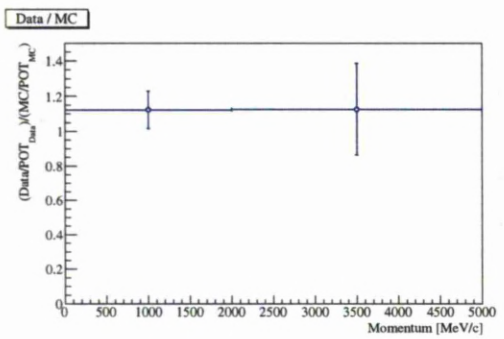

Figure 8.16: The data/MC comparison normalized to protons on target.

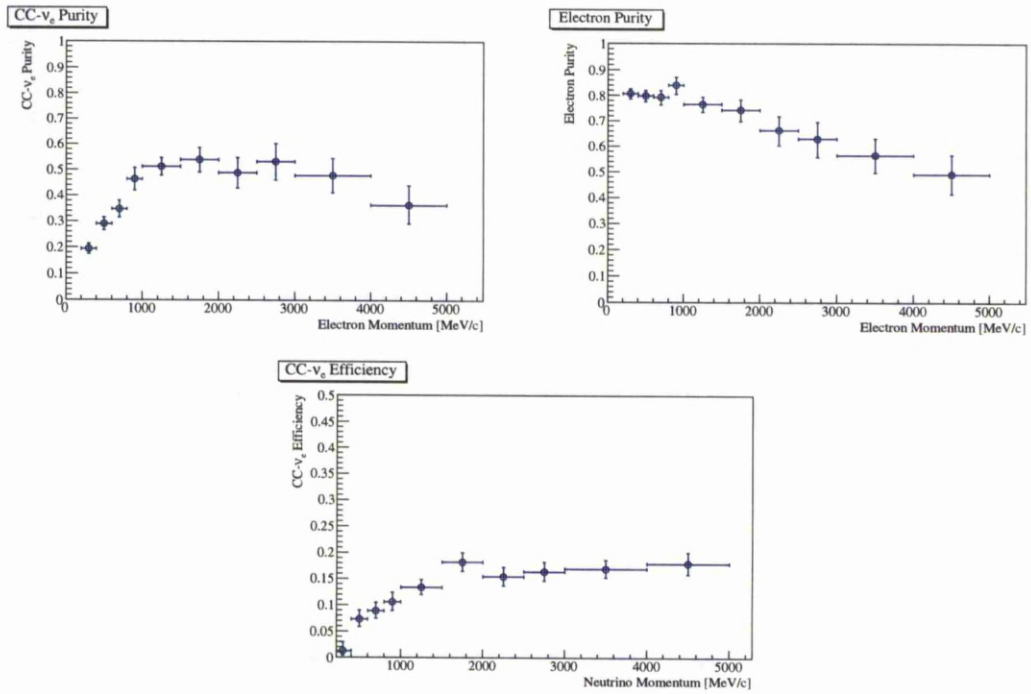

Figure 8.17: The CC ν_e purity (top left) and the electron purity (top right) and the CC ν_e efficiency (bottom).

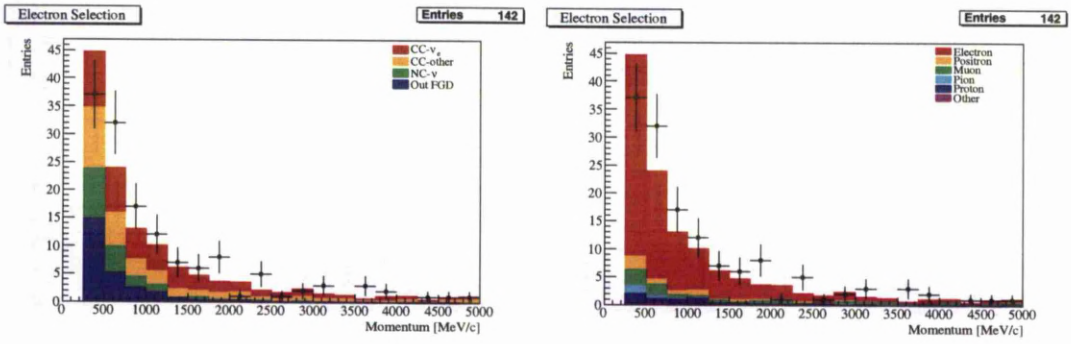

Figure 8.18: The selection of CC ν_e candidates separated to interaction type (left) and particle type (right).

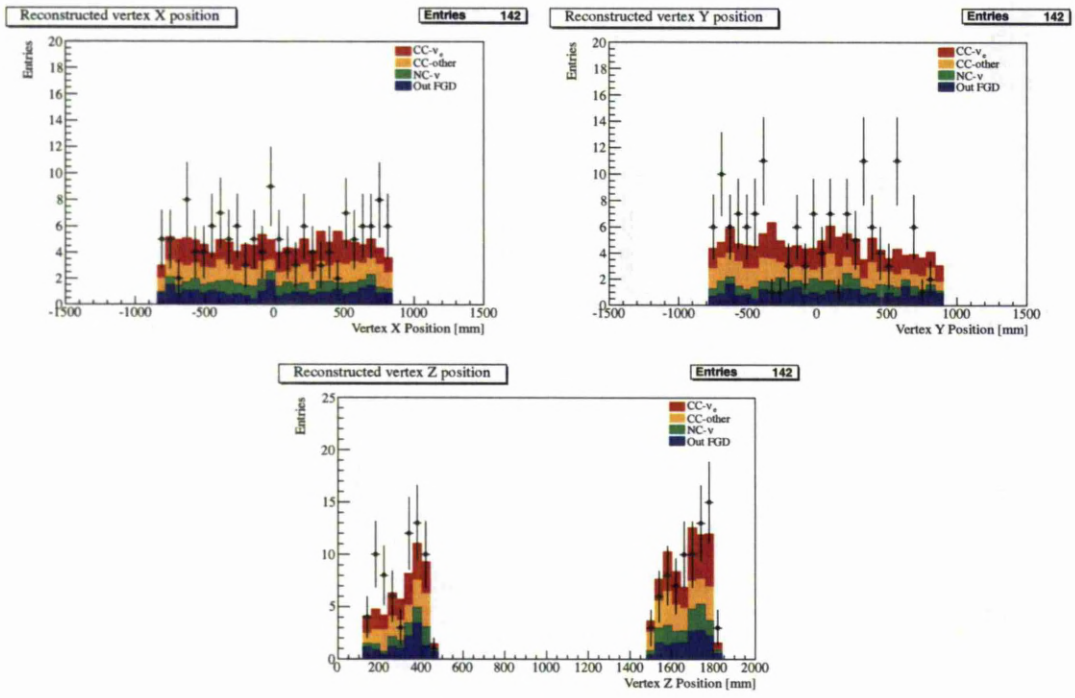

Figure 8.19: The position of the reconstructed vertex for the CC ν_e candidates.

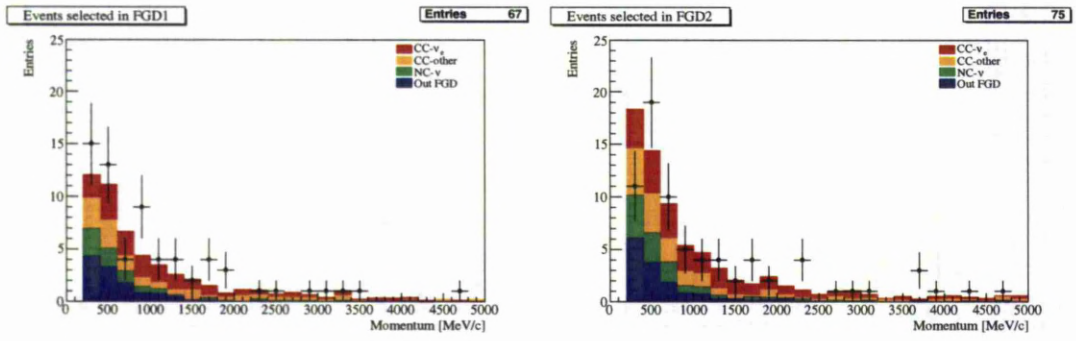

Figure 8.20: Momentum distribution of the events selected in the FGD1 (left) and FGD2 (right).

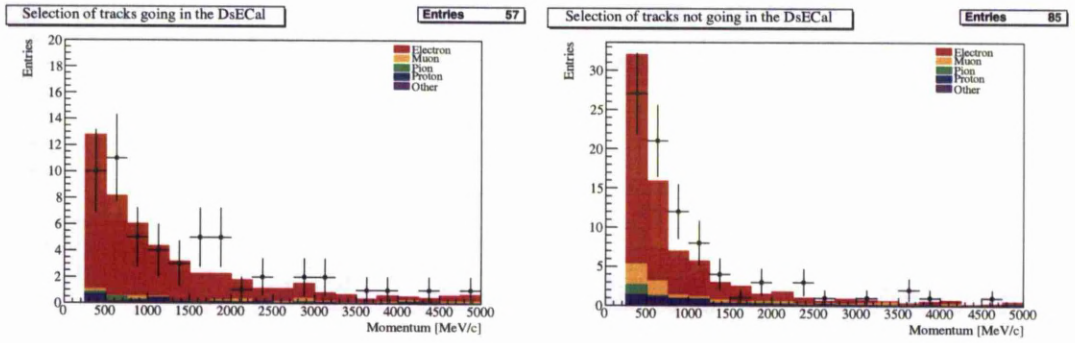

Figure 8.21: Momentum distribution of the events selected in the TPC+ECal (left) and the events selected with TPC only (right).

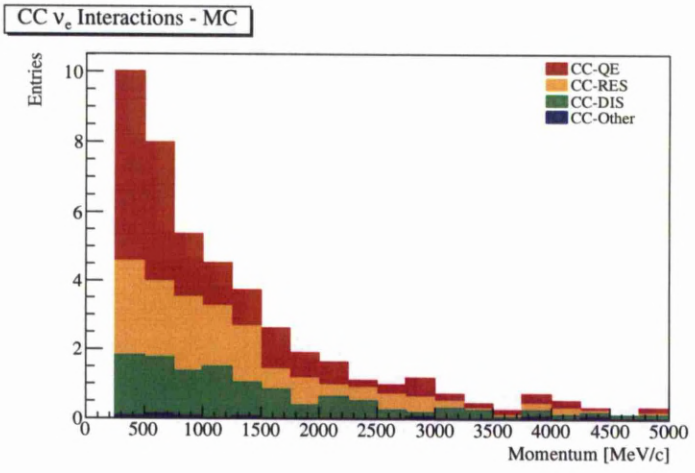

Figure 8.22: The electron momentum distribution for the MC expected ν_e events separated by neutrino interaction type.

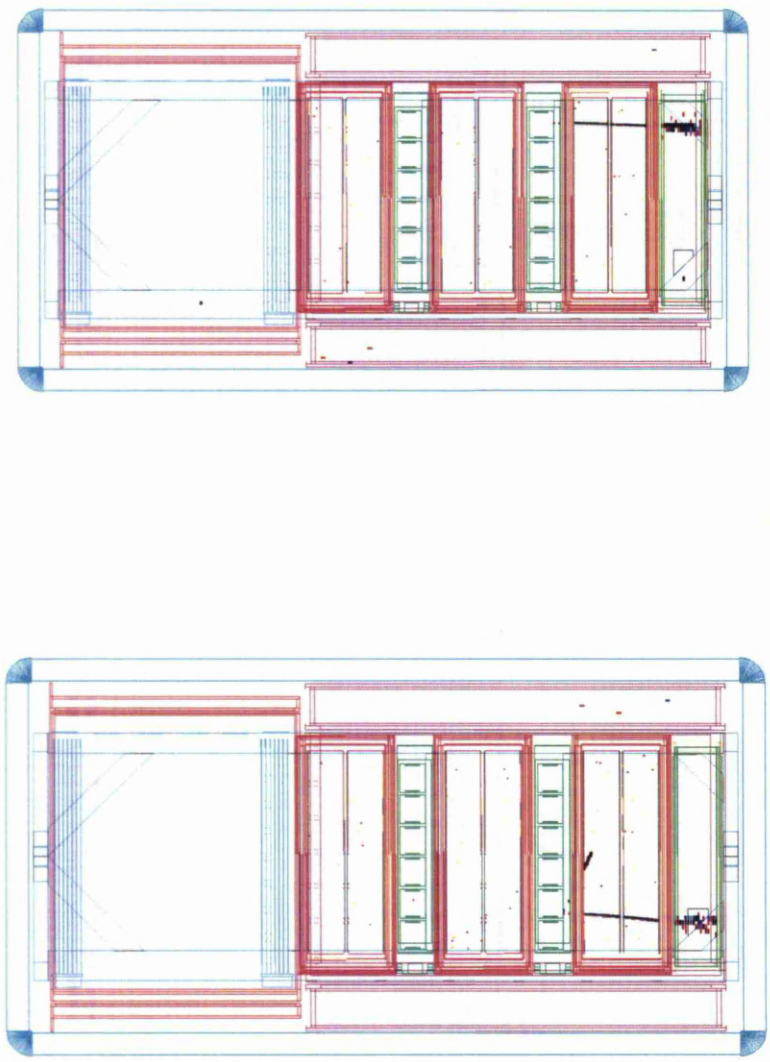

Figure 8.23: Event displays of one (top) and two (bottom) track ν_e candidates selected in the FGD2.

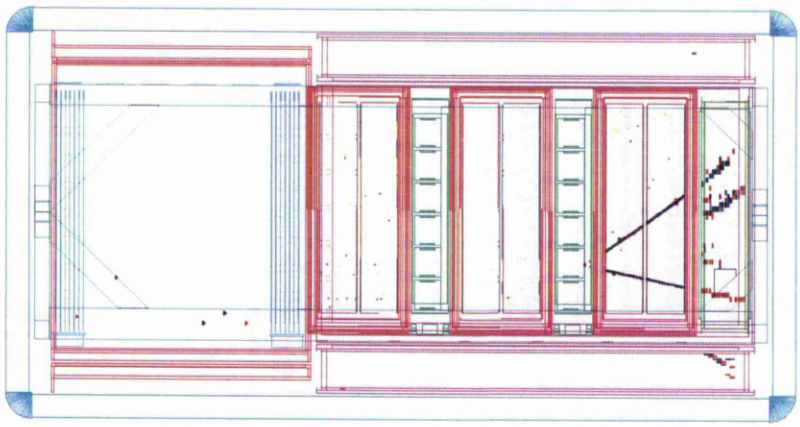

Figure 8.24: Event display of a multi-track ν_e candidate selected in the FGD2.

Run	Selected events
31	1
32	11
33	10
34	12
Total Run-I	34 (MC expected 35.1)
36	13
37	81
38	14
Total Run-II	108 (MC expected 94.8)

Table 8.8: Electron neutrino candidates selected per run. Number in parenthesis shows the expected number from the MC.

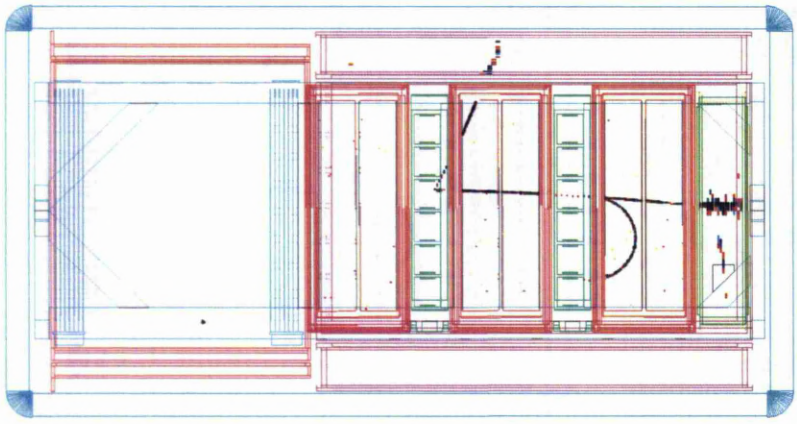

Figure 8.25: Event display of a ν_e candidates selected in the FGD1. The electron track passes through TPC2-FGD2-TPC3 and going into the DsECal developing a shower. Both TPCs agree with the electron hypothesis. Another track goes into the BrECal. A secondary low momentum track (probably a δ-electron) is created during the propagation of the electron candidate.

	TPC1	TPC2	TPC3
Run31	1.07	1.05	1.09
Run32	1.07	1.05	1.08
Run33	0.98	0.97	0.96
Run34	1.02	0.99	1.01
Run36	1.02	1.00	1.05
Run37	1.03	1.01	1.06
Run38	1.04	1.03	1.07

Table 8.9: The calibration correction applied to C_T^{meas} using the through-going muons.

8.13 Muon mis-identification using through-going muons

The muon mis-identification probability studies the muons mis-identified as electrons and the difference between data and MC. The study of the through-going muons is important for two main reasons. The first is for the TPC C_T calibration and the second is for the estimation of muon mis-identification probability for both the DsECal and the TPC. The main idea is the same for both cases. Taking the long tracks, going through the 3 TPCs and the DsECal, and then using the PID of the TPCs to monitor the DsECal or the other way around.

8.13.1 Muon energy loss calibration

The corrections to the TPC energy loss applied for MIPs is performed on a run by run basis and for each TPC separately. For each run, the long tracks passing through the three TPCs and agreeing with the ECal track hypothesis are selected. For each TPC then a correction factor is applied in order to centralize the muon pull at zero. The correction applied is shown in Table 8.9. The result of the TPC calibration is shown in Figure 8.26. A small contamination of muons for Beam-Run 31 and for TPC3 appear to be at the low negative muon pull region. This might be related to the low MM gain issue during Run-I data taking [117]. Since the total number of these tracks is very small, they are removed from the TPC muon mis-identification probability. Finally, the muon pull in the MC is checked so that it is centralized at zero for all three TPCs.

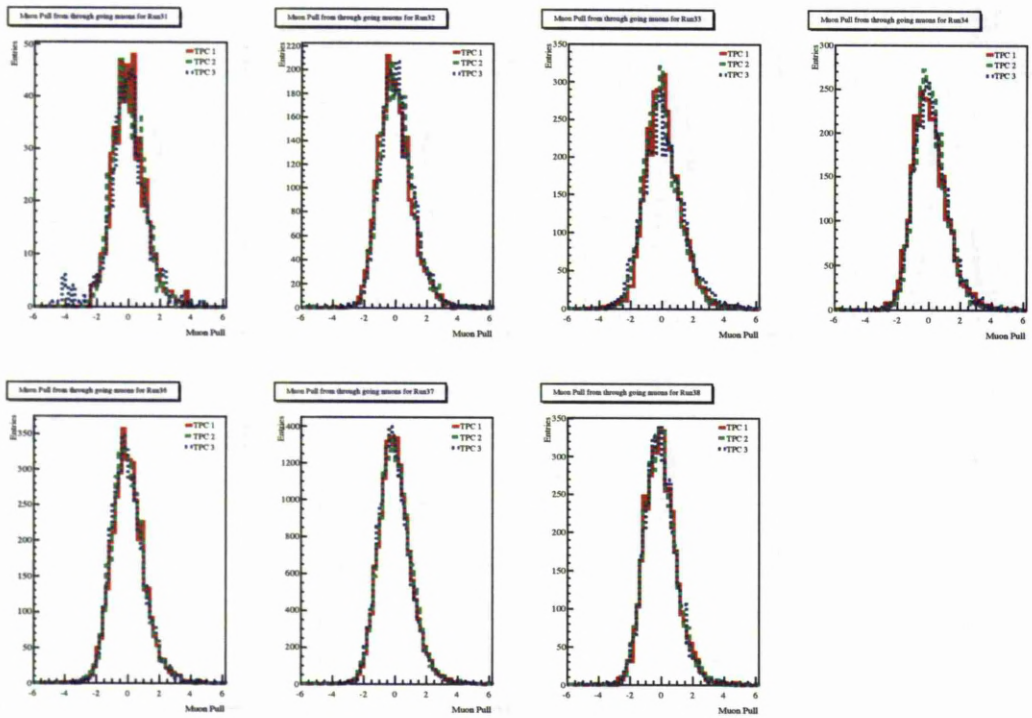

Figure 8.26: Muon pulls for all Runs and TPCs after the C_T calibration.

8.13.2 TPC Muon mis-identification probability

The muon mis-identification probability is studied separately for the TPCs and the DsECal. For the TPCs, negative long tracks passing through the three TPCs are selected. The ECal PID is then applied to remove shower like clusters; this is TrShVar > 0.4 and $E_{rec} < 400$ MeV/c. Then the TPC PID is checked. If the electron pull is less than two then the long track is treated as a possible mis-identified muon. Furthermore, if the muon pull is higher than 2, then the long track is treated as a true electron. The fraction of these two categories, to the total number of tracks selected is displayed in Figure 8.27. The differences between the three TPCs are also demonstrated in this plot. In general, TPC1 appears to have a higher rate of mis-identification probability. The same behavior is also visible in the MC as well. Since the performance of TPC1 has a negligible effect on this analysis, no further action is taken for this issue.

The study of mis-identified muons is only performed for tracks with a momentum more than 250 MeV/c. Below this momentum, the number of tracks selected is very small and also the ECal PID does not perform very well. A comparison between the muon and electron pull is shown in Figure 8.28. Most of the selected tracks agree with the muon hypothesis, and very few with the electron hypothesis. A contamination of tracks is also agree with both the muon and electron pulls.

From Figure 8.27 the muon mis-identification probability is below 1 % for momentum below 1 GeV/c, and below 2 % for momentum above 1 GeV/c. The cases that the muon and electron pulls agree are also shown on this plot and the mis-identification fraction is now up to 4 % for TPC2 and TPC3.

For the study of the muon mis-identification probability, a direct comparison with the MC is not possible. The reason is that the MC does not simulate the sand muons, thus only the POD muons are simulated. The differences might be important on the energy scale of the selected muons and also on the through-going beam composition. However, an approximation on the beam composition can be performed with the MC, revealing that 99 % of the tracks selected in the DsECal are true muons and 99 % of the background are pions.

8.13.3 DsECal Muon mis-identification probability

A similar procedure is followed to monitor the DsECal muon mis-identification probability. The TPC PID from all the three TPCs is used to select an almost pure muon beam. This is done by selecting only negative long tracks where the muon pull is less than two and the electron pull is more than two. Then the ECal PID is studied and the tracks that do not agree with the MIP hypothesis are treated as a muon mis-identified as electron. The ECal PID output and the ECal energy are displayed in Figure 8.29. A comparison between the ECal energy and the TPC momentum is shown in Figure 8.30.

The DsECal muon mis-identification probability is shown in Figure 8.31, with the muon mis-identification probability to be less than 1 % between 0.5-1 GeV/c and below 2 % for momentum above 1 GeV/c. The beam purity is studied through the MC and is composited of 99.5 % of muons with the remaining 0.5 % to be almost entirely pions.

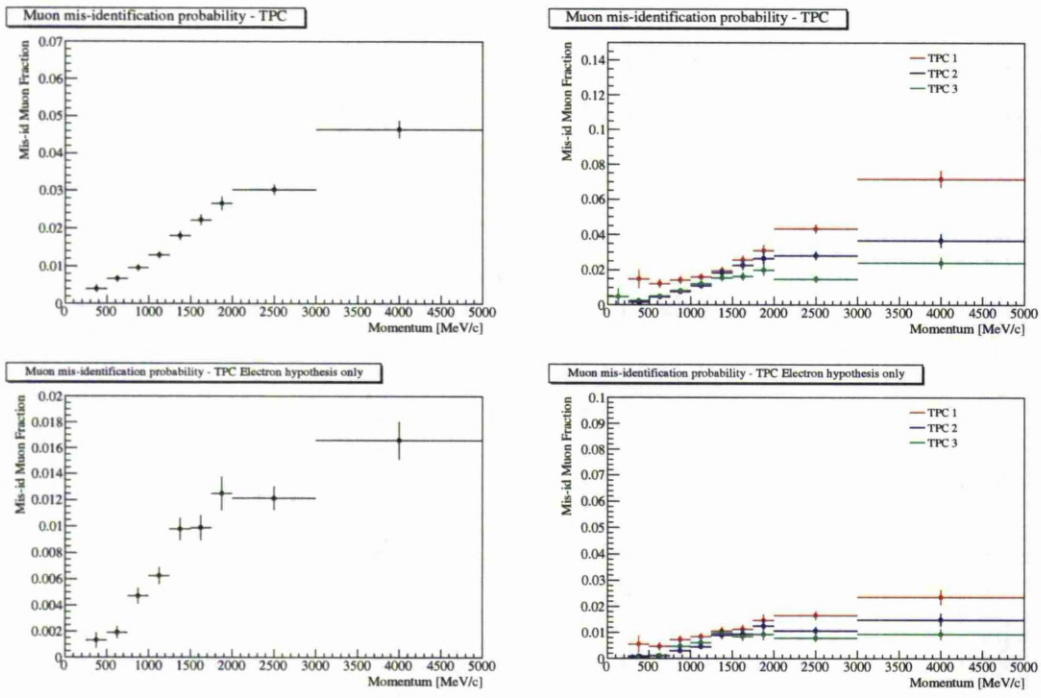

Figure 8.27: The TPC muon mis-identification probability for all 3 TPCs (top left) and each TPC separately (top right). The bottom plots show the cases where the TPC pull agrees only with the electron hypothesis.

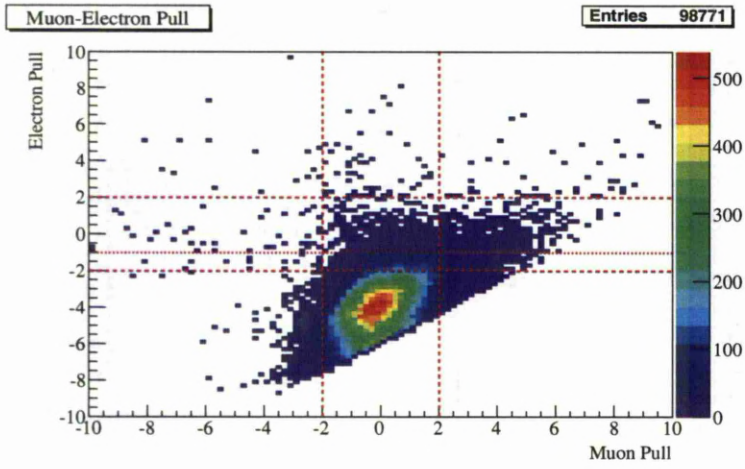

Figure 8.28: Comparison between the muon and electron pulls for through-going muons.

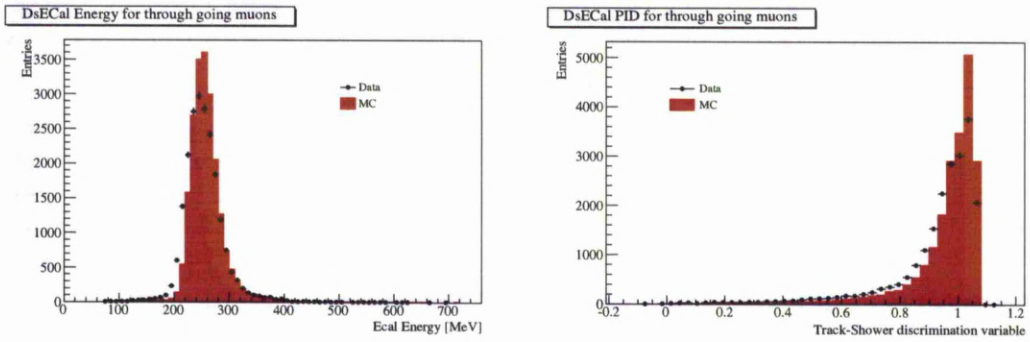

Figure 8.29: The ECal energy (left) and the neural network output (right) for through-going muons to study the DsECal mis-identification probability. Plots are normalized by area.

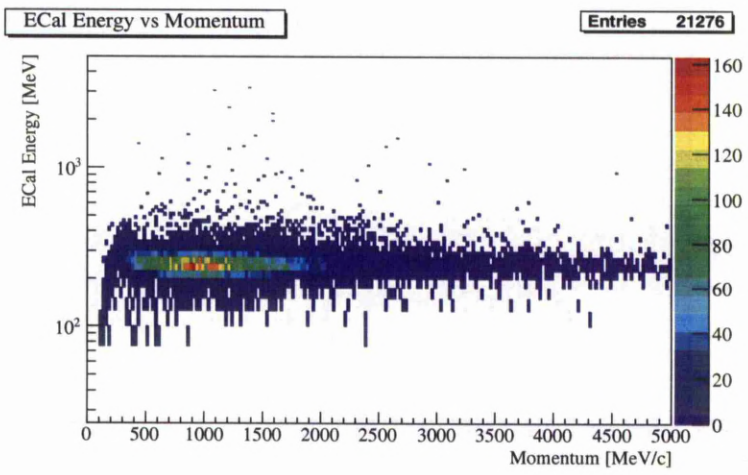

Figure 8.30: The ECal energy and the TPC momentum for through-going muons to study the DsECal mis-identification probability.

8.14 Fit of the electron neutrino spectrum

A method to extract the ν_e signal and separate from the background has been developed. The method builds the signal and background probability density functions (pdf). Kernel estimation is used for the pdf construction [118]. The background is separated into three different components; NC, CC non-ν_e and out of FGD. The pdf of the three background components is built separately, and the total background pdf is the sum of the three. The total signal plus background pdf is built. The fit then has two free parameters, the number

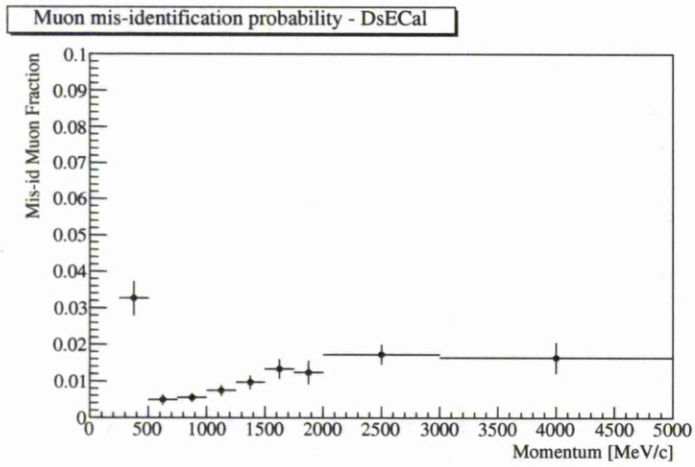

Figure 8.31: The muon mis-identification probability in the DsECal.

of signal events, (n_{sig}), and the number of background events, (n_{bkg}).

Then an unbinned maximum likelihood fit is performed. In general, the likelihood function of a parameter $\bar{p}$ for a sample $x_1, ..., x_n$ is defined as

$$L(\bar{p}) = \prod_i F(\bar{x}_i; \bar{p}), \tag{8.6}$$

where $F(\bar{x}_i; \bar{p}) > 0$ is the pdf and $\int F(\bar{x}_i; \bar{p}) \equiv 1$. For convenient the negative log likelihood is often used

$$-\ln L(\bar{p}) = -\sum_i \ln F(\bar{x}_i; \bar{p}). \tag{8.7}$$

The fit is repeated for 1000 virtual experiments. The mean value of the fitted n_{sig} is then selected as the most probable value. The fit method is first validated with the MC by checking that the MC is approximately returning the input values, with input $n_{sig} = 680$ and returned from the fit $n_{sig} = 695.3 \pm 80.4$ and input $n_{bkg} = 1214$ and returned $n_{bkg} = 1198.8 \pm 84.2$ (Figure 8.32). A second validation is done by normalizing the MC pdfs to the data expectation with similar results. The shape of the signal and background pdfs are shown on Figure 8.33.

The fit is then repeated 1000 times on data in the range 0-5000 MeV/c with 139 data events and 123.9 expected from the MC. The normalization of the total (signal + back-

ground) pdf is changed to the number of events, and the fit is performed with two free parameters, the number of signal and background events. The results are summarized in Figure 8.34 with

$$n_{sig} = 51.2 \pm 21.3 \text{ stat.}, \tag{8.8}$$

and

$$n_{bkg} = 88.3 \pm 22.4 \text{ stat.} \tag{8.9}$$

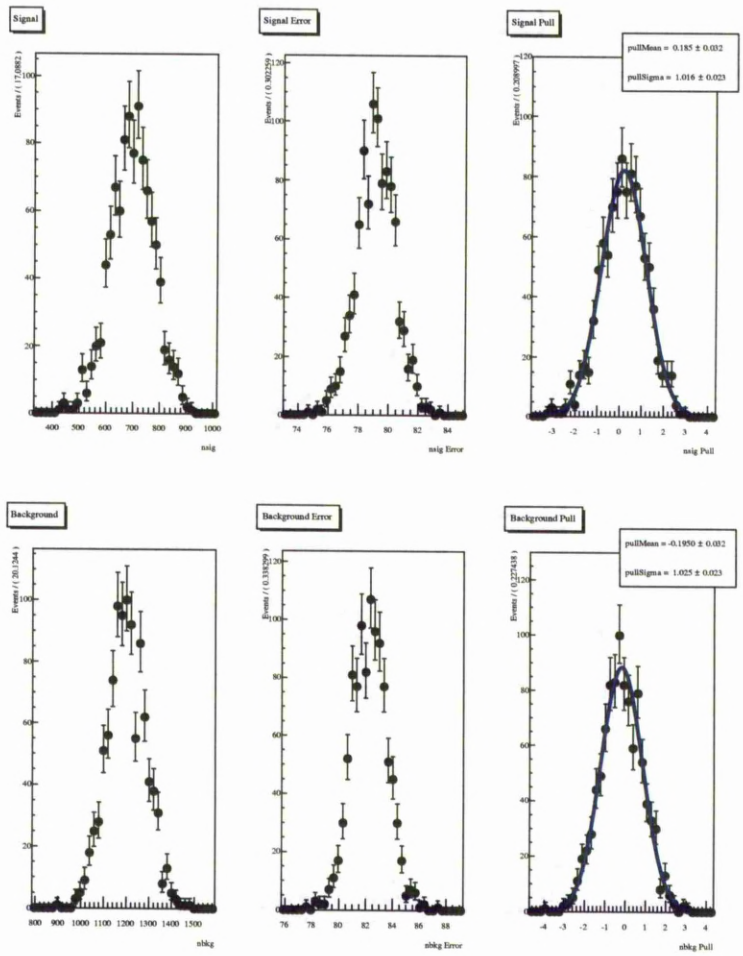

Figure 8.32: The validation of the fit method with 1000 toy MC experiments. The plots show the signal, signal error and pull (top) and background, background error and pull (bottom).

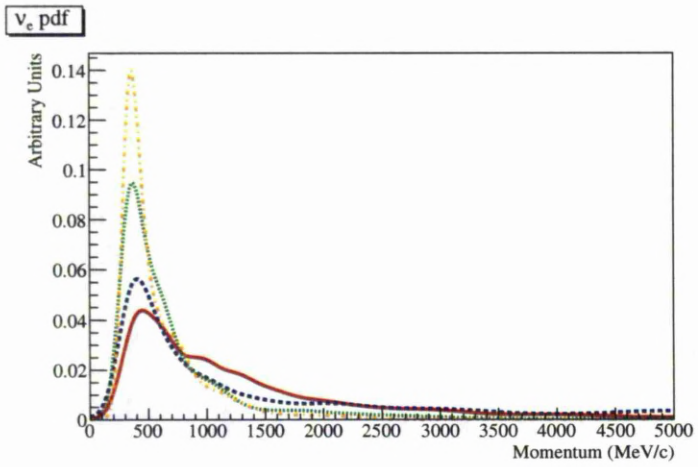

Figure 8.33: The shape of the signal and background pdfs built from the MC. Red (solid) line is the CC ν_e, blue (dashed) line is the CC non ν_e, green (dotted) line is the NC, orange (dashed-dotted) line is the out of FGD. All pdfs are normalized to unity.

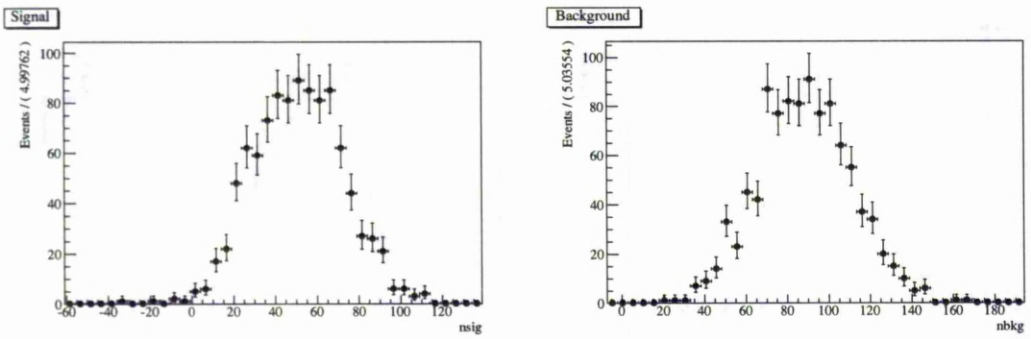

Figure 8.34: The fit result for 1000 experiments. Signal events on the left and background events on the right.

The study of the systematics is done by varying the background shape of the three background components. This is done in two steps. First, the normalization of each of the background pdfs is changed, but the overall normalization for the background pdf is kept the same. This is done to understand the differences in the background shape estimation, if the overall background normalization is constant. The second step is to change the normalization of the signal or one of the background component's pdf and redo the fit. For both steps, the difference from the nominal fit value is taken as the systematic. The next section

will discuss the estimation and evaluation of the systematic uncertainties.

8.15 A discussion on the systematic uncertainties

For the current electron neutrino analysis the study of the systematic uncertainties is kept as simple as possible. Although the study is not performed in extended detail, it is sufficient enough to give a first order estimation on the systematic uncertainties. The study of systematic uncertainties is separated in the categories:

- Detector systematics
- Muon mis-identification
- Background from outside the tracker
- NC and non- ν_e CC interactions.

8.15.1 The positive sample

Before moving to a discussion of the systematic uncertainties, a study selecting positive tracks as a control sample has been performed. The selection is exactly the same except of the charge cut which is now positive. The positive sample, although it could be used as an extra cut to further improve the selection, it will be instead used as an independent sample to study the charge mis-identification and also to estimate the backgrounds coming from outside the tracker. The selection of positive tracks returned 322 positron candidates with 292.7 events expected from the MC. The ratio data/MC is approximately the same as the electron selection. As the ν_e and $\bar{\nu}_e$ contamination in the positive sample is negligible the same excess in the two samples could lead to the conclusion that the excess in the data is due to background. However, for this analysis the fit is left free to decide how to deal with the excess in the data, treating similarities or differences in the positive and negative analysis as systematic uncertainties. The positron candidates are shown in Figure 8.35, with the biggest background now protons, especially in the region around 1 GeV/c where the proton and electron energy loss curves in the TPC cross. As it can also be seen from Table 8.10, protons actually populate the positive sample.

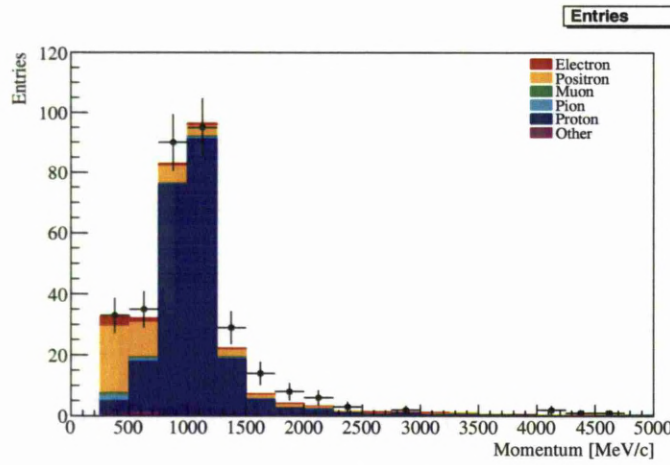

Figure 8.35: The momentum distribution of the positron candidates from the positive selection.

	Negative sample	Positive Sample
Electron	96.6	8.2
Positron	7.7	53.1
Muon	14.0	4.2
Pion	3.6	5.7
Proton	7.3	219.3
Other	0.6	2.2
Total	129.8	292.7

Table 8.10: Particle type expected from the MC from the negative and positive analysis.

8.15.2 Detector systematics

As already mentioned the study of the systematics uncertainties is meant to be as simple as possible. The vertex, PID and kinematics systematics are studied.

Hit finding: The FGD hit finding is important for the vertex position reconstruction. Due to the small number of FGD planes along the Z direction (32 for FGD1 and 14 for FGD2), if the closest hit to the vertex in the FGD is not reconstructed or the hit-track matching fails, then the position of vertex could be different and varies inside or outside the FV. For this study, all tracks associated to a reconstructed vertex point and before the application of any cuts are propagated backwards searching for unused FGD hits in a 2D XY radius less than 5 cm. 0.3 % of all the tracks checked are found to be associated with an

unused FGD hit. This fraction is approximately the same in the data and MC and is taken as the systematic uncertainty.

Broken tracks: In the case that the detector matching failed, a long track could be reconstructed as two or more tracks. The case studied here is when the detector matching between TPC2-FGD2 failed. This source of failure could result a track originating in FGD1 to be reconstructed in FGD2 if the secondary broken track is more energetic. The tracks reconstructed in FGD2 are propagated backwards and search for other tracks that stop at the end of TPC2 in a 5 cm 2D XY radius. In total 0.1 % tracks are matched between TPC2-FGD2 (approximately the same in data and MC) with a 65 % efficiency that the tracks matched come from the same parent particle.

Vertex efficiency: The vertex reconstruction algorithm reconstructs a vertex with approximately 94 % efficiency. In terms of ν_e efficiency this mean that approximately 0.7 % of true ν_e vertices will not be reconstructed. When the vertex reconstruction algorithm fails to find a vertex, while there is at least one good track in a TPC, then the most energetic track among all negative tracks is selected and its initial position is assumed to be the vertex position. The difference in the events selected with the latter approach are removed from the data and MC and the ratio data/MC is recalculated with a difference at 0.2 %.

Track and vertex mis-reconstruction: Track or vertex mis-reconstruction refers to vertices reconstructed outside the FGD while the true vertex is in the FGD or tracks where the direction of the track is not calculated properly or the initial and final positions of a track is wrongly reversed. The estimation of this number using the MC and removing these events from data and MC samples results in a 0.8 % difference in the ratio data/MC.

TPC PID: The effect of the C_T calibration on the electron pull has been studied extensively in [119] using cosmics for Run-I data taking. The method described in [119] to calibrate the pulls and the software version are different from the one used in this analysis and the estimation is based on the pull width difference between data and MC with a 4 % difference. Since this is the only study performed so far to estimate the differences in the electron pull between data and MC, the coresponding systematic obtained is also adopted for this analysis as well. Thus, in terms of the current selection this is translated to a 2.2 % systematic uncertainty in the ratio data/MC.

ECal PID: The systematic uncertainty for the ECal PID is studied separately for the energy reconstruction and neural network output. From the DsECal testbeam a 5.2 % correction on the reconstructed energy was applied in order to centralise the reconstructed electron energy in the MC. The same correction has been applied to the data and MC used for this analysis. Removing this correction and redoing the analysis returned a 1 % difference in the shower selection which is taken as the systematic. For the neural network output, the testbeam is used to test the shower selection efficiency between data and MC. The difference between data and MC changes for each testbeam momentum, and for the systematic uncertainty the difference between data and MC for all the momenta up to 2 GeV/c is summed resulting in a 1.2 % systematic uncertainty.

Systematics for the background rejection: For the number of cuts applied for the background rejection, the systematic uncertainty is assumed as the difference in the fraction of data events rejected to the fraction of MC events rejected. This returns a 2.5 % systematic uncertainty. Explicitly, the study of background from outside the tracker will be studied in the next section.

Charge mis-identification: The charge mis-identification could either result in the leakage of positive tracks into the negative sample or the leakage of negative tracks into the positive sample. An estimation of the wrong charge tracks entering the negative selection can be done by selecting protons in the momentum range 0.25-0.8 GeV/c. In this momentum region the TPC PID could select the protons. The tracks selected that agree with the proton hypothesis (proton pull < 2 and all other pulls > 2) are 65, with 100.6 expected from the MC with 85 % proton purity (Figure 8.36). The same procedure to select protons in the momentum range 0.25-0.8 GeV/c is repeated and for the positive selection. Now the proton purity is at 99 % and the excess in the MC dropped to 14 % (Figure 8.36). 14 % of the proton excess in the positive MC is removed from the MC proton expectation (Table 8.10) and then the new fraction of expected positive candidates is removed from the negative selection in data and MC, and the ratio data/MC is recalculated with a difference of -1.8 %. For the leakage of negative tracks in the positive selection the fraction of expected negative tracks are removed from the positive selection in both data and MC and the data/MC is different by +1.3%.

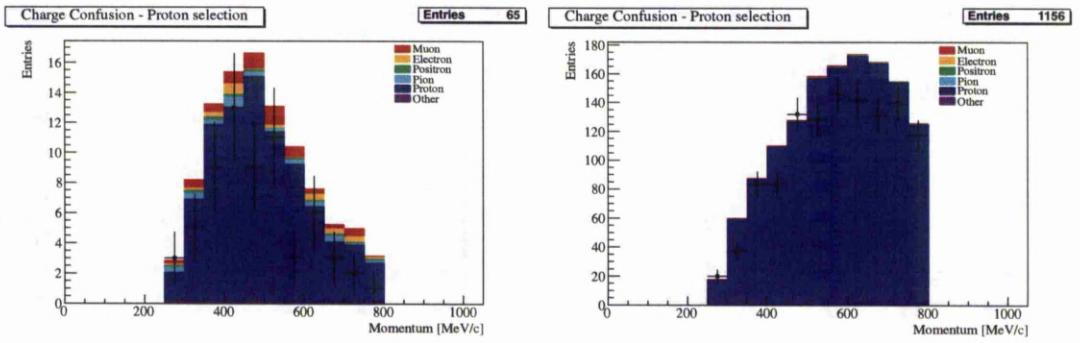

Figure 8.36: The proton selection in the TPC for the negative charge sample (left) and for the positive charge sample (right) in the momentum region 0.25-0.8 GeV/c. The excess in the MC is 30 % in the negative sample and 14 % in the positive sample.

Total detector systematic uncertainty: The quadratic sum of the list of the detector systematic mentioned above returns in total $^{+4.1}_{-4.2}$ % detector systematic uncertainty. Repeating the fit and changing the expected number of events by this uncertainty fraction and the difference from the nominal fit values are accounted as the systematic uncertainty in the number of signal and background events. The differences are $n_{sig}\ ^{+2}_{-2.2}$ and $n_{bkg}\ ^{+2.1}_{-2.8}$.

8.15.3 Muon mis-identification

The muon mis-identification probability is estimated in section 8.13. The CC ν_e selection is then separated into two samples, one with the events identified by the TPC+ECal PID and the other with the events identified by only the TPC PID (Figure 8.21). These two samples are then divided again into two other samples, separating the tracks with TPC2 and TPC3. The mis-identification probability is applied differently to the two TPCs. For the events with the TPC+ECal PID selection the TPC and ECal mis-identification probability is multiplied and the number of mis-identified muons is extracted by comparing the data and the MC. The same method is applied and for the events with no ECal PID selection but this time only using the TPC mid-identification probability and comparing the data with the MC. The comparison between data and the MC reveals 2.13 ± 0.26 event excess in the data. These events are used to change the background pdf normalization and repeating the fit gives a difference from the nominal values for the signal $n_{sig}\ ^{+0}_{-0.9}$ and for the background $n_{bkg}\ ^{+0.5}_{-0}$.

8.15.4 Out of tracker activity

The estimation of the activity outside the tracker is very important to understand since it is one of the most important backgrounds to the ν_e analysis. The main source of this background is photons created in other parts of the detector, but converged in the FGDs. Although electrons coming from photons populate the low momentum region, the contamination at higher momenta is also important.

To study the differences in the contamination of this background at low and high momenta, two different samples are selected. The first selects tracks with activity outside the tracker and with momentum less than 200 MeV/c. This sample is mainly populated from events coming from outside the tracker; the contamination of true neutrino interactions is very small. The second samples selects all the tracks with activity outside the tracker for the whole momentum spectra. The detectors identified with this activity are demonstrated in Figure 8.37. The first thing to notice from this figure is the very high activity in the SMRD for the data. A track in the SMRD can be reconstructed even with two hits only, making the separation of true tracks and noise very difficult. Events with isolated SMRD or ECal+SMRD activity are not considered for the background estimation; only tracks with POD activity are considered.

For the selection of tracks with momentum less than 200 MeV/c, 233 events are selected in the data with 202.5 expected from the MC. From the second sample containing all the tracks in all momenta, 578 events are selected in the data with 415.8 expected from the MC, resulting in an increase of 17.3 % in the data/MC background estimation for the second sample (all momentum region).

The same procedure is repeated and for the positive analysis, resulting in some significant differences. The data/MC for the events with activity in the POD now decreases for all momenta by 8.6 % comparing with the data/MC for momenta below 200 MeV/c. For the study of the systematic uncertainties, a 30 % error will be assumed on the out of FGD pdf. The details of the extraction of the systematic uncertainty on the number ν_e number will be discussed in the next section.

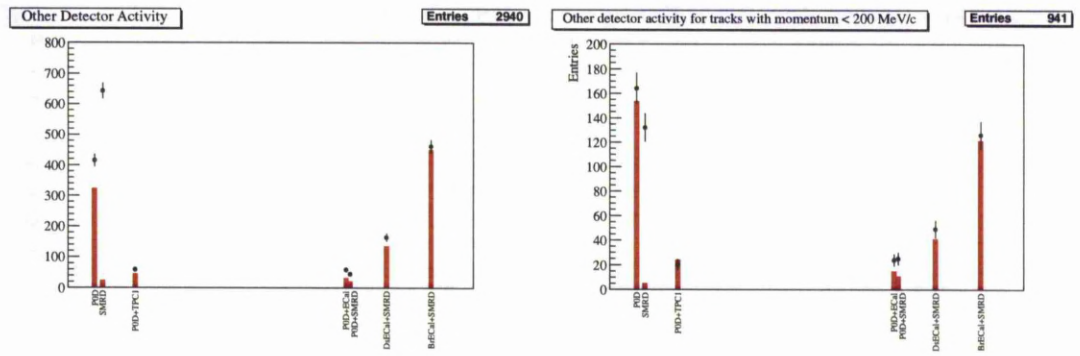

Figure 8.37: The activity outside the tracker for tracks for all momenta (left) and with momentum less than 200 MeV/c (right). Red (sketched) area is the MC.

8.15.5 NC and CC uncertainties

Cross section systematic uncertainties are contaminated by the NC and CC π^0 production. The total error for these two types of background is assumed to be 30 % [62]. The estimation of the systematic uncertainty on the ν_e will be discussed in the next section.

8.16 Systematic uncertainty on the neutrino fit

In this section we will estimate the systematic uncertainties due to cross sections and outside the FGD background. The study of these systematics is treated in two parts. The first part deals with the shape uncertainties and the second with the normalization uncertainties.

The shape uncertainties are studied by modifying the normalization of the NC, CC and out of FGD pdfs by 30 %, but at the same time keeping the normalization of the overall background pdf the same. Thus only the shape of the background pdf is changed. This study will determine the case where the shape of the signal pdf is correctly estimated while the shape of the background pdfs is varied. The variation of the three background pdfs is performed by pairs and modifying the components of each pair by $\pm$ 30 %. For each case (12 in total) the fit is re-evaluated with 1000 experiments and the mean is selected as the new fit result. The difference from the nominal fit result is taken as the systematic uncertainty. The quadratic sum for all the 12 cases, returns $\pm$ 2.0 events for the signal and $\pm$ 2.3 events for the background.

For the normalization uncertainties the most extreme cases, returning the highest val-

ues for the error bars, are considered for the systematic estimation. These are: all the background components are simultaneously shifted by $\pm$ 33 % (15 % flux uncertainty [77] and a 30 % for the cross section uncertainty, which is the maximum cross section uncertainty for CC neutrino interactions [62]). The pdf describing the background outside the FGD is only counted for the underestimation since from the tracker background studies it only contributes to increase the background expectation. The next case is also to incude the signal pdf normalization in this calculation as well. This contributes to an uncertainty to the signal pdf at $\pm$ 33 % and finally to modify all the signal and background pdfs by $\pm$ 33 %. The overall uncertainty from this estimation is $n_{sig}\ ^{+9.7}_{-14.1}$ and $n_{bkg}\ ^{+14.3}_{-3.9}$.

The total systematic is estimated as the quadratic sum from all the sources of systematic uncertainties. The final results for the ν_e events expected in the near detector is

$$n_{sig} = 51.2^{+21.3\ \text{stat.}\ +10.1\ \text{sys.}}_{-21.3\ \text{stat.}\ -14.4\ \text{sys.}} \tag{8.10}$$

and for the background events is

$$n_{bkg} = 88.3^{+22.4\ \text{stat.}\ +14.6\ \text{sys.}}_{-22.4\ \text{stat.}\ -5.3\ \text{sys.}} \tag{8.11}$$

The electron neutrino selection for the first year of data taking at T2K near detector ND280 is based on a vertex selection in one of the two FGDs FV and in time with one of the bunches. The most energetic track among all negative tracks is selected and the TPC and ECal PID is checked to agree with the electron hypothesis. A series of other cuts are then applied in order to remove background electrons, mainly coming from photons. The pdf of the signal CC ν_e is built using the MC and a fit over the neutrino spectrum returned 51.2 ν_e candidates with 44.4 candidates expected from the MC in the momentum range 0-5 GeV/c. The ratio, data/MC, is $1.15\ ^{+0.15}_{-0.33}$.

Chapter 9

Conclusions

This thesis is separated into three main topics. The first is to measure the electron neutrino component at the near detector, the second is the electron analysis in the DsECal testbeam and the third is the construction of the BrECal modules. Other general topics, like neutrino physics and cross sections, beam and detector simulation and track reconstruction have also been discussed.

The main goal of this thesis is to study the beam electron neutrino component in the near detector, ND280. The selection of electron neutrino in ND280 is very challenging due to the small contamination of beam ν_e and also due to the large electron background. The analysis developed in this thesis is optimized to separate electrons from the other particles using the TPC and ECal PID and also to reject the electron background contamination coming mainly from photons originating either from a π^0 inside the FGDs or coming from outside the tracker region. After the cut optimization and a simple estimation of the systematics uncertainties, the final number of the electron neutrino events selected in the momentum range 0-5 GeV/c is $51.2^{+21.3\ \text{stat.}\ +10.1\ \text{sys.}}_{-21.3\ \text{stat.}\ -14.4\ \text{sys.}}$ for 1.068×10^{20} protons on target and with a MC expectation of 44.4 events. This result is a supplementary statement to the $\nu_\mu \rightarrow \nu_e$ oscillation signal observed at Super-Kamiokande during the first year of T2K run [62], as no significant excess in the expected ν_e beam contamination has been observed.

A selection of electrons has also been studied using the DsECal testbeam. Testbeam electrons are quite important for the ECal PID and energy reconstruction uncertainties and also for a general reconstruction and calibration validation in the calorimeter. An independent ECal PID method based on the Kalman filter following the ECal cluster on a hit by hit

basis has been developed to separate between tracks and showers and has been successfully tested using the DsECal testbeam.

Finally, a detailed procedure for constructing a sampling calorimeter has been described. The construction of the BrECal modules was an important task to be completed and on a very limited time-line. The procedure described follows the construction of a calorimeter layer, the addition to each scintillation bar of an optic fiber and finally the test of the optic fiber attenuation with a radioactive source and replacing it in the case it is found to be damaged.

Bibliography

[1] F.A. Scott, "Energy Spectrum of the Beta-Rays of Radium E," *Phys. Rev.* , vol. 48, pp. 391–395, 1935.

[2] J. Chadwick, "Possible Existence of a Neutron," *Nature* , vol. 129, p. 312, 1932.

[3] E. Fermi, "Towards the Theory of β-Rays," *Z. Phys.* , vol. 8, pp. 161–177, 1934.

[4] Shoichi Sakata and Takesi Inoue, "On the correlations between Mesons and Yakawa Particles," *Prog. Theor. Phys.* , vol. 1, pp. 143–150, 1946.

[5] C. Cowan *et al.*, "Detection of the free neutrino: A confirmation," *Science* , vol. 124, p. 103, 1956.

[6] F. Reines *et al.*, "Detection of the free antineutrino," *Phys. Rev.* , vol. 117, pp. 159–173, 1960.

[7] B.Pontecorvo *Zh.Eksp.Teor.Fiz.* , vol. 33, p. 549, 1957.

[8] B.Pontecorvo *Sov.Phys.-JETP* , vol. 6, p. 429, 1958.

[9] Z.Maki, M. Nakagawa and S.Sakata, "Remarks on the unified Models of Elementary Particles," *Prog. Theor. Phys.* , vol. 28, p. 870, 1962.

[10] G.Dandy *et al.*, "Observation of High-Energy Neutrino Reactions and the Existence of Two Kinds of Neutrinos," *Phys.Rev.Lett.* , vol. 9, pp. 36–44, 1962.

[11] M. Perl *et al.*, "Evidence for anomalous lepton production in the e^+-e^- annihilation," *Phys. Rev. Lett.* , vol. 35, pp. 1489–1492, 1975.

[12] F. Hasert *et al.*, "Search for elastic muon-neutrino electron scattering," *Phys.Lett. B* , vol. 46, pp. 121–124, 1973.

[13] F. Hasert *et al.*, "Observation of neutrino-like interactions without muon or electron in the gargamelle neutrino experiment," *Phys.Lett. B* , vol. 46, pp. 138–140, 1973.

[14] D. DeCamp *et al.*, "Determination of the number of light neutrino species," *Phys.Lett. B* , vol. 231, pp. 519–529, 1989.

[15] K. Kameda *et al.*, "Observation of the tau neutrino," *Phys.Lett. B* , vol. 504, pp. 218–224, 2001.

[16] R. Davis, D. S. Harmer and K.C. Hoffman, "Search for neutrinos from the Sun," *Phys. Rev. Lett.* , vol. 20, pp. 1205–1209, 1968.

[17] J.N. Bahcall, N.A. Bahcall and G. Shaviv, "Present status of the theoretical predictions for the ^{37} Cl Solar-neutrino experiment," *Phys. Rev. Lett.* , vol. 20, pp. 1209–1212, 1968.

[18] Y.Fukuda *et al.*, "Atmospheric ν_μ/ν_e ratio in the multi-GeV energy range," *Phys. Lett. B* , vol. 335, pp. 237–245, 1994.

[19] P. Anselmann *et al.*, "Solar neutrinos observed by GALLEX at Gran Sasso," *Phys.Lett. B* , vol. 285, pp. 376–389, 1992.

[20] J. Abdurashitov *et al.*, "Results from SAGE (The Russian-American Gallium Solar neutrino source measurement)," *Phys.Lett. B* , vol. 328, pp. 234–248, 1994.

[21] S. Fukuda *et al.*, "Solar ^8B and hep neutrino measurements from 1258 days of Super-Kamiokande data ," *Phys. Rev. Lett.* , vol. 86, p. 5651, 2001.

[22] J. Yoo *et al.*, "Search for periodic modulations of the solar neutrino flux in the Super-Kamiokande I," *Phys. Rev. D* , vol. 68, p. 092002, 2003.

[23] M. Smy *et al.*, "Precise measurement of the solar neutrino day-night and seasonal variation in Super-Kamiokande I," *Phys. Rev. D* , vol. 69, p. 011104, 2004.

[24] Q. Ahmad *et al.*, "Measurement of day and night neutrino energy spectrum at SNO and constraints on neutrino mixing parameters," *Phys. Rev. Lett.* , vol. 89, p. 011302, 2002.

[25] Q. Ahmad *et al.*, "Direct evidence for neutrino transformation from neutral current reactions in the Sudbury Neutrino Observatory," *Phys. Rev. Lett.* , vol. 89, p. 011301, 2002.

[26] S.M. Bilenky and B. Pontecorvo, "Lepton mixing and neutrino oscillation," *Phys. Rep.* , vol. 41, pp. 225–261, 1978.

[27] E. Kearns, "Experimental measurements of atmospheric neutrinos," *Nucl. Phys. Proc. Suppl.* , vol. 70, p. 315, 1999.

[28] K. Egushi *et al.*, "First results from KamLAND: Evidence for reactor antineutrino disappearance," *Phys. Rev. Lett.* , vol. 90, p. 021802, 2003.

[29] M.Apollonio *et al.*, "Search for neutrino oscillations on a long baseline at the CHOOZ nuclear power station," *Eur. Phys. J. C* , vol. 27, pp. 331–374, 2003.

[30] F. Boehm *et al.*, "Final results from the Palo Verde neutrino oscillation experiment," *Phys. Rev. D* , vol. 64, p. 112001, 2001.

[31] F. Ardellier *et al.*, "Double Chooz: A search for the neutrino mixing angle θ_{13}," *hep-ex/0606025*.

[32] Daya Bay Collaboration, "A precision measurement of the neutrino mixing angle θ_{13} using reactor antineutrinos at Daya Bay," *hep-ph/0701029*.

[33] T. Schwetz, M. Tortola, and J. W. F. Valle, "Global neutrino data and recent reactor fluxes: status of three-flavour oscillation parameters," *New J. Phys.*, vol. 13, p. 063004, 2011.

[34] M. Ahn *et al.*, "Measurement of neutrino oscillation by the K2K experiment," *Phys. Rev. D* , vol. 74, p. 072003, 2006.

[35] P. Adamson *et al.*, "Measurement of neutrino oscillations with the MINOS detectors in the NuMI beam," *Phys. Rev. Lett.* , vol. 101, p. 131802, 2008.

[36] P. Adamson *et al.*, "Measurement of the neutrino mass splitting and flavor mixing by MINOS," *Phys. Rev. Lett.*, vol. 106, p. 181801, 2011.

[37] C. Kraus *et al.*, "Final Results from phase II of the Mainz Neutrino Mass Search in Tritium β Decay," *Eur. J. Phys.* , vol. C40, pp. 447–468, 2005.

[38] V. Lobashev *et al.*, "Direct search for mass of neutrino and anomaly in the tritium beta-spectrum," *Phys. Lett. B* , vol. 460, pp. 227–235, 1999.

[39] L. Bornschein *et al.*, "Direct search for mass of neutrino and anomaly in the tritium beta-spectrum," *Phys. Lett. B* , vol. 460, pp. 227–235, 1999.

[40] K. Assamagan *et al.*, "Upper limit of the muon-neutrino mass and charged-pion mass from momentum analysis of a surface muon beam," *Phys. Rev. D* , vol. 53, pp. 6065–6077, 1996.

[41] R. Barate *et al.*, "An upper limit on the τ neutrino mass from three- and five-prong tau decays ," *Eur. Phys. Jour. C* , vol. 2, pp. 395–406, 1998.

[42] W. Furry, "On Transition Probabilities in Double Beta-Disintegration," *Phys. Rev.* , vol. 56, pp. 1184–1193, 1939.

[43] S.M. Bilenky and S.T. Petcov, "Massive neutrinos and neutrino oscillations," *Rev. Mod. Phys.* , vol. 59, p. 671, 1987.

[44] H. Klaptor-Kleingrothaus *et al.*, "Latest results from the HEIDELBERG-MOSCOW double beta decay experiment," *Eur. Phys. Jour. A*, vol. 12, pp. 147–154, 2001.

[45] C. Arnaboldi *et al.*, "New Limit on the Neutrinoless $\beta\beta$ Decay of ^{130}Te," *Phys. Rev. Lett.* , vol. 95, p. 142501, 2005.

[46] S.R. Elliott and J. Engel, "Double-beta decay," *J. Phys. G* , vol. 30, p. R183, 2004.

[47] Mark C.Chen, "The SNO+ experiment," *hep-ex/08103694*, 2008.

[48] C. Athanassopoulos *et al.*, "Evidence for $\bar{\nu_\mu} \rightarrow \bar{\nu_e}$ oscillations from the LSND experiment at Los Alamos physics facility," *Phys. Rev. Lett.* , vol. 77, p. 3082, 1996.

[49] C. Athanassopoulos *et al.*, "Results on $\nu_\mu \rightarrow \nu_e$ neutrino oscillations from the LSND experiment," *Phys. Rev. Lett.* , vol. 81, p. 1774, 1998.

[50] A. A. Aguilar-Arevalo *et al.*, "A search for electron neutrino appearance at the Δm^2 $1eV^2$ scale," *Phys. Rev. Lett.* , vol. 98, p. 231801, 2007.

[51] A. A. Aguilar-Arevalo *et al.*, "Unexplained excess of electronlike events from a 1 GeV neutrino beam," *Phys. Rev. Lett.* , vol. 102, p. 101802, 2009.

[52] A. A. Aguilar-Arevalo *et al.*, "A search for electron Antineutrino appearance at the Δm^2 $1eV^2$ scale," *Phys. Rev. Lett.* , vol. 103, p. 111801, 2009.

[53] A. A. Aguilar-Arevalo *et al.*, "Event Excess in the MiniBooNE Search for $\bar{\nu_\mu} \rightarrow \bar{\nu_e}$ Oscillations," *Phys. Rev. Lett.*, vol. 105, p. 181801, 2010.

[54] B.Kayser, "On the quantum mechanics of neutrino oscillations," *Phys.Rev. D* , vol. 24, p. 110, 1981.

[55] C.Giunti and C.W.Kim, "Quantum mechanics of neutrino oscillations," *Phys.Lett.* , vol. 14, p. 213, 2001.

[56] C.Giunti, "Neutrino wave packets in quantum field theory," *JHEP* , vol. 0211, p. 017, 2002.

[57] W. Yao *et al.*, "Review of particle physics ," *Journal of physics G* , vol. 33, 2006.

[58] G.Fogli and E.Lisi, "Evidence for the MSW effect," *New Journal of Physics* , vol. 6, p. 139, 2004.

[59] T.Schewtz, M. Tortola, J.W.F.Valle, "Three flavour neutrino oscillation update," *New J. Phys.* , vol. 10, p. 113011, 2008.

[60] T2K Internal Document.

[61] T2K Collaboration, "T2K ND280 Conceptual Design Report, T2K Internal document."

[62] K. Abe *et al.*, "Intication of Electron neutrino Appearance from an accelerator-Produced Off-Axis Muon Neutrino Beam," *Phys. Rev. Lett.*, vol. 107, p. 041801, 2011.

[63] T.Lux, "A TPC for the near detector at T2K," *J. Phys. Conf. Ser.* , vol. 65, p. 012018, 2007.

[64] M. Di Marco, "Test-bench for the characterization of MicroMegas modules for the T2K ND280 TPC," *J. Phys. Conf. Ser.* , vol. 65, p. 012019, 2007.

[65] A.Vacheret, "Characterization of the $1.3mm \times 1.3mm$ MPPC for the T2K near detectors," *Nucl. Instr. and Meth. A*, 2010.

[66] K. Yamamura *et al.*, "Products and Development Status of MPPC," in *International Workshop on new photon detectors*, PoS(PD09)017, 2009.

[67] M.Yokoyama *et al.*, "Performance of the Multi-pixel photon counters for the T2K near detectors," *Nucl. Instr. and Meth. A*, vol. 622, pp. 567–573, 2010.

[68] Hamamatsu Photonics K.K. http://www.hamamatsu.com.

[69] A.Vacheret *et al.*, "The Front-End readout system for the T2K ND280 detectors," in *Nuclear Science Symposium Conference Record*, pp. 1984–1991, 2007.

[70] S.Ritt and P.Amaudruz, "The MIDAS Data Acquisition System," in *Proc. IEEE* 10^{th} *Real Time Conference*, pp. 309–312, 1997.

[71] Midas online: https://midas.psi.ch/htmldoc/index.html .

[72] ROOT data analysis framework: http://root.cern.ch/ .

[73] Fluka version 2008.3c, http://www.fluka.org/fluka.php .

[74] S. Agostinelle and others, "Geant4 - A Simulatio Toolkit ," *Nucl. Inst. Meth. A*, vol. 506, pp. 250–303, 2003.

[75] J. Allison and others, "Geant4 Developments and Applications," *IEEE Trans. on Nucl. Sci. 53*, vol. 1, p. 270, 2006.

[76] http://www.staff.uni-mainz.de/zeitnitz/Gcalor/gcalor.html.

[77] N.Abgrall *et al.*, "Report from the NA61/SHINE experiment at the CERN SPS," *Technical Report CERN-SPSC-2010-025*, vol. SPSC-SR-066, 2010.

[78] N.Abgrall *et al.*, "Measurements of Cross Sections and Charged Pion Spectra in Proton-Carbon Interactions at 31 GeV/c," *PrePrint: CERN-PH-EP-2011-005*, 2011.

[79] C.Andreopoulos, "The GENIE Neutrino Monte Carlo Generator," *Ac. Phys. Polonica B*, vol. 40, p. 2461, 2009.

[80] http://www.genie-mc.org/ .

[81] Y.Hayato, "A Neutrino Interaction Program Library NEUT," *Ac. Phys. Polonica B*, vol. 40, p. 2477, 2009.

[82] Llewellyn-Smith, "Neutrnio reactions at accelerator energies," *Phys. Rept.*, vol. 3, p. 261, 1972.

[83] R.P. Feynman and M. Gell-Mann, "Theory of the Fermi interaction," *Phys. Rev.*, vol. 109, p. 193, 1958.

[84] I.S. Towner and J.C Hardy, "Currents and their Couplings in the Weak Sector of the Standard Model," in *Symmetries and Fundamental Interactions in Nuclei*, p. 183, 1995.

[85] J. Arrington, C. D. Roberts, and J. M. Zanotti, "Nucleon electromagnetic form factors," *J. Phys.*, vol. G34, pp. S23–S52, 2007.

[86] R. Bradford *et al.*, "A new parameterization of the nucleon elastic form factors," *Nucl. Phys. Proc. Suppl.*, vol. 159, pp. 127–132, 2006.

[87] H. Budd *et al.*, "Modelling quasi-elastic form factors for electron and neutrino scattering," *hep-ex/0308005*, 2003.

[88] R. G. Sachs, "High energy behavior of electromagnetic form factors," *Phys. Rev.*, vol. 126, pp. 2256–2260, 1962.

[89] M. H. Ahn *et al.*, "Indications of Neutrino Oscillation in a 250 km Long-baseline Experiment," *Phys. Rev. Lett.*, vol. 90, p. 041801, 2003.

[90] L. Ahrens *et al.*, "Measurement of neutrino-proton and antineutrino-proton elastic scattering," *Phys. Rev. D*, vol. 35, p. 785, 1987.

[91] K. Abe *et al.*, "Precise Determination of $\sin^2\theta_W$ from Measurements of the Differential Cross Sections for $\nu_\mu p \to \nu_\mu p$ and $\bar{\nu}_\mu p \to \bar{\nu}_\mu p$," *Phys. Rev. Lett.*, vol. 56, pp. 1107–1111, 1986.

[92] C.H.Albright *et al.*, "Neutrino-proton elastic scattering: Implications for weak-interaction models," *Phys. Rev. D*, vol. 14, pp. 1780–1798, 1976.

[93] D.Rein and L.M. Sehgal, "Neutrino Excitation of baryon resonances and single pion production," *Ann. Phys.*, vol. 133, p. 79, 1981.

[94] V. L. K.S. Kuzmin and V. Naumov, "Axial masses in quasielastic neutrino scattering and single-pion neutrino production on nucleons and nuclei," *Acta. Phys. Polon. B*, vol. 37, pp. 2337–2348, 2006.

[95] C.H. Albright and C. Jarlskog, "Neutrino Production of M^+ and E^+ heavy leptons," *Nucl. Phys. B*, vol. 84, pp. 467–492, 1974.

[96] A. Bodek and U. K. Yang, "Higher twist, ξ_w scaling and effective LO PDFs for lepton scattering in the few GeV region," *J. Phys. G*, vol. 29, pp. 1899–1906, 2003.

[97] M. Gluck *et al.*, "Dynamical parton distribution revisited," *Eur. Phys. J.*, vol. C5, pp. 461–470, 1998.

[98] T. Sjostrand, "High energy physics event generation with pythia 5.7 and jetset 7.4," *Comp. Phys. Commun.*, vol. 82, pp. 74–90, 1994.

[99] E. Jihn *et al.*, "A theoretical and experimental review of the weak neutral current: A determination of its structure and limits on deviations from the minimal SU(2) × U(1) electroweak theory," *Rev. Mod. Phys.*, vol. 53, p. 211, 1981.

[100] P. Musset and J. P. Vialle, "Neutrino physics with gargamelle," *Phys. Rept.*, vol. 39, pp. 1–130, 1978.

[101] D.Rein and L.M. Sehgal, "Coherent π^0 production in neutrino reactions," *Nucl. Phys. B*, vol. 223, p. 29, 1983.

[102] D.Rein and L.M. Sehgal, "PCAC and the deficit of forward muons in π^+ production by neutrinos," *Phys. Lett. B*, vol. 657, pp. 207–209, 2007.

[103] E. Moniz *et al.*, "Nuclear Fermi momenta from quasi-elastic electron scattering," *Phys.Rev.Lett.* , vol. 26, pp. 445–448, 1971.

[104] M. Antonello *et al.*, "Study of pion production in ν_μ CC interactions on oxygen using different MC generators," *Acta Phys. Polonica B* , vol. 40, pp. 2519–2536, 2009.

[105] M. Nakahata *et al.*, "Atmospheric Neutrino Background and Pion Nuclear Effect for KAMIOKA Nucleon Decay Experiment," *J. Phys. Soc. Jap.*, vol. 55, pp. 3786–3805, 1986.

[106] J. Birks, "Scintillations from Organic Crystals: Specific Fluorescence and Relative Response to Different Radiation," *Proc. Phys. Soc. A*, vol. 64, pp. 874–877, 1951.

[107] A. Cervera-Villanueva *et al.*, "RecPack a reconstruction toolkit," *Nuc. Instr. Meth. in Phys. Res. A*, vol. 534, pp. 180–183, 2004.

[108] C. Giganti, "The TPC beam test: PID studies, T2K Internal document, T2K-TN-003."

[109] R. Fruhwirth, "Application of Kalman filtering to track and vertex fitting," *Nuc. Instr. Meth. in Phys. Res. A*, vol. 262, pp. 444–450, 1987.

[110] A. Cervera-Villanueva *et al.*, "Kalman filter tracking and vertexing in a silicon detector for neutrino physics," *Nuc. Instr. Meth. in Phys. Res. A*, vol. 486, pp. 639–662, 2002.

[111] A. Carver, "Particle identification in the ND280 Electromagnetic Calorimeter, T2K Internal Document, T2K-TN-001."

[112] A. Hoecker *et al.*, "TMVA - Toolkit for multivariate data analysis."

[113] G. Wikstrom, "Global Kalman vertexing in ND280, T2K Internal document, T2K-TN-046."

[114] D. Simon *et al.*, "Secondary beams for tests in the PS East experimental area," *CERN PS/PA Note 93-21*, 1993.

[115] M. Bass *et al.*, "Quality assessment of t he 2010a data set at ND280, T2K Internal document, T2K-TN-013."

[116] M. Bass *et al.*, "Data quality at near detectors for Run2, T2K Internal document, T2K-TN-050."

[117] A. Cervera *et al.*, "Inclusive ν_μ CC analysis using the entire ND280 detector, T2K Internal document, T2K-TN-044."

[118] K. S. Cranmer, "Kernel estimation in high-energy physics," *Comput. Phys. Commun.* , vol. 136, pp. 198–207, 2001.

[119] C. Giganti, A. Longhin and M. Zito, "Measurement of the ν_e beam component with 2010a data using the ND280 tracker, T2K Internal document, T2K-TN-014."